REPORT DOCUMENTATION PAGE

Form Approved
OMB No. 0704-0188

1. REPORT DATE *(DD-MM-YYYY)*	2. REPORT TYPE	3. DATES COVERED *(From - To)*
07-03-2001	Final	Jun 1997 – Aug 2000

4. TITLE AND SUBTITLE

Shallow Water Waveguide Influences on Time Reversing Array Retrofocusing

5a. CONTRACT NUMBER

5b. GRANT NUMBER
N00014-97-1-0628

5c. PROGRAM ELEMENT NUMBER

6. AUTHOR(S)

Dowling, David R.

5d. PROJECT NUMBER
97PR05675-00

5e. TASK NUMBER

5f. WORK UNIT NUMBER

7. PERFORMING ORGANIZATION NAME(S) AND ADDRESS(ES)

University of Michigan
Department of Mechanical Engineering
2250 G.G. Brown
Ann Arbor, MI 48109-2125

8. PERFORMING ORGANIZATION REPORT NUMBER

DRDA# 97-1395

9. SPONSORING/MONITORING AGENCY NAME(S) AND ADDRESS(ES)

Office of Naval Research
Ballston Centre Tower One
800 North Quincy Street
Arlington, VA 22217-5660

10. SPONSOR/MONITOR'S ACRONYM(S)

ONR

11. SPONSORING/MONITORING AGENCY REPORT NUMBER

12. DISTRIBUTION AVAILABILITY STATEMENT

APPROVED FOR PUBLIC RELEASE

13. SUPPLEMENTARY NOTES

NONE

14. ABSTRACT

See Cover Page of Attached Final Report

20010314 124

15. SUBJECT TERMS

Underwater acoustics
Time reversal

16. SECURITY CLASSIFICATION OF:			17. LIMITATION OF ABSTRACT	18. NUMBER OF PAGES	19a. NAME OF RESPONSIBLE PERSON
a. REPORT	b. ABSTRACT	c. THIS PAGE			David R. Dowling
U	U	U	UU		19b. TELEPONE NUMBER *(Include area code)* 734-936-0423

Standard Form 298 (Rev. 8-98)
Prescribed by ANSI-Std Z39-18

FORM A1-2
AUGMENTATION AWARDS FOR SCIENCE & ENGINEERING
RESEARCH TRAINING (ASSERT)
REPORTING FORM

The Department of Defense (DOD) requires certain information to evaluate the effectiveness of the AASERT program. By accepting this Grant Modification, which bestows the AASERT funds, the Grantee agrees to provide the information requested below to the Government's technical point of contact by each annual anniversary of the ASSERT award date.

1. Grantee identification data: *(R & T and Grant numbers found on Page 1 of Grant)*

    a. THE REGENTS OF THE UNIVERSITY OF MICHIGAN

        University Name

    b. N00014-97-1-0628   c. 97PR05675-00

        Grant Number   PR Number

    d. David R. Dowling   e. From: 01 JUN 97   To: 31 MAY 00

        P.I. Name   AASERT Reporting Period

NOTE: Grant to which AASERT award is attached is referred to hereafter as "Parent Agreement."

2. Total funding of the Parent Agreement and the number of full-time equivalent graduate students (FTEGS) supported by the Parent Agreement during the 12-month period **prior to** the AASERT award date.

    a. Funding: $ 46,990

    b. Number FTEGS: 1

3. Total funding of the Parent Agreement and the number of FTEGS supported by the Parent Agreement during the current 12-month reporting period.

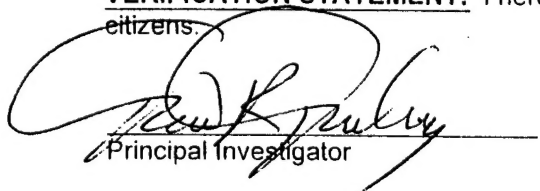   a. Funding: $ 65,000

    b. Number FTEGS: 1

4. Total AASERT funding and the number of FTEGS and undergraduate students (UGS) supported by AASERT funds during the current 12-month reporting period.

    a. Funding: $ 41,267

    b. Number FTEGS: 1

    c. Number UGS: 0

VERIFICATION STATEMENT: I hereby verify that all students supported by the AASERT award are U.S. citizens.

_____   3/8/01
Principal Investigator   Date

GRANT NUMBER: N00014-97-1-0628

A Final Report:

Shallow Water Waveguide Influences on Time Reversing Array Retrofocusing

David R. Dowling
Department of Mechanical Engineering
University of Michigan, Ann Arbor, MI 48109-2121
phone: (734) 936-0423   fax: (734) 764-4256   email: drd@engin.umich.edu
http://www.personal.engin.umich.edu/~drd/

Grant Number: N00014-97-1-0628

Thrust Category: Shallow-Water

ABSTRACT

This project seeks to quantitatively predict time-reversing array retrofocus size and longevity in the presence of the physical phenomena common in shallow ocean waters. These phenomena include guided-wave propagations, acoustic absorption, dynamic internal waves, and bottom roughness. In addition the influence of the orientation of linear arrays with respect to the waveguide axis and the source has been addressed.

RESULTS

The main findings of this project are contained in the three attached manuscripts. The research work completed here represents the doctoral dissertation of Michael R. Dungan.

ATTACHMENTS

[1] M.R. Dungan and D.R. Dowling, "Computed time-reversing array retrofocusing in a dynamic shallow ocean," J. Acoust. Soc. Am, Vol. 107, 3101-3112, 2000.

[2] M.R. Dungan and D.R. Dowling, "Computed narrowband azimuthal time-reversing array retrofocusing in shallow water," revised for the J. Acoust. Soc. Am, Nov. 2000.

[3] Dungan, M.R. and Dowling, D.R., "Orientation and linear time reversing array retrofocusing in shallow water," submitted to the Journal of the Acoustical Society of America, Feb. 2001

Computed narrow-band time-reversing array retrofocusing in a dynamic shallow ocean

Michael R. Dungan and David R. Dowling[a]

Department of Mechanical Engineering and Applied Mechanics, University of Michigan, Ann Arbor, Michigan 48109-2121

A time-reversing array (TRA) can retrofocus acoustic energy, in both time and space, to the original sound-source location without any environmental information. This unique capability may be degraded in time-dependent or noisy acoustic environments, or when propagation losses are prevalent. In this paper, monochromatic propagation simulations (based on the parabolic equation code, RAM) are used to predict TRA retrofocusing performance in shallow-water sound channels having characteristics similar to those measured during the recent SWARM (shallow-water acoustics in a random medium) experiment. Results for the influence of source–array range, source depth, acoustic frequency, bottom absorption, internal wave strength, and round-trip time delay are presented. For a fixed channel geometry, higher frequencies, deeper sources, and lower bottom absorption improve TRA performance and allow retrofocusing at longer ranges. In a dynamic shallow-water channel containing a random superposition of linear internal waves, the size of the retrofocus is slightly decreased and sidelobes are suppressed compared to the static channel results. These improvements last for approximately 1 to 2 min for source-array ranges near 10 km at a frequency of 500 Hz. For longer time delays, the internal waves cause significant TRA retrofocus amplitude decay, and the decay rate increases with increasing internal wave activity and acoustic frequency. © *2000 Acoustical Society of America.* [S0001-4966(00)06106-3]

PACS numbers: 43.30.Vh, 43.30.Yj, 43.30.Ft [DLB]

INTRODUCTION

Acoustic time reversal is the process of recording an acoustic signal and then replaying it backwards so that the last part of the recording is played first and the first part of the recording is played last. When this process is accomplished by an array of transducers (a time-reversing array, or TRA), the replayed sounds will focus at the place of their origin, provided that the acoustic environment is reciprocal and absorption losses are small. Because this retrofocusing occurs without environmental information, TRAs have some unique properties that are of interest in ultrasonics (Fink, 1997; Tanter, 1998) and underwater sound (Jackson and Dowling, 1991; Dowling and Jackson, 1992; Dowling, 1993, 1994; Parvulescu, 1995; Kuperman *et al.*, 1998; Song *et al.*, 1998; Khosla and Dowling, 1998). In fact, acoustic time reversal is now well on its way to becoming an established technique for focusing acoustic waves in unknown environments, and for acoustically characterizing unknown environments by quantitatively interrogating the retrofocus size and field amplitude. In particular, active TRA systems may facilitate moderate range (tens of kilometers) underwater communication through unknown acoustic environments. Novel uses of time-reversal concepts are also occurring in other areas of acoustics (Rose *et al.*, 1999; Roux *et al.*, 1999; Yönak and Dowling, 1999).

The dimensions, field amplitude, and temporal decay of the retrofocus produced by a narrow-band TRA are deter-mined by the signal frequency, the source–array geometry, and the acoustic environment. In general, higher frequencies lead to better TRA retrofocusing (Jackson and Dowling, 1991). Similarly, larger array apertures and shorter source-array ranges may also improve TRA retrofocusing (Dowling and Jackson, 1992; Hodgkiss *et al.*, 1997). The acoustic environment may aid or limit TRA retrofocusing. For example, inhomogeneous media may produce TRA superfocusing (Saichev, 1982; Dowling and Jackson, 1992; Derode *et al.*, 1995; Khosla and Dowling, 1998), while environmental dynamics typically cause retrofocus-amplitude decay (Dowling and Jackson, 1992; Dowling, 1994; Khosla and Dowling, 1998).

In a dynamic environment, the refractive-index structure associated with the source-to-array propagation step may change before the array-to-source propagation step because of the requisite time delay for propagation, recording, and signal processing. Therefore, when the time-reversed sound is reintroduced into the medium, it travels back through an altered version of the original environment, and retrofocusing is degraded because of this mismatch. Longer time delays produce larger mismatches that lead to greater TRA retrofocus degradation. The studies mentioned above show that this degradation may consist of lower focal amplitude, larger focal size, or stronger and more prevalent sidelobes (spurious retrofoci).

The environment may also limit TRA retrofocusing performance through absorption losses (Tanter *et al.*, 1998) and the restrictions associated with modal propagation (Kuperman, 1997). Hence, one of the most challenging applications of TRAs lies in shallow ocean sound channels where internal

---

[a]Author to whom correspondence should be addressed. Electronic mail: drd@engin.umich.edu

waves produce dynamic inhomogeneities, modal propagation is assured, and bottom absorption, bubbles, and rough-surface scattering provide important loss mechanisms. For the 100-Hz to 1-kHz simulation results presented here, only bottom absorption losses are included because they are likely to be the dominant loss mechanism at the source–array ranges of interest (1 to 50 km). The effects of bubbles are usually more prevalent at higher frequencies. Assessments of rough surface scattering and TRA performance are provided in Kuperman *et al.* (1998) and Khosla and Dowling (1998).

This paper presents the results of monochromatic numerical simulations of TRA retrofocusing performance in static and dynamic shallow ocean sound channels. The main independent parameter is the source–array range, R. The influence of variations in source depth, acoustic frequency, bottom absorption, internal wave strength, and round-trip time delay on TRA retrofocusing performance is presented. Properties of the sound channel are drawn from measurements made during the SWARM experiment (Apel *et al.*, 1997; Finette, 1998) and reference sources (Jensen *et al.*, 1994). For simplicity and clarity, only results from range-independent environments are presented, and only one array geometry has been considered: a linear vertical array having 24 elements that spans the nominal water column depth, and only sends and receives narrow-band signals. The effects of subsampling a water-column-spanning array are presented in Kuperman *et al.* (1998).

The remainder of this paper is organized into four sections. The next section describes the acoustic environment used in this study, the internal wave model, and the computational technique. Sections II and III present the simulation results for static and dynamic sound channels, respectively. The final section summarizes the findings and states the conclusions drawn from this study.

I. COMPUTATIONAL APPROACH

This study utilizes parabolic-equation (PE) computations to predict how TRA retrofocusing is influenced by the environmental parameters, source–array geometry, and acoustic frequency. The sound propagation computations were performed using the wide-angle PE-code RAM (Collins, 1993, 1994, 1998). The following three subsections describe the environments investigated, the internal wave model, and the implementation of RAM.

A. Environment

The basic or generic environment for this study is a range-independent sound channel (see Fig. 1) having a depth $D = 75$ m and a two-layer bottom. The r coordinate runs in the horizontal direction and the z coordinate has its origin at the water surface and increases downward. The sound-speed profile in the channel, shown in Fig. 2, was obtained by smoothing and combining oceanic measurements of water temperature and salinity as a function of depth. These measurements were provided by Finette (1998), and were made at the SWARM shallow site where the actual ocean depth is 75 m (Apel *et al.*, 1997). The unusual strength of the downward refraction in the profile of Fig. 2 is common in mid to late summer at the SWARM site. In addition, such a strongly
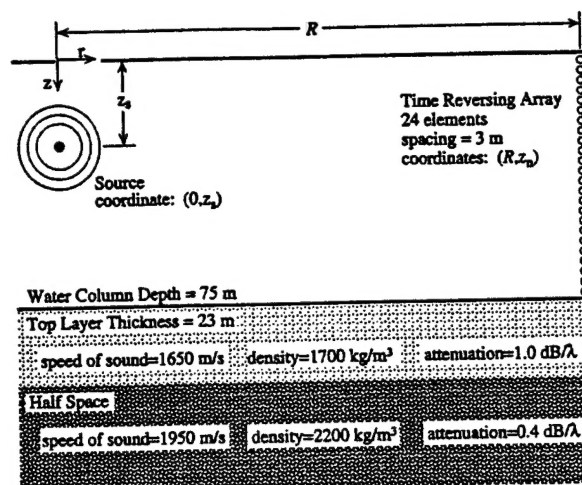

FIG. 1. Schematic of the sound channel and time-reversing array (TRA) geometry. The horizontal coordinate is r. The vertical coordinate, z, increases downward. The omnidirectional source at $(0, z_s)$ broadcasts at time t_1. The TRA receives the signal at (R, z_n) and retransmits to form the retrofocus at time t_2. In a dynamic acoustic environment, TRA retrofocus properties may be degraded when $t_2 - t_1 > 0$.

downward-refracting profile indicates favorable conditions for an active internal wave field. Such conditions were sought for the SWARM experiment (Apel *et al.*, 1997). For TRA operations, the main effect of the downward-refracting profile is to enhance the importance of array elements in the lower half of the water column while leaving the upper array elements somewhat underutilized.

The density, speed of sound, and thickness of the two bottom layers are based on core and chirp measurements made at the SWARM site (Apel *et al.*, 1997). The top layer has a thickness of 23 m, sound speed of 1650 m/s, and density of 1700 kg/m^3. The second layer is much thicker and has a sound speed of 1950 m/s and a density of 2200 kg/m^3. Attenuation values of 1.0 decibel per wavelength in the upper layer, and 0.40 decibel per wavelength in the lower layer were extrapolated from tabulations in Jensen *et al.* (1994) as conservative matches to the available geological measurements. The top of the sound channel was treated as a flat pressure release surface.
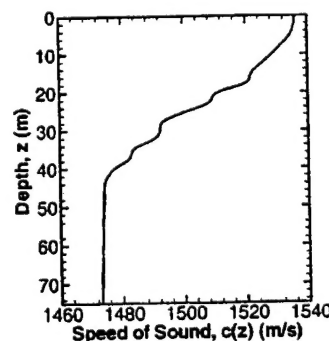

FIG. 2. Speed of sound versus depth for the standard sound channel. This profile is based on measurements made during the 1995 SWARM experiment and was provided to the authors by Dr. Steven Finette of the Naval Research Laboratory.
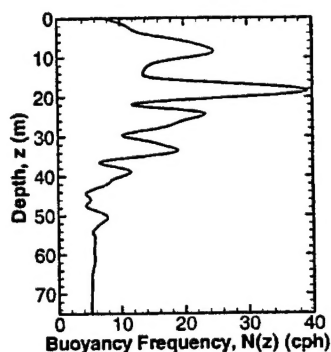
FIG. 3. Buoyancy frequency versus depth for the standard sound channel. This profile is based on measurements made during the 1995 SWARM experiment and was provided to the authors by Dr. Steven Finette of the Naval Research Laboratory.

The environmental parameters given above will be the same throughout the rest of this paper unless stated otherwise. For example, results from differing levels of absorption in this environment are presented in Sec. II.

B. Linear internal waves

The dynamic effects of internal waves on TRA retrofocusing were predicted by inserting a random superposition of linear internal waves into the sound channel described above (similar to the formulation in Dashen et al., 1979 and Tielbürger et al., 1997). The interaction of tides and the local continental shelf can lead to nonlinear soliton-type internal waves, while random shallow-water linear internal waves are merely the near-coast extension of deep-water linear internal waves (Garrett and Munk, 1979, provides a review of deepwater internal wave properties). Here, the internal wave model is intended to represent the shallow SWARM site in the absence of soliton activity. Figure 3 shows the Brunt–Väisälä or buoyancy frequency profile, $N(z)$, used to determine and animate the internal waves. This profile was obtained by smoothing water-column density measurements from the SWARM shallow site (Finette, 1998).

Internal waves cause heaving motions within the water column that alter the local sound speed by lifting and lowering the otherwise static contours of constant sound speed. The vertical deflections produced by these internal waves are governed by a second-order differential equation (Dashen et al., 1979)

$$\frac{d^2}{dz^2}W(z)+k_h^2\left[\frac{N^2(z)-\omega^2}{\omega^2-f_c^2}\right]W(z)=0, \qquad (1)$$

which, along with the waveform boundary conditions of $W(0)=W(D)=0$, creates an eigenvalue problem. Here, $W(z)$ is the vertical displacement produced by an internal wave having radian frequency ω, k_h is the horizontal wave number of the internal wave, and $f_c=2\Omega\sin$ (°latitude) is the inertial frequency with Ω equal to the rotation rate of the earth. In this study, f_c was evaluated at a latitude of 39.25°, corresponding to the center of the SWARM site. When ω and k_h are independent parameters, (1) has eigenmode solutions $W(k_h,j,z)$ at a discrete set of frequency eigenvalues

$\omega_j(k_h)$. The internal wave modes and frequencies particular to this study were calculated from (1) using standard shooting techniques (see Press et al., 1986). Hence, a dynamic three-dimensional simulation of the internal-wave-induced vertical displacement η can be obtained by a triple sum over internal-wave modes (j), horizontal wave numbers (k_h), and azimuthal angles (θ),

$$\eta(r,\phi,z,t)=\mathrm{Re}\left\{\sum_j\sum_{k_h}\sum_\theta F(k_h,j)W(k_h,j,z)\right.$$
$$\times\exp[ik_hr\cos\theta\cos\phi+ik_hr\sin\theta\sin\phi$$
$$\left.-i\omega(k_h,j)t]\right\}, \qquad (2a)$$

where ϕ is the azimuthal angle associated with the $r-z$ coordinate system. The F term is a Gaussian random complex weighting having a uniform distribution in θ and a Garrett–Munk spectrum in mode number and horizontal wave number

$$\langle\|F(k_h,j)\|^2\rangle=\frac{4}{\pi}E_0M[j^2+j_*^2]^{-p/2}k_jk_h^2(k_h^2+k_j^2)^{-2}, \qquad (2b)$$

where

$$k_j=\frac{\pi jf_c}{\int_0^D N(z)dz}, \qquad (2c)$$

$$M=\left\{\sum_{j=1}^\infty (j^2+j_*^2)^{-p/2}\right\}^{-1}, \qquad (2d)$$

E_0 is the internal-wave energy level, j_* is the mode weighting parameter, and p is the mode weighting exponent. The sum given in (2a) was calculated using a variable azimuthal resolution so that random numbers were assigned to approximately equal tile areas of the $k_h-\theta$ plane for each value of j. Hence, the number of θ evaluations in (2a) increased linearly with increasing k_h. The parametric ranges and increments used were: $1\le j\le 15$, $5\times10^{-4}\,\mathrm{m}^{-1}\le k_h\le 1.5\times10^{-1}\,\mathrm{m}^{-1}$, with steps of $\Delta k_h=5\times10^{-4}\,\mathrm{m}^{-1}$, and $0\le\theta\le360°$ with $\Delta\theta=2°$ when $k_h=1.5\times10^{-1}\,\mathrm{m}^{-1}$. The internal wave mode shapes $W(k_h,j,z)$ evolve gradually with increasing k_h, so mode shapes were interpolated between the minimum and maximum values of k_h with intervening calculations every $10^{-2}\,\mathrm{m}^{-1}$. It was found that additional refinements influenced the statistics of the simulated internal wave fields less than a change in the random number seed. In addition, the plane $\phi=0$ was chosen throughout this study, so the second term in the exponential function in (2a) was consistently zero.

The Garrett–Munk spectrum parameters (E_0,p,j_*) were chosen to match a temporal power spectrum of vertical displacements measured at the SWARM shallow site (75-m depth) without soliton activity (Finette, 1998). This was accomplished by using (2a) at a fixed depth of 25 m to generate a synthetic vertical displacement time series, computing the power spectrum from this synthetic time series, and then comparing the resulting synthetic spectrum with the SWARM measurements. Adjustments were made to the
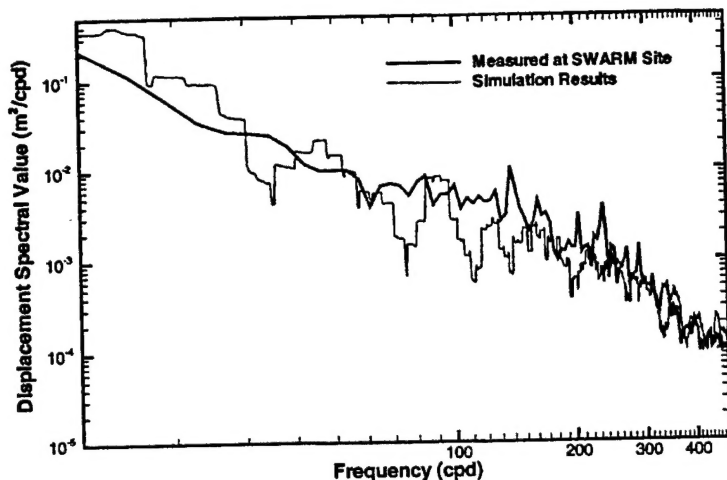
FIG. 4. Comparison of the synthetic internal-wave vertical-displacement temporal power spectrum and a spectrum measured during the 1995 SWARM experiment in the absence of soliton internal waves. The measured spectrum was provided to the authors by Dr. Steven Finette of the Naval Research Laboratory.

spectrum parameters until a visually acceptable match of the two spectra was achieved. Figure 4 shows a sample result for the final parameter choices: $j_* = 1$, $p = 4$, and $E_o = 24.6 \, \text{J/m}^2$. Other independent research suggests similar values for these parameters (Tielbürger, 1997; Yoo and Yang, 1998; Yang and Yoo, 1998). Spectral matches obtained with shallower (15 m) and deeper (40 m) synthetic data were not quite as good as that shown in Fig. 4, but deviations from the measured spectrum at these locations were comparable to those produced by changes in the random number seed.

Sample internal-wave vertical-displacement fields, $\eta(r,0,z,t)$, are shown in Fig. 5 for $t = 0$ (a), and $t = 20 \, \text{min}$ (b) over a 50-km range. Comparison of Fig. 5(a) and (b) shows that the short wavelength features of the internal wave field decorrelate in 20 min, while the long wavelength features persist, as expected. The disruption by internal waves of the initial layered sound-speed profile (Fig. 2) is accomplished by merely deflecting the static sound-speed profile by

$\eta(r,0,z,t)$ at each depth and range location in the input file to RAM. Corrections to the internal-wave-induced sound-speed changes due to the adiabatic gradients in the water column variables were on the order of 1% and were therefore neglected.

C. RAM implementation

The main value of a computational study like this one is the ease with which parametric studies may be completed. Here, the main computational tool is the one-way wide-angle PE code RAM (Collins, 1993, 1994, 1998) modified to output the real and imaginary field components at each grid point. RAM is based on a split-step Padé solution method. In the forward propagation step (at time t_1), a point source with radian frequency ω located at $(0,z_s)$ ensonifies the sound channel described above. Elements of the TRA located at (R,z_n), record this field, complex conjugate it [complex conjugation is the equivalent of time reversal for narrow-band
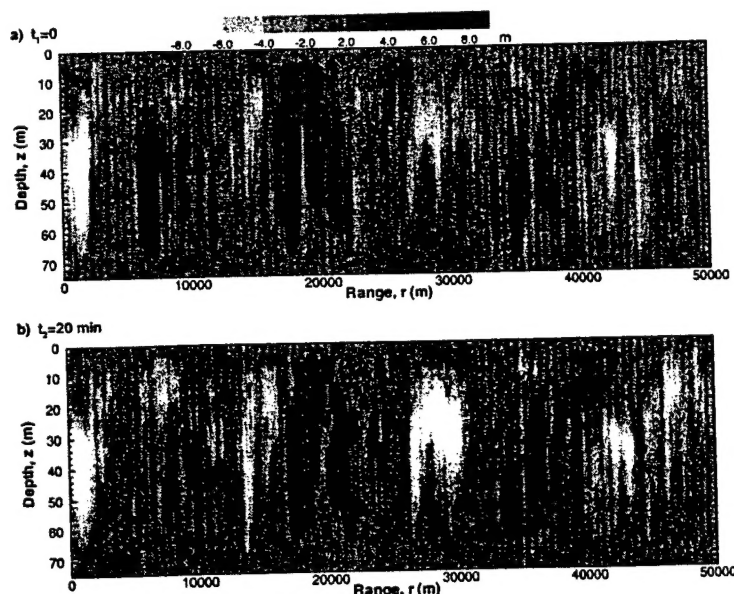

FIG. 5. Sample synthetic internal-wave vertical displacement fields over a 50-km range at an initial time (a), and 20 min later (b). In 20 min most of the small-scale fluctuations have changed, but the larger scale deflections persist. The gray scale ranges from white (less than −8-m downward deflection) to black (more than +8-m upward deflection).

signals (Jackson and Dowling, 1991)], amplify it, and re-broadcast it (at time t_2). Thus, the response of the array is entirely described by the complex-conjugate Green's function, $G_{c\omega}$ [see Dowling and Jackson (1992), Eq. (10), or Kuperman et al. (1998), Eq. (7)]

$$G_{c\omega}(r,z,t_2-t_1) = \sum_{n=1}^{N} G_{2\omega}(r,z;R,z_n)G_{1\omega}^{*}(R,z_n;0,z_s) \quad (3)$$

where r and z are the range and the depth coordinates, respectively, N is the number of array elements, $G_{m\omega}(r,z;r',z')$ is the Green's function at radian frequency ω for acoustic propagation from (r',z') to (r, z) at time t_m, and the asterisk denotes complex conjugation. The time delay, t_2-t_1, becomes important in dynamic environments. For all retrofocusing computations presented here, the array had 24 elements with 3-m vertical spacing. Here, the use of RAM to compute the fields $G_{1\omega}$ and $G_{2\omega}$ limits the acoustic propagation to the $r-z$ plane. Out-of-plane scattering from the fully three-dimensional synthetic internal wave fields is neglected. Neglect of azimuthal scattering is acceptable as long as the average water column properties are range independent, and the internal-wave-induced horizontal gradients in the speed of sound are much smaller than the vertical sound-speed gradients. Both conditions are satisfied here.

To characterize the strength of the retrofocused field at different ranges and depths, the TRA transmission loss is defined

$$TL_{c\omega} = -20\log\left(\frac{G_{c\omega}(r,z,t_2-t_1)}{G_{c\omega}(1\text{ m},z_s,0)}\right). \quad (4)$$

Here, the reference amplitude is that obtained at the retrofocus of the same array operated in free space when the source–array range is 1 m.

Studies of one-way propagation and computational reciprocity, as well as comparisons to modal sum calculations, were conducted to determine the input parameters best suited for the retrofocus problem at hand. Such parameters include the number of Padé terms, depth and range grid spacing, and computational bottom depth and attenuation. Convergence studies confirmed the choices of eight Padé terms, a depth grid spacing of 1/60th of a wavelength or less, and a range grid spacing of no more than four-thirds of a wavelength. A short-range step is required to obtain the details in the retrofocus peak region. The computational bottom depth was taken to be at least three times the water column depth. Within a few wavelengths of the computational bottom, the attenuation ramps up to a final value of 10.0 dB per wavelength to prevent artificial reflections.

Figure 6 shows a sample TRA retrofocus calculation in the standard sound channel without internal waves for a source depth of $z_s = 25$ m at a frequency of 500 Hz and a source–array range of $R = 10$ km. The horizontal (range) axis is zoomed in to the region near the source. The array lies off the figure to the right. As expected, the retrofocus peak appears in the correct location and is clearly the highest amplitude feature on the vertical path through $r = 0$. In fact, close inspection of Fig. 6 shows that all sound amplitudes above and below the retrofocus are well below the up- and down-
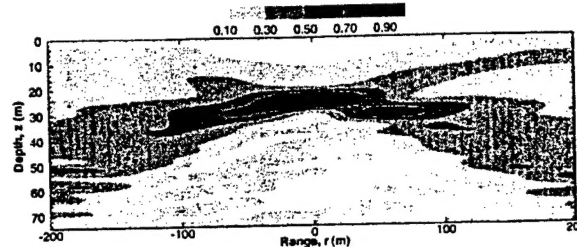

FIG. 6. Sample retrofocus field without internal waves for a source depth of $z_s = 25$ m, an acoustic frequency of $f = 500$ Hz, and a source–array range of $R = 10$ km. The peak amplitude occurs at the correct location and the nearest sidelobe is roughly 60 m up-range from the original source location.

range sidelobes. This is a clear indication that nearly all of the propagating sound energy passes near the source location, and that the retrofocus is not spurious.

II. STATIC SOUND CHANNEL RESULTS

The results of this investigation into the retrofocusing capability of a time-reversing array are presented in two parts. This section contains results for static sound channels lacking internal wave motions. The parameters explored here include source depth, source–array range, acoustic frequency, and bottom attenuation. The next section covers a dynamic sound channel containing internal waves.

Figure 7(a) shows how the retrofocus field at $r = 0$ depends on the source depth z_s in the standard sound channel at a frequency of 500 Hz and $R = 10$ km. The darkness of the gray scale is proportional to $G_{c\omega}(0,z,0)/G_{c\omega}(0,z_s = 63\text{ m},0)$ where the loudest retrofocus was obtained at a source depth $z_s = 63$ m. This figure shows that retrofocusing is loudest in the lower third of the sound channel, as would be expected with the pressure release boundary condition at $z = 0$ and the strongly downward-refracting sound-speed profile (Fig. 2). Figure 7(b) shows the same retrofocus information normalized by the peak amplitude on each vertical slice. In an ideal environment, the central dark diagonal curve in Fig. 7(b) would be straight and most of the figure would be white. Here, the vertical sidelobe structure is weakest above the source and when the source resides in the lower half of the sound channel below the thermocline.

Figure 8 shows how the retrofocus field at $r = 0$ changes with increasing source–array range R at four acoustic frequencies, $f = 100$ Hz, 250 Hz, 500 Hz, and 1 kHz, for a source depth of $z_s = 25$ m. For both this and the next figure, the gray-scale darkness is proportional to $G_{c\omega}(0,z,0)$ divided by its maximum value. This scaling eliminates the effect of focal amplitude decay caused by increasing R.

Several interesting trends are shown in Fig. 8. First, higher frequencies produce smaller retrofoci whose size is essentially proportional to the acoustic wavelength. Here, the vertical retrofocus size is approximately three wavelengths (or less) out to ranges of 10 km at all four frequencies. A second trend shown in Fig. 8 is that higher frequencies lead to effective retrofocusing at longer ranges. Better retrofocusing at longer ranges requires more weakly absorbed modes, and higher acoustic frequencies allow a greater number of (all types of) modes for fixed sound channel properties. A
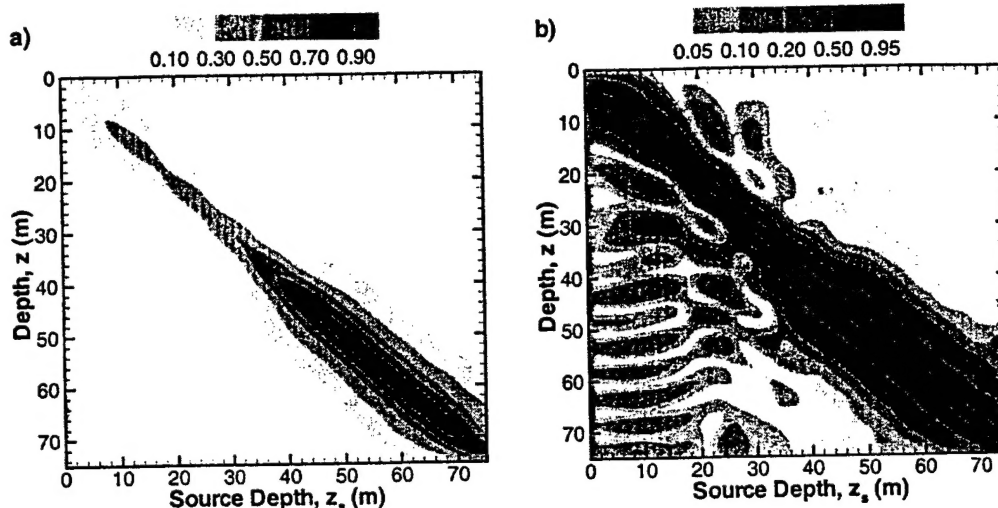
FIG. 7. Retrofocus field amplitude through the channel depth on a vertical line at $r=0$ versus source depth without internal waves at an acoustic frequency of $f=500$ Hz and a source–array range of $R=10$ km. In (a), the gray scale is normalized to the overall peak amplitude, which is found at a source depth of $z_s=63$ m. Because of the modal structure of the sound channel, source locations in the lower third of the channel lead to stronger (louder) retrofoci. In (b), the gray scale is normalized by the peak amplitude on each vertical slice so that the sidelobe structure of each retrofocus is more clearly displayed. Minimal sidelobes occur when the retrofocus is in the lower half of the sound channel.

third trend seen in Fig. 8 is the downward drift and vertical growth of the focal spot at all frequencies with increasing range. This third trend has also been found in TRA experiments performed in the Mediterranean Sea (Hodgkiss *et al.*, 1997). The retrofocus drift is most apparent at $f=100$ Hz [Fig. 8(a)], where there is essentially only one propagating mode for $R>20$ km.

In Fig. 9, results similar to those shown in Fig. 8 are displayed for a deeper source placed at $z_s=50$ m. Here, the

same three trends are found except that vertical drift of the retrofocus location is less pronounced because this lower source lies near the antinode of the most persistent propagating mode.

To complement the results in Figs. 8 and 9, Table I provides the computed-field transmission loss, $\text{TL}_{c\omega}$, for the retrofocus-field peak amplitude through the depth at source–array ranges of $1\text{ km} \leq R \leq 50\text{ km}$ for four acoustic frequencies, $f=100$ Hz, 250 Hz, 500 Hz, and 1 kHz, and source
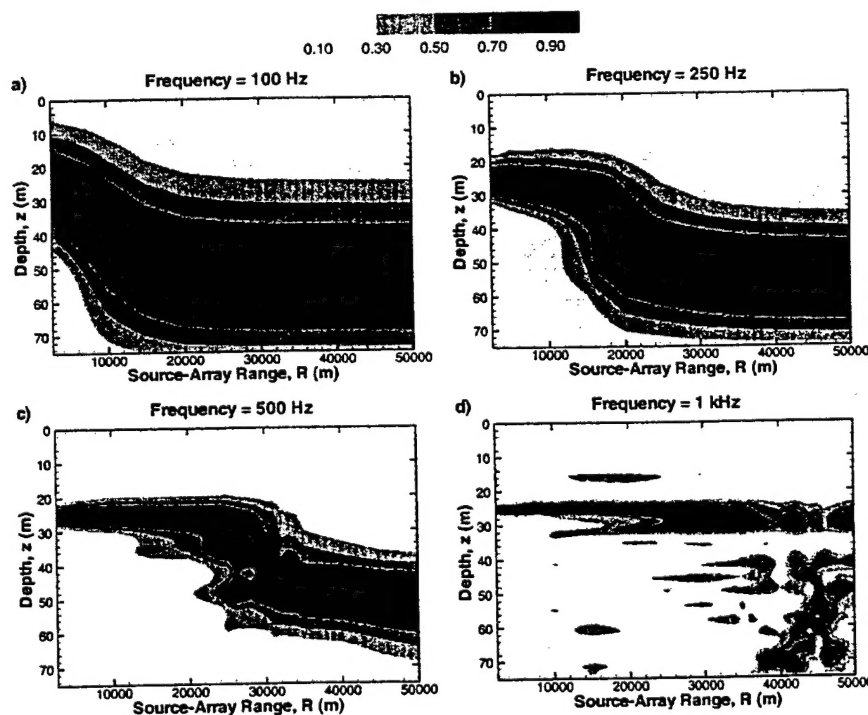

FIG. 8. Retrofocus field amplitude through the channel depth on a vertical line at $r=0$ versus source–array range R without internal waves at a source depth of $z_s=25$ m at acoustic frequencies of $f=100$ Hz (a), 250 Hz (b), 500 Hz (c), and 1 kHz (d). Here, each vertical slice is normalized by its maximum value so that the vertical growth and migration of the retrofocus with increasing R is emphasized. Dark regions lie near the local field maximum at any R. As expected, higher frequencies produce tighter retrofoci.
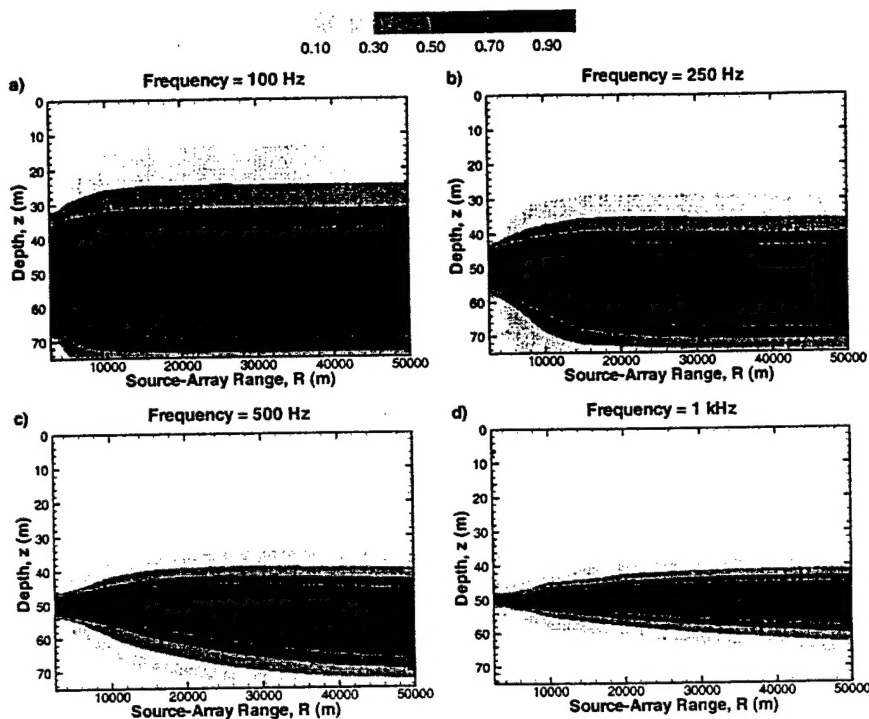
FIG. 9. Retrofocus field amplitude through the channel depth on a vertical line at $r=0$ versus source–array range R without internal waves for a source depth of $z_s=50$ m at acoustic frequencies of $f=100$ Hz (a), 250 Hz (b), 500 Hz (c), and 1 kHz (d). Here, each vertical slice is normalized by its maximum value so that the vertical growth and migration of the retrofocus with increasing R is emphasized. Dark regions lie near the local field maximum at any R. As expected, higher frequencies produce tighter retrofoci.

depths of $z_s=25$ m (Table Ia) and $z_s=50$ m (Table Ib). These results show that $TL_{c\omega}$ is not always monotonically increasing with increasing R. Table I also lists the depth of the retrofocus peak, z_{rp} (which indicates the vertical retrofocus drift), and the amplitude of the largest vertical sidelobe in dB relative to the retrofocus peak amplitude. For the shallower source, sidelobe amplitudes generally increase with increasing source–array range until absorption losses in the modal propagation cause the retrofocus location to shift. At this juncture, sidelobe amplitudes sometimes exceed that of the intended retrofocus (for example: $f=1$ kHz, $z_s=25$ m, and $R=40$ km). As R is increased further, the retrofocus eventually settles onto the lowest propagating mode and sidelobes no longer exist [see Fig. 8(a)–(c)]. Sidelobes are

TABLE I. TRA retrofocus parameters for various source–array ranges (R) and frequencies (f) for two source depths: $z_s=25$ m (a) and $z_s=50$ m (b). The TRA transmission loss, $TL_{c\omega}$, is computed from (4) for the peak value of the retrofocus field through the depth. The vertical location of this retrofocus peak is z_{rp}. The sidelobe ratio is based on the strongest sidelobe, and a negative sidelobe ratio implies that the sidelobe amplitude is less than the retrofocus peak. If sidelobes are absent or the sidelobe ratio is less than -70 dB, table entries are left blank.

| | Frequency | | | | | | | | | | | |
| | 100 Hz | | | 250 Hz | | | 500 Hz | | | 1000 Hz | | |
Range (km)	$TL_{c\omega}(z_{rp})$ (dB)	z_{rp} (m)	Sidelobe ratio (dB)	$TL_{c\omega}(z_{rp})$ (dB)	z_{rp} (m)	Sidelobe ratio (dB)	$TL_{c\omega}(z_{rp})$ (dB)	z_{rp} (m)	Sidelobe ratio (dB)	$TL_{c\omega}(z_{rp})$ (dB)	z_{rp} (m)	Sidelobe ratio (dB)
					(a) Source depth=25 m							
1.0	37.3	23.5	−20.1	37.0	25.5	−15.5	37.0	25.0	−15.0	37.6	25.0	−7.1
2.0	41.7	25.5	−19.2	41.6	25.5	−17.1	41.8	25.0	−16.1	41.9	25.0	−9.1
5.0	49.4	29.0	−17.1	50.0	26.0	−24.7	50.1	25.0	−16.5	50.7	25.0	−11.3
10.0	56.1	39.5		58.7	27.5	−15.1	60.0	25.0	−12.5	60.2	25.0	−9.1
20.0	61.9	51.0		68.0	46.5		74.1	26.0	−11.6	73.7	25.5	−4.2
30.0	67.9	53.0		66.1	52.0		82.3	36.5	+0.7	86.3	26.5	−0.6
40.0	74.1	53.0		66.5	54.5		77.2	48.0	−38.2	94.4	29.0	+3.7
50.0	80.2	53.5		68.7	55.5		73.1	51.0	−57.0	103.6	29.5	−2.0
					(b) Source depth=50 m							
1.0	35.9	50.0	−18.5	36.1	50.0	−19.9	36.1	50.0	−17.4	35.3	50.0	−13.3
2.0	40.3	51.0	−22.5	40.2	50.0	−21.9	40.2	50.0	−20.1	40.4	50.0	−12.6
5.0	46.8	50.5	−32.3	46.6	50.0	−29.4	46.6	50.0	−15.8	46.7	50.5	−17.0
10.0	52.7	52.5		52.0	51.0	−37.5	52.0	50.0	−37.8	52.5	50.0	−22.7
20.0	60.8	53.5		57.8	53.5		57.6	51.0	−54.3	57.8	50.0	−36.6
30.0	67.7	53.5		61.7	55.5		61.0	52.5		61.2	50.5	−35.2
40.0	74.1	53.5		65.1	56.0		63.4	54.5		63.6	51.0	−40.9
50.0	80.2	53.5		68.2	56.0		65.4	56.0		65.7	51.5	

TABLE II. TRA retrofocus parameters for various source–array ranges (R) and bottom absorption levels for two source depths: $z_s = 25$ m (a) and $z_s = 50$ m (b) at a frequency of 500 Hz. Other parameters are the same as for Table I.

Range (km)	Quarter attenuation			Half attenuation			Nominal attenuation			Double attenuation		
	$TL_{c\omega}(z_{rp})$ (dB)	z_{rp} (m)	Sidelobe ratio (dB)	$TL_{c\omega}(z_{rp})$ (dB)	z_{rp} (m)	Sidelobe ratio (dB)	$TL_{c\omega}(z_{rp})$ (dB)	z_{rp} (m)	Sidelobe ratio (dB)	$TL_{c\omega}(z_{rp})$ (dB)	z_{rp} (m)	Sidelobe ratio (dB)
(a) Source depth=25 m												
1.0	35.6	25.0	−12.7	36.1	25.0	−13.7	37.0	25.0	−15.0	38.5	25.0	−15.4
2.0	39.4	25.0	−13.9	40.3	25.0	−14.8	41.8	25.0	−16.1	44.5	25.0	−17.1
5.0	44.6	25.0	−18.9	46.7	25.0	−19.6	50.1	25.0	−16.5	56.0	25.5	−13.3
10.0	50.1	25.0	−13.8	53.7	25.0	−15.5	60.0	25.0	−12.5	70.8	26.0	−5.4
20.0	56.3	25.0	−16.0	62.7	25.5	−14.0	74.1	26.0	−11.6	75.5	48.5	−34.3
30.0	61.3	25.5	−14.4	70.3	25.5	−7.9	82.3	36.5	+0.7	68.2	52.5	
40.0	66.1	25.5	−13.8	77.6	26.5	−8.8	77.2	48.0	−38.2	68.5	56.0	
50.0	69.6	25.5	−10.5	83.1	27.5	0.0	73.1	51.0	−57.0	70.5	57.5	
(b) Source depth=50 m												
1.0	35.2	50.0	−13.3	35.5	50.0	−14.6	36.1	50.0	−17.4	37.1	50.0	−22.4
2.0	38.5	50.0	−14.1	39.1	50.0	−17.1	40.2	50.0	−20.1	41.7	50.0	−18.2
5.0	43.5	50.0	−17.4	44.8	50.0	−18.3	46.6	50.0	−15.8	48.8	51.0	−25.2
10.0	47.8	50.0	−21.9	49.6	50.0	−17.9	52.0	50.0	−37.8	54.6	51.0	−51.9
20.0	52.6	50.0	−17.5	55.0	50.0	−35.8	57.6	51.0	−54.3	60.2	54.0	
30.0	55.7	50.0	−34.3	58.3	50.5	−61.2	61.0	52.5		63.8	56.5	
40.0	58.1	50.0	−38.6	60.7	51.0	−57.9	63.4	54.5		66.9	58.0	
50.0	59.9	50.0	−44.4	62.6	51.5	−59.9	65.4	56.0		69.7	58.5	

uniformly small for the deeper source. In addition, examination of Figs. 8 and 9 and Table I shows that when the retrofocus occurs within a wavelength or two of the intended depth (z_s) the shallower source generally produces a quieter but smaller retrofocus.

Taken together, these results clearly show that the shape and number of propagating modes in the sound channel are critical to forming a robust retrofocus. The shallower retrofocus requires acoustic penetration of the strongly downward-refracting portion of the sound-speed profile, and this is only possible with the highest-order propagating modes. A higher acoustic frequency (or deeper sound channel) allows more of the highest-order modes to propagate further. Retrofocusing at the deeper source does not require acoustic modes that penetrate into the strongly downward-refracting portion of the sound-speed profile, and thus is less sensitive to the presence or lack of the highest-order modes. This point is supported by the retrofocus size results in Figs. 8 and 9, which show that deeper retrofoci tend to have larger vertical extent.

To confirm these interpretations of the relative amplitudes and sizes of the TRA retrofocus, a parameter study on the bottom attenuation level was undertaken at an acoustic frequency of $f = 500$ Hz with different attenuation values in the two bottom layers. In practice, of course, once an ocean site has been selected there is no control over these variables, but understanding the trends may lead to more effective use of TRA systems. The results of this attenuation study are presented in Table II for one quarter (0.25 and 0.10 dB/λ), one half (0.50 and 0.20 dB/λ), one (1.00 and 0.40 dB/λ), and two (2.00 and 0.80 dB/λ) times the nominal attenuation values for source depths of $z_s = 25$ m (Table IIa) and $z_s = 50$ m (Table IIb). When the retrofocus occurs near its intended location, greater bottom loss always leads to lower retrofocus amplitudes. However, comparisons within Table II show that

the deeper source is much less influenced by the level of bottom losses, which confirms the description of sound-channel retrofocusing given above.

From these studies of retrofocusing in static sound channels, a common theme emerges: deeper sources lying below the strongly downward-refracting portion of the sound-speed profile generally lead to a louder, larger TRA retrofocus independent of the acoustic frequency, source–array range, and attenuation level. Results given in the next section also show that the TRA retrofoci produced by shallow and deep sources have differing properties in dynamic shallow-water environments.

III. DYNAMIC SOUND CHANNEL RESULTS

This section presents TRA retrofocusing results for a dynamic sound channel that contains a linear superposition of synthetic internal waves whose temporal spectrum was matched to measurements taken during the SWARM experiment. Throughout this section, the static characteristics of the sound channel are the same as those described in Sec. I and shown in Fig. 1. The main effect of dynamic evolution of the sound channel is to degrade the retrofocus amplitude during the time delay ($t_2 - t_1$) between the source broadcast (time=t_1) and the formation of the retrofocus (time=t_2). The independent parameters explored in this section are source depth, source–array range, acoustic frequency, internal wave strength, and time delay.

Figure 10 shows a sample of how the TRA retrofocus field degrades for $z_s = 25$ m, $f = 500$ Hz, and $R = 10$ km. The first frame [Fig. 10(a)] corresponds to the ideal case of retrofocusing in a *frozen* ocean containing SWARM-strength internal waves (i.e., $t_2 - t_1 = 0$). The second, third, and fourth frames [Fig. 10(b)–(d)] show the retrofocus field at time delays of $t_2 - t_1 = 1$, 2, and 5 min, respectively. The gray scale
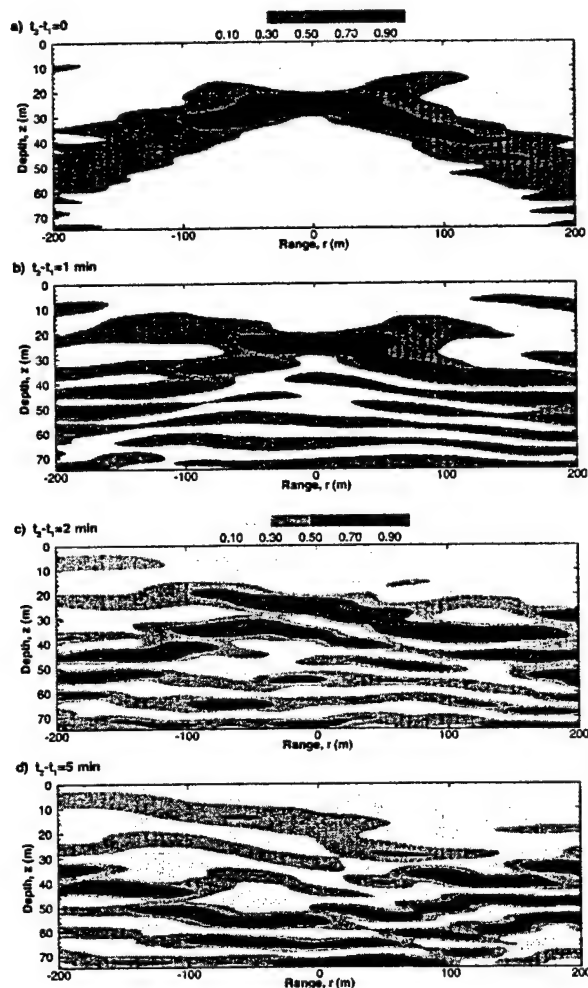
FIG. 10. Sample retrofocus fields with SWARM-strength synthetic internal waves for a source depth of $z_s = 25$ m, an acoustic frequency of $f = 500$ Hz, and a source–array range of $R = 10$ km. The time delay is $t_2 - t_1 = 0$, 1, 2, and 5 min in frames (a), (b), (c), and (d), respectively. This series of frames shows how the retrofocus is degraded in a dynamic sound channel. Comparison of frame (a) with Fig. 6 shows that the internal waves lead to a slight decrease in the retrofocus size and a reduction of the nearby sidelobes.

is the same in all three frames. Comparison of these three frames shows that the retrofocus is degraded by amplitude loss, sidelobe growth, and position migration, but not by an obvious change in retrofocus size. In fact, a comparison of Fig. 10(a) and Fig. 6 shows that the internal waves lead to only a slight reduction in the size of the retrofocus and a somewhat stronger suppression of the nearest sidelobes. Hence, the retrofocus amplitude is chosen to be the main performance metric as $t_2 - t_1$ increases. It would certainly be critical to any underwater communication scheme based on amplitude modulation.

Figure 11 provides a sample of how the amplitude at the intended retrofocus location changes with increasing $t_2 - t_1$ when $R = 10$ km at four internal-wave energy levels for $f = 100$ Hz [Fig. 11(a)], 250 Hz [Fig. 11(b)], 500 Hz [Fig. 11(c)], and 1 kHz [Fig. 11(d)], and a source depth of z_s

$= 25$ m. Here, the four internal-wave energy levels have been obtained by multiplying the value of E_0 obtained by matching the synthetic internal-wave spectrum to the measured SWARM spectrum by: 4, 1, 0.1, and 0.01, adjusting η, and then recomputing the forward and backward propagating sound fields at the same time delays. All the results in Fig. 11 are for one internal wave realization. The black dots in Fig. 11(c) denote the locations of the retrofocus fields shown in Fig. 10(b)–(d). As expected, the more active internal-wave fields and the higher frequencies lead to the quickest loss of amplitude. However, the field decay is not always monotonic and there are cases where the internal waves slightly enhance the retrofocus or cause it to reemerge after a hiatus of many minutes [see Fig. 11(b)]. Similar time-dependent features of shallow-water TRA retrofocusing have been observed during the experiments in the Mediterranean Sea (Song, 1998).

Results similar to those shown in Fig. 11 are obtained at $z_s = 50$ m, except that the retrofocus amplitude decay rates are different. When results like these are averaged over multiple realizations for fixed internal-wave energy level at a variety of source–array ranges, a performance envelope for a water-column-spanning TRA can be plotted. Figure 12 presents such performance envelopes for SWARM-level internal waves, 0.5 km $\leqslant R \leqslant 50$ km, $0.2 \leqslant t_2 - t_1 \leqslant 300$, $f = 100$ Hz, 250 Hz, 500 Hz, and 1 kHz, and source depths of $z_s = 25$ m [Fig. 12(a)] and $z_s = 50$ m [Fig. 12(b)]. Here, the plotted curves are the loci of the points where the amplitude at the intended retrofocus location has fallen by a factor of 2 (6 dB) from its value when $t_2 - t_1 = 0$. These results are based on 20 internal-wave realizations with the extreme highest and lowest retrofocus ranges ignored. Acceptable focusing should occur below and to the left of these lines, while retrofocusing is marginal or not assured above and to the right of them. The horizontal error bars denote the 50%-confidence interval for each curve. As the widths of these intervals suggest, considerable variability was found, especially for the deeper source [Fig. 12(b)]. These half-life curves are truncated when the retrofocus is lost because of absorption. The black dots in Fig. 12(a) denote the locations of the retrofocus fields shown in Fig. 10(b)–(d). The upward-sloping diagonal line in both frames is the causality boundary. Realizable TRA systems must operate above and to the left of this line.

Comparison of the two frames of Fig. 12 shows that, for sufficiently long time delays (greater than 10–20 min at 1 kHz, for example), the shallower source leads to a more robust retrofocus. However, the deeper source generally allows longer-range retrofocusing for time delays less than 10 min. The explanation of this changeover may lie in the fact that all important propagating modes must arrive in phase at the source location for proper retrofocusing. Shallow-source retrofocusing relies primarily on the higher-order modes, while deeper-source retrofocusing utilizes all propagating modes (this is why deeper retrofoci are also louder). Hence, internal-wave-produced scattering and phase perturbations of the low-order modes do not influence the shallow retrofocus as much as the deeper one because the shallow retrofocus is not produced by as many modes. Thus, the deeper retrofocus
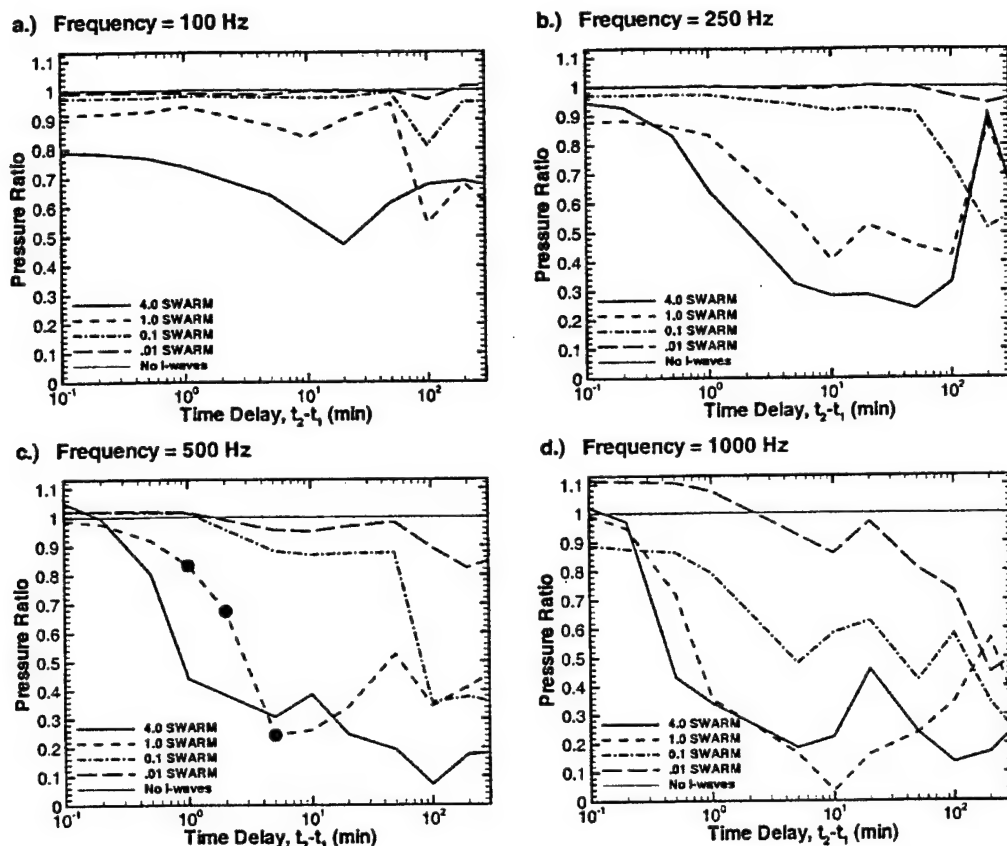
FIG. 11. Sample retrofocus field amplitude versus time delay for four internal-wave energy levels when $R = 10$ km. The vertical axis is the retrofocus field amplitude at $z = z_s = 25$ m divided by that found without internal waves. The various curves are for 4.0 (———), 1.0 (‐‐‐), 0.1 (·····), and 0.01 (– – –) times the measured SWARM internal-wave energy level. The four frames are for acoustic frequencies of 100 Hz (a), 250 Hz (b), 500 Hz (c), and 1 kHz (d). The retrofocus persists for longer periods of time at lower frequencies and lower internal-wave activity levels. The black dots in (c) correspond to the fields shown in Fig. 10(b)–(d).

decays more quickly because it is sensitive to internal-wave-induced perturbations of all propagating modes.

IV. SUMMARY AND CONCLUSIONS

This paper reports the findings of a broad computational study of time-reversing array retrofocusing in the shallow ocean with a water-column-spanning array. The influences of source depth, source–array range, acoustic frequency, bottom absorption, internal-wave strength, and time delay have all been presented. Although the many specific parametric and geometric choices have been guided by measurements made during the SWARM experiment, the parametric studies presented here should encompass a large fraction of all shallow ocean environments, and should be readily extendable to mildly range-dependent environments.

There are three main conclusions that can be drawn from this study. First, modal propagation sets limits on TRA retrofocusing in a static sound channel. When the acoustic frequency is higher and more modes are available, TRA retrofocusing is better and extends to longer ranges. Similarly, when the initial source lies in the lower portion of the sound channel where the speed of sound gradient is weak and many modes have both nodes and antinodes, time-reversing array

retrofocusing is enhanced compared to that computed for shallow sources that primarily excite more rapidly attenuated high-order acoustic modes. In fact, the ultimate source–array range for TRA retrofocusing in quiescent shallow-water sound channels will be set by mode stripping caused by bottom and bubble absorption, and scattering losses from the bubbles and the ocean's free surface.

The second main conclusion is that internal-wave-induced fluctuations actually aid TRA retrofocusing for short time delays (a minute or less at source–array ranges of 10 km) mainly by suppressing sidelobes, but do eventually degrade retrofocusing at longer times (tens of minutes at source–array ranges of 10 km). The beneficial effects come about because internal waves induce mode coupling that allows low-order modes to properly scatter into higher orders as the backward-propagating signal nears the original source location. Such scattering increases the acoustic energy in the higher-order modes compared to the same signal in a sound channel without internal waves, and leads to a slightly smaller retrofocus with lower sidelobes. However, the beneficial effects of this internal-wave-induced mode coupling are lost when the time delay is large enough for the internal-wave dynamics to significantly change the refractive index structure in the sound channel. As expected, significant
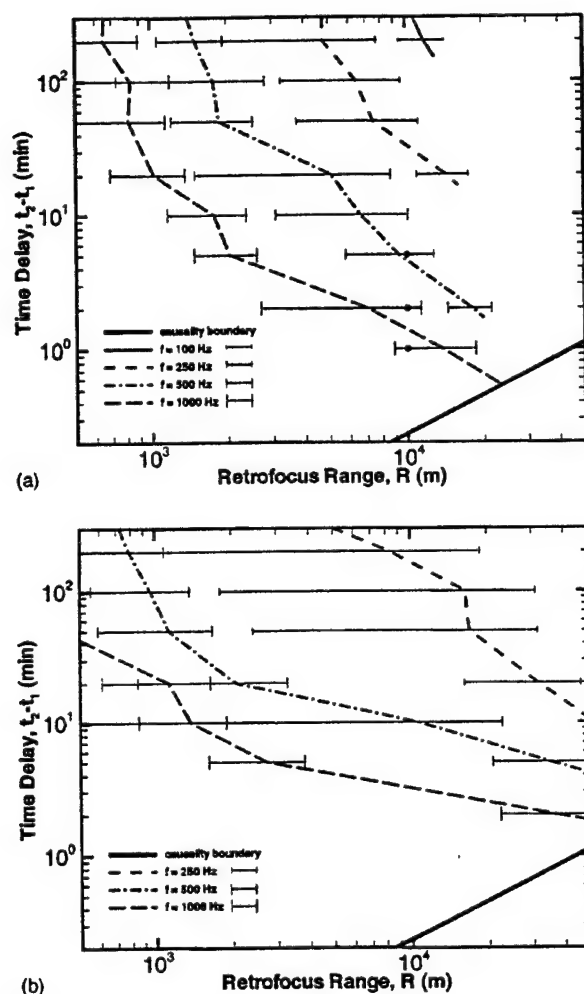
(a)

(b)

FIG. 12. Time-reversing array performance envelopes for variable source–array range (R) and time delay ($t_2 - t_1$) with SWARM-strength internal waves. The contours are the loci of the retrofocus half life at each frequency $f = 100$ Hz (———), 250 Hz (---), 500 Hz (-·-·), and 1 kHz (– – –). The plotted curves correspond to the average of 20 trials. Above and to the right of these contours, the TRA retrofocus amplitude is predicted to have fallen to half its value in a frozen shallow ocean ($t_2 - t_1 = 0$). The upward-sloping diagonal line is the causality boundary. Realizable TRA systems must operate above and to the left of this line. Frame (a) is for a source depth $z_s = 25$ m, and frame (b) is for a source depth $z_s = 50$ m. The deeper source leads to retrofocusing at longer ranges, but the shallow source produces a longer-lasting retrofocus. The 100-Hz curve lies off the figure in (b). The error bars denote the 50%-confidence interval for each half-life curve. The black dots in (a) correspond to the fields shown in Fig. 10(b)–(d).

changes occur more rapidly at longer source–array ranges and higher acoustic frequencies. Decreasing the frequency increases the delay time before internal-wave degradation of the retrofocus but also increases the retrofocus size. However, some minimum number of propagating modes (ten or so) is required to retrofocus properly (depending on source depth), and this sets a lower limit on the acoustic frequency that could be used for successful TRA operations.

Finally, for an active internal-wave environment such as that found during the SWARM experiment, the source–array range limitation imposed by the internal waves is likely to be more severe than that imposed by bottom losses. In less ac-

tive environments, absorption losses are likely to set the ultimate source–array range.

ACKNOWLEDGMENTS

Apel, J. R., Badiey, M., Chiu, C.-S., Finette, S., Headrick, R., Kemp, J., Lynch, J. F., Newhall, A., Orr, M. H., Pasewark, B. H., Tielbürger, D., Turgut, A., von der Heydt, K., and Wolf, S. (1997). "An overview of the 1995 SWARM shallow-water internal wave acoustic scattering experiment," IEEE J. Ocean Eng. 22, 465–500.

Collins, M. D. (1993). "A split-step Padé solution for parabolic equation method," J. Acoust. Soc. Am. 93, 1736–1742.

Collins, M. D. (1994). "Generalization of the split-step Padé solution," J. Acoust. Soc. Am. 96, 382–385.

Collins, M. D. (1998). "New and improved parabolic equation models," J. Acoust. Soc. Am. 104, Pt. 2, 1808.

Dashen, R., Munk, W. H., Watson, K. M., and Zachariasen, F. (1979). In Sound Transmission Through a Fluctuating Ocean, edited by S. M. Flatté (Cambridge University Press, Cambridge).

Derode, A., Roux, P., and Fink, M. (1995). "Robust acoustic time reversal with high-order multiple scattering," Phys. Rev. Lett. 75, 4206–4209.

Dowling, D. R., and Jackson, D. R. (1992). "Narrow-band performance of acoustic phase-conjugate arrays in dynamic random media," J. Acoust. Soc. Am. 91, 3257–3277.

Dowling, D. R. (1993). "Phase-conjugate array focusing in a moving medium," J. Acoust. Soc. Am. 94, 1716–1718.

Dowling, D. R. (1994). "Acoustic pulse compression using passive phase-conjugate processing," J. Acoust. Soc. Am. 95, 1450–1458.

Fink, M. (1997). "Time reversed acoustics," Phys. Today 50, No. 3, 34–40.

Finette, S. (1998). Private communication.

Garrett, C., and Munk, W. (1979). "Internal waves in the ocean," Annu. Rev. Fluid Mech. 11, 339–369.

Hodgkiss, W. S., Kuperman, W. A., and Song, H. C. (1997). Private communication.

Jackson, D. R., and Dowling, D. R. (1991). "Phase-conjugation in underwater acoustics," J. Acoust. Soc. Am. 89, 171–181.

Jensen, F. B., Kuperman, W. A., Porter, M. B., and Schmidt, H. (1994). Computational Ocean Acoustics (AIP, New York), p. 41.

Khosla, S. R., and Dowling, D. R. (1998). "Time-reversing array retrofocusing in simple dynamic underwater environments," J. Acoust. Soc. Am. 104, 3339–3350.

Kuperman, W. A. (1997). Private communication.

Kuperman, W. A., Hodgkiss, W. S., Song, H. C., Akal, T., Ferla, C., and Jackson, D. R. (1998). "Phase-conjugation in the ocean: Experimental demonstration of an acoustic time reversal mirror," J. Acoust. Soc. Am. 103, 25–40.

Parvulescu, A. (1995). "Matched-signal (MESS) processing by the ocean," J. Acoust. Soc. Am. 98, 943–960.

Press, W. H., Flannery, B. P., Teukolsky, S. A., and Vetterling, W. T. (1986). Numerical Recipes (Cambridge University Press, Cambridge), Chap. 16.

Rose, J. H., Bilgen, M., Roux, P., and Fink, M. (1999). "Time-reversal mirrors and rough surfaces: Theory," J. Acoust. Soc. Am. 106, 716–723.

Roux, P., De Rosny, J., and Fink, M. (1999). "Time reversal mirrors and rough surfaces: Experiment," J. Acoust. Soc. Am. 106, 724–732.

Saichev, A. I. (1982). "Effect of compensating distortions due to scattering in an inhomogeneous medium by the use of a reflector turning the front," Radio Eng. Electron. Phys. 27, 23–30.

Song, H. C. (1998). Private communication.

Song, H. C., Kuperman, W. A., and Hodgkiss, W. S. (1998). "A time-reversal mirror with variable range focusing," J. Acoust. Soc. Am. 103, 3234–3240.

Tanter, M., Thomas, J.-L., and Fink, M. (1998). "Focusing and steering through absorbing and aberrating layers: Application to ultrasonic propagation through the skull," J. Acoust. Soc. Am. 103, 2403–2410.

Tielbürger, D., Finette, S., and Wolf, S. (1997). "Acoustic propagation through an internal wave field in a shallow water waveguide," J. Acoust. Soc. Am. 101, 789–808.

Yang, T. C., and Yoo, K. (1998). "Frequency spectrum of linear internal waves in shallow water and a modified Garrett–Munk model," J. Acoust. Soc. Am. 104, 1765(A).

Yönak, S. H., and Dowling, D. R. (1999). "Photoacoustic detection and localization of small gas leaks," J. Acoust. Soc. Am. 105, 2685–2694.

Yoo, K., and Yang, T. C. (1998). "Measurements of modal spectrum of linear internal waves in shallow water and comparison with the Garrett–Munk model," J. Acoust. Soc. Am. 104, 1765(A).

Computed narrowband azimuthal time-reversing array retrofocusing in shallow water

(Revised for *The Journal of the Acoustical Society of America*, 11/00)

Michael R. Dungan and David R. Dowling
Dept. of Mechanical Engineering and Applied Mechanics, University of Michigan, Ann Arbor, MI 48109-2121

Abstract

The process of acoustic time reversal sends sound waves back to their point of origin in reciprocal acoustic environments even when the acoustic environment is unknown. The properties of the time-reversed field commonly depend on the frequency of the original signal, the characteristics of the acoustic environment, and the configuration of the time-reversing transducer array (TRA). In particular, vertical TRAs are predicted to produce horizontally-confined foci in environments containing random volume refraction. This paper validates and extends this prediction to shallow water environments via monochromatic Monte-Carlo propagation simulations (based on parabolic equation computations using RAM). The computational results determine the azimuthal extent of a TRA's retrofocus in shallow-water sound channels either having random bottom roughness or containing random internal-wave-induced sound speed fluctuations. In both cases, randomness in the environment may reduce the predicted azimuthal angular width of the vertical-TRA retrofocus to as little as several degrees (compared to 360° for uniform environments) for source-array ranges from 5 to 20 km at frequencies from 500 Hz to 2 kHz. For both types of randomness, power law scalings are found to collapse the calculated azimuthal retrofocus widths for shallow sources over a variety of acoustic frequencies, source-array ranges, water column depths, and random fluctuation amplitudes and correlation scales. Comparisons are made between retrofocusing on shallow and deep sources, and in strongly and mildly absorbing environments.

PACS: 43.30Vh, 43.30Yj, 43.30Ft

Introduction

Acoustic time reversal is a promising technique for acoustic-array beamforming in unknown multipath environments. The transducer array that produces the time reversed field (a time-reversing array or TRA) may be of nearly any size or shape and can operate in any frequency range. Recent computational and experimental TRA studies in underwater acoustics (Kuperman et al. 1998, Song et al. 1998a, Khosla & Dowling 1998, Song et al. 1999, Hodgkiss et al. 1999) suggest that TRAs can robustly retrofocus sound on remote sound sources in shallow ocean waters. TRA research has also been pursued in the area of bio-medical ultrasound (Fink 1997, 1999, Tanter 1998, Rose et al. 1999, Roux et al. 1999a), nondestructive evaluation (Chakroun et al. 1995, Draeger et al. 1998, Yönak & Dowling 1999), and other areas (Draeger et al. 1999ab,

Ohno et al. 1999, Yamamoto et al. 1999, Roux et al. 1999b). The basic formulation of acoustic time reversal is provided in Jackson and Dowling (1991). Overviews are provided in Fink (1997, 1999).

Unlike ordinary beamforming techniques (Steinberg 1976, Ziomek 1985), time reversal actually utilizes the acoustic environment to retrofocus sound so TRAs perform better when random scattering and multipath propagation are present, although TRA performance is generally degraded in time-dependent (Dowling & Jackson 1992, Khosla & Dowling 1998, Dungan & Dowling 2000) and noisy environments (Song et al. 1998a, Khosla & Dowling 2000). This paper presents new computational results and scaling laws for azimuthal beam forming by a linear vertical TRA responding to a harmonic point source at a range R from the TRA in a low-noise time-independent shallow water sound channel. When the environment is horizontally uniform, this source-TRA configuration produces a retrofocus ring of radius R with an azimuthal angular extent of 360°. However, this same array placed in a horizontally inhomogeneous environment can produce a time-reversed field that includes significant azimuthal focusing (beamforming) in the direction of the point source. The purpose of this paper is to provide predictions of the extent of this environmentally-produced retrofocusing in shallow-water sound channels having either bottom roughness or containing sound speed fluctuations produced by a linear superposition of random internal waves convecting a sound speed gradient.

This azimuthal environmentally-produced retrofocusing is generated by the two-step propagation algorithm for a time-reversing array. During the source-to-array propagation step, the sound signal is imprinted with the environmental characteristics between the source and the array. The array receives the imprinted signal, time reverses it (i.e. first-in becomes last-out), and rebroadcasts it. During this rebroadcast step, the vertical TRA directs acoustic energy uniformly into all azimuthal angles ($0 \leq \phi < 360°$). However, only the sound that retraces the direction ($\phi = 0$) back toward the source focuses because the TRA's rebroadcast field is mismatched to the details of the environment in all other directions ($\phi \neq 0$). This preferred-direction focusing phenomena is essentially the same as the environmental signal-processing gain described in Perkins & Kuperman (1990) in the context of matched field processing; the difference is the present paper emphasizes the effects of randomness as opposed to deterministic three-dimensional features of the ocean sound channel. Acoustic underwater communication is one application area where the benefits of robust focusing in unknown and changing environments are important and where TRA techniques are currently receiving attention.

Previous studies of TRA horizontal focusing have been limited. Song et al. (1998b) investigated the horizontal dimension of a retrofocus spot in their unique experiments conducted in the Mediterranean Sea (Kuperman et al 1998, Song et al. 1998a, 1999, Hodgkiss et al. 1999). However, their efforts on this topic were confined to a single source-array track, acoustic frequency, and source-array range. Past analytical and computational studies of time reversal in shallow ocean waters (Khosla & Dowling 1998, Dungan & Dowling 2000) have emphasized vertical retrofocus size without considering horizontal focusing in any detail, although a tenuous theoretical prediction was advanced in Khosla & Dowling (1998). The computational results and scaling laws presented here are intended to complement these previous studies to provide a means of quantitatively predicting the horizontal or azimuthal retrofocus size produced by vertical TRAs in horizontally non-uniform environments.

The remainder of this paper is organized into three sections. The next section describes the acoustic environment used in this study, the bottom variation and internal wave models, and the computational technique. Section II presents the vertical and azimuthal retrofocus simulation results along with proposed scaling laws and comparisons. The final section summarizes the findings and states the conclusions drawn from this study.

I. Computational Approach

This study utilizes repeated two-dimensional (2D) simulations in depth-range planes that fan out from the array to predict azimuthal TRA retrofocusing, a three-dimensional (3D) phenomena. This technique, commonly called the N×2D approach to 3D simulations, has been successfully exploited in previous underwater simulation studies. Here, each propagation slice is computed with the wide-angle parabolic-equation code RAM (Collins 1993, 1994, 1998). The goal of this study is to predict how vertical-TRA azimuthal retrofocus size is influenced by environmental parameters, source-array geometry, and acoustic frequency (f). The following four subsections describe the environment investigated, the bottom variation model, the internal wave model, and the implementation of these within RAM.

A. Average Environment

The shallow ocean is a complicated acoustic environment. Here, the main parametric complication is random bottom roughness added to a static baseline range-independent sound-channel. Figure 1 shows a 3D representation of the simulation environment with bottom

3

roughness and mean depth $D = 75$ m. Water column and smooth-bottom properties are based on oceanic measurements taken near the center of the SWARM (shallow-water acoustics in a random medium) site (see Apel et al. 1997). The SWARM experiment was conducted off the coast of New Jersey in the late summer of 1995 during a seasonally active time for internal waves. The actual SWARM water column depth was range dependent (seaward sloping bottom) and the bottom contained multiple layers, but these complexities were not included in the present study. The speed of sound profile used here, shown in Fig. 2(a), is calculated from smoothed temperature and salinity measurements made at the center of the SWARM site in the absence of internal wave solitons. Figure 2(b) shows the calculated root-mean-square speed of sound fluctuations when synthetic internal waves (see subsection I.C.) are included in the sound channel. For all the simulations, the average bottom is a two layer model with properties extrapolated from core and chirp measurements at the SWARM site (Apel et al. 1997). The 23 m thick upper layer has a speed of sound of 1650 m/s and a density of 1.70 kg/m^3, and the lower layer is modeled as a half-space with a speed of sound of 1950 m/s and a density of 2.20 kg/m^3. Attenuation values were extrapolated from tabulations in Jensen et al. (1994) and are 1.00 decibel per wavelength and 0.40 decibel per wavelength for the upper and lower layers, respectively. The roughness model (described in the next subsection) was not based on SWARM measurements.

The ocean surface is treated as a flat pressure-release surface. Although this is clearly an approximation for acoustic frequencies in the kHz range and above, the complications posed by bubble scattering, bubble absorption, and dynamic rough ocean-surface scattering are beyond the scope of this study. Assessments of rough surface scattering and TRA performance are provided in Kuperman et al. (1998) and Khosla & Dowling (1998).

The parameters just described above will be the same throughout the rest of this paper unless stated otherwise. The exceptions will be for: i) variations in attenuation values that illustrate the role of bottom absorption, ii) different bottom roughness levels (described in the next subsection), iii) vertical stretching (see discussion of Fig. 11), and iv) fluctuations in the speed of sound profile caused by random linear internal waves.

B. Bottom Variation

In this study, the ocean bottom is taken to be flat, on average, with a zero-mean spatially-varying random roughness height $H(r,\phi)$ of the first bottom layer. The local depth, z_b, of the sound channel at a given (r,ϕ) location is the sum of the mean depth $D = 75$ m and H:

$$z_b(r,\phi) = D + H(r,\phi) \tag{1}$$

Most ocean-bottom surveys agree on a statistical variation model involving a power law distribution of the spectrum of H, $\Phi_H(k_h)$, with horizontal spatial frequency k_h:

$$\Phi_H(k_h) \propto k_h^{-b}. \tag{2}$$

Bell (1975) tabulated bottom roughness spectral data from various experiments. Berkson & Matthews (1984), Fox & Hayes (1985), Jackson et al. (1986), and Medwin & Clay (1998) also present or use bottom roughness spectral data in the form of a power law but some differences exist between recommended values of the exponent b.

In this study, H is synthesized from a random superposition of sinusoidal roughness height fluctuations whose statistics are azimuthally isotropic:

$$H(r,\phi) = \sum_{k_h} \sum_{\theta} F(k_h) e^{ik_h r \cos\phi \cos\theta + ik_h r \sin\phi \sin\theta}, \tag{3}$$

where θ represents the azimuthal angles of the roughness height sinusoids ($0 < \theta < 360°$), and $F(k_h)$ is a random complex amplitude having a power spectrum in k_h given by

$$\left\langle |F(k_h)|^2 \right\rangle = C_0^2 H_{RMS}^2 \left(\frac{k_h^2}{k_h^2 + k_l^2} \right)^{\alpha} k_h^{-b} \left(\frac{k_u^2}{k_h^2 + k_u^2} \right)^{\beta}. \tag{4}$$

The real and imaginary components of $F(k_h)$ are Gaussian-distributed with zero mean, and the angle brackets denote an expected value. The power law exponent used here is $b = 2.0$ and the maximum root-mean-square (RMS) depth variation is $H_{RMS} = 3.0$ m. These values are based on Table I in Berkson & Matthews (1984) (see also Table 13.1 in Medwin & Clay 1998). The extra factors in (4) compared to (2) exist to smooth the depth fluctuation spectrum in the regions of the lower- and upper-cutoff horizontal wavenumbers, k_l and k_u, respectively. The normalization constant in (4), C_o^2, is chosen so that

$$H_{RMS}^2 = \int_0^\infty \left\langle |F(k_h)|^2 \right\rangle dk_h \tag{5}$$

The remaining parametric choices necessary to evaluate (4) consist of roll-off exponents ($\alpha = 3$ and $\beta = 2$) and upper and lower wave numbers ($k_u = 0.001$ m^{-1} and $k_l = 0.06$ m^{-1}). The final depth fluctuation spectrum is shown in Fig. 3 for $H_{RMS} = 3.0$ m. The correlation length Λ produced by this bottom roughness model was 280 m, and was computed from

$$\Lambda = \frac{1}{H_{RMS}^2} \int_0^\infty \langle H(r,\phi)H(r+\Delta r,\phi) \rangle d\Delta r \tag{6}$$

In computing the sum shown in (3), discrete k_h steps of $\Delta k_h = 0.0005$ m^{-1} were taken. The number of θ-direction waves increases linearly with k_h to attain nearly uniform tiling of the k_h-θ plane. One realization of the bottom roughness with $H_{RMS} = 3.0$ m and RMS slope of 0.02 is shown in Fig. 4. Although some remnants of the discrete sinusoid sum are apparent, the depth variations are not unrealistic. Superimposed on Fig. 4 is a sample retrofocus grid with the TRA on the left and the various source locations (white dots) and azimuthal sample points on the right. Notice that the bottom roughness profile found between the various return paths and the initial source-array path may differ significantly. This paper presents the result of investigations into the importance of such variations in bottom roughness on TRA retrofocusing.

C. Linear Internal Waves

To compare the importance of bottom roughness and water-column random refraction on azimuthal retrofocusing by vertical TRAs, linear internal waves were inserted into the baseline sound channel described in subsection A. The internal-wave model is a superposition of random linear waves having a Garrett-Munk spectrum that is adjusted for shallow ocean conditions. It is the model used by Dungan and Dowling (2000) and is a simple extension on the formulation of Dashen et al. (1979) and Tielbürger et al. (1997).

Internal waves cause heaving motions within the water column that alter the local sound speed by lifting and lowering the otherwise static contours of constant sound speed. These imposed variations produce a 3D sound-speed field that depends on r and ϕ, as well as z. The vertical deflections produced by internal waves are governed by a second-order differential equation (Dashen et al. 1979)

6

$$\frac{d^2}{dz^2} W(z) + k_h^2 \left[\frac{N^2(z) - \omega^2}{\omega^2 - f_c^2} \right] W(z) = 0, \tag{7}$$

which, along with the waveform boundary conditions of $W(0) = W(D) = 0$, creates an eigenvalue problem. Here, $W(z)$ is the vertical displacement produced by an internal wave having radian frequency ω, k_h is the horizontal wavenumber of the internal wave, and $f_c = 2\Omega \sin(°\text{latitude})$ is the inertial frequency with Ω equal to the rotation rate of the earth. For these calculations, f_c was evaluated at a latitude of 39.25°, corresponding to the center of the SWARM site. When ω and k_h are independent parameters, (7) has eigenmode solutions $W(k_h, j, z)$ at a discrete set of frequency eigenvalues $\omega_j(k_h)$. The internal wave modes and frequencies particular to this study were calculated from (7) numerically using shooting techniques (see Press et al. 1986). Hence, a dynamic three-dimensional simulation of the internal-wave-induced vertical displacement η can be obtained by a triple sum over internal-wave modes (j), horizontal wavenumbers (k_h), and azimuthal angles (θ),

$$\eta(r,\phi,z,t) = \text{Re}\left\{ \sum_j \sum_{k_h} \sum_\theta F(k_h, j) W(k_h, j, z) \exp\left[ik_h r \cos\theta \cos\phi + ik_h r \sin\theta \sin\phi - i\omega(k_h, j)t \right] \right\}. \tag{8a}$$

The F-term is a Gaussian random complex weighting having a uniform distribution in θ and a Garrett-Munk spectrum in mode number and horizontal wavenumber

$$\left\langle |F(k_h, j)|^2 \right\rangle = \frac{4}{\pi} E_o M \left[j^2 + j_*^2 \right]^{-p/2} k_j k_h^2 (k_h^2 + k_j^2)^{-2}, \tag{8b}$$

where:
$$k_j = \frac{\pi j f_c}{\int_o^D N(z)\,dz}, \quad \text{and} \quad M = \left\{ \sum_{j=1}^{\infty} (j^2 + j_*^2)^{-p/2} \right\}^{-1} \tag{8c,d}$$

Here, E_o is the internal-wave energy level, j_* is the mode weighting parameter, and p is the mode weighting exponent. As with (3), the sum given in (8a) was calculated using a variable azimuthal resolution so that random numbers were assigned to approximately equal tile areas of the k_h-θ plane for each value of j. Hence the number of θ-evaluations in (8a) increased linearly with increasing k_h. The parametric ranges and increments used for summation were: $1 \le j \le 15$, 5×10^{-4}

$m^{-1} \leq k_h \leq 1.5 \times 10^{-1}$ m^{-1} with steps of $\Delta k_h = 5 \times 10^{-4}$ m^{-1}, and $0 \leq \theta \leq 360°$ with $\Delta \theta = 2°$ when $k_h = 1.5 \times 10^{-1}$ m^{-1}. The internal wave mode shapes $W_j(z, k_h)$ evolve gradually with increasing k_h, so mode shapes were interpolated between the minimum and maximum values of k_h with intervening calculations every 10^{-2} m^{-1}.

The Garrett-Munk spectrum parameters (E_o, p, j_*) were chosen to match a temporal power spectrum of vertical displacements measured at the SWARM site in 75 m of water without soliton activity. This was accomplished by using (8a) at a fixed depth of 25 m to generate a synthetic vertical displacement time series, computing the power spectrum from this synthetic time series, and then comparing the resulting synthetic spectrum with the SWARM measurements. Adjustments were made to the spectrum parameters until a visually acceptable match of the two spectra was achieved (see Dungan & Dowling 2000). The final parameter choices are $j_* = 1$, $p = 4$, and $E_o = 24.6$ J/m^2. Other independent research suggests similar values for these parameters (Tielbürger et al. 1997, Yoo & Yang 1998, Yang & Yoo 1998). The final speed of sound fluctuation levels, shown in Fig. 2(b), are confined to the upper half of the sound channel.

D. Propagation Model

Acoustic propagation in the roughened and internal-wave containing sound channels is computed with RAM, a wide-angle parabolic equation (PE) code (Collins, 1993, 1994, and 1998). Previous use of RAM in the context of narrowband TRA simulations has been described in Dungan & Dowling (2000). The use of RAM here is nearly identical, the only difference being the extension to N×2D calculations to determine the azimuthal extent of the TRA retrofocus region.

To summarize, a modified version of RAM that outputs the real and imaginary components of the pressures was used so that amplitudes at the TRA locations could be complex conjugated before the back-propagation was computed. Complex conjugation is the equivalent of time reversal for narrowband signals (Jackson & Dowling 1991). In the forward propagation step (at time t_1), a point source with radian frequency ω located at $(r, \phi, z) = (R, 0, z_s)$ ensonifies the sound channel. Elements of the TRA located at $(0, 0, z_n)$, record this field, complex conjugate it, amplify it, and rebroadcast it (at time t_2). The response of such an array is entirely described by the conjugate Green's function, $G_{c\omega}$ [see Dowling & Jackson (1992) Eq. (10), or Kuperman et al. (1998) Eq. (7)]:

8

$$G_{c\omega}(r,\phi,z,t_2-t_1) = \sum_{n=1}^{N} G_{2\omega}(r,\phi,z;0,0,z_n)G_{1\omega}^{*}(0,0,z_n;R,0,z_s) \tag{9}$$

where N is the number of array elements and the coordinates are shown on Fig. 1. Here, $G_{1\omega}(0,0,z_n;R,0,z_s)$ is the Green's function at radian frequency $\omega = 2\pi f$ for acoustic propagation from the source at $(R,0,z_s)$ to an array element at $(0,0,z_n)$ for time t_1, and the asterisk denotes complex conjugation. Similarly, $G_{2\omega}(r,\phi,z;0,0,z_n)$ is the Green's function for acoustic propagation from an array element at $(0,0,z_n)$ to (r,ϕ,z) for time t_2. For all retrofocusing computations in the baseline sound channel, the array has 24 elements with 3-meter vertical spacing, and the time delay, $t_2 - t_1$, is set to be zero for simplicity.

The use of the N×2D approach to calculate the 3D features of $G_{2\omega}(r,\phi,z;0,0,z_n)$ requires some consideration. Much work has been done to determine the applicability of N×2D approximations to 3D problems. Buckingham (1984) and Sturm et al. (1998) have shown that this approximation does not fare well in a full-wedge sound channel. However, Kuperman et al. (1991), Smith (1998), and others have shown that for mild range-dependence, the N×2D approach closely models three dimensions and even predicts some 3D effects like horizontal refraction (Smith 1996, 1998). The bottom roughness and internal wave-field environments generated to obtain the current results are mild enough to be treated with acceptable accuracy by the N×2D approximation.

II. TRA Retrofocusing Results

The results of this investigation into the environment's effect on the retrofocusing capability of a time reversing array are presented in three parts. The first two subsections investigate an environment with a varying bottom and its impact on vertical and azimuthal retrofocusing, respectively. The final subsection explores the impact of linear internal waves on azimuthal retrofocusing. A more thorough study of TRA retrofocus amplitude and vertical extent in static and dynamic shallow-water sound channels is provided in Dungan & Dowling (2000).

A. Vertical Retrofocusing with Random Rough Bottom

The performance of the TRA in the $\phi = 0$ vertical plane of the baseline sound channel with varying bottom geometry was investigated as a preliminary study to the azimuthal retrofocusing

investigations. The results are found by calculating $G_{c\omega}$ from (9) at $r = R$ and $\phi = 0$, and determining the vertical size of the retrofocus region. The parameters varied in this case include source depth (z_s = 25 and 50 m), acoustic frequency (f = 250, 500, 1000, and 2000 Hz), and RMS depth fluctuation (H_{RMS} = 0, 1.0, 2.0, and 3.0 m). The parameters cover a range $0 \le kH_{RMS} \le 25$, where k is the acoustic wavenumber. For these initial studies, the source-array range was held fixed at $R = 10$ km.

The vertical retrofocus size results are given in Table I which lists the TRA-retrofocus-peak full-width-at-half-maximum (FWHM) values through the depth, z_{FWHM}, divided by the acoustic wavelength λ. These results show that z_{FWHM} lies in the range of three to four wavelengths for the entire parameter range with the shallow source (z_s = 25 m) providing a somewhat smaller retrofocus. These results are based on 10 realizations of the bottom roughness at each H_{RMS} value.

Interestingly, increasing RMS depth fluctuation does not lead to consistent changes in z_{FWHM} or even to higher uncertainty values for z_{FWHM}. Thus, the main conclusion to be drawn from these results is that bottom roughness does not have a significant effect on vertical retrofocus size in this parameter range when $\phi = 0$.

B. Azimuthal Retrofocusing with a Random Rough Bottom

The azimuthal extent of the TRA retrofocus was investigated for the baseline sound channel with varying levels of bottom roughness. The results are found by calculating $G_{c\omega}$ from (9) at $r = R$ and $\phi \ne 0$, and determining the azimuthal angular size of the retrofocus peak. The parameters varied in this case cover the same parametric range as the vertical retrofocus size study but also include four source-array ranges $R = 2.5, 5, 10$, and 20 km.

Whereas the increase in bottom roughness has little or no effect on the TRA's vertical retrofocus size, the azimuthal retrofocus size is strongly dependent on both roughness and range, and decreases as both increase. An example is shown in Fig. 5 for the results of one bottom roughness realization captured by looking at different ϕ-angles at a constant range ($R = 10$ km) to produce an N×2D composite image. The projected geometry for the images shown in Fig. 5 is sketched in Fig. 6. The TRA's retrofocus for the baseline smooth-bottom sound channel [$H(r,\phi,)$ = 0.0 m] is an unvarying 360° ring as partially shown for a 500 Hz source at z_s = 25 m in Fig. 5(a). As the bottom roughness increases (H_{RMS} = 0.75 m, H_{RMS} = 1.5 m, and H_{RMS} = 3.0 m), the azimuthal retrofocus size decreases [Figures 5(b), 5(c), and 5(d), respectively]. This environment-enhanced focusing becomes stronger as H_{RMS} increases. Sidelobes that occur in the lower half of

the sound channel when $\phi \neq 0$ are caused by acoustic energy that was unintentionally broadcast at that azimuthal angle by the linear vertical TRA. These azimuthal sidelobes are not caused by mode stripping and would contribute to the 360°-ring retrofocus if $H_{RMS} = 0$. They occur in the lower half of the sound channel because of the channel's strongly downward-refracting sound speed profile.

The azimuthal retrofocus size also decreases as the source-array range increases (up to a point where absorption degrades the retrofocus). Figure 7 shows this development for a 500 Hz source at $z_s = 25$ m for $R = 2.5, 5, 10,$ and 20 km. As R increases, the importance of bottom scattering increases and the acoustic waves traveling on bottom interacting paths become increasingly more imprinted with the particular bottom roughness profile lying between the source and the array. On the array-to-source propagation step, the TRA's rebroadcast field only retrofocuses in the angular region where the bottom roughness profile felt by the back-propagating waves is closely matched to the source-array bottom roughness profile. At longer ranges, this angular region of bottom-profile match is reduced because of increased bottom scattering and geometrical considerations. The linear vertical TRA still spreads acoustic power uniformly into all possible azimuthal directions (i.e. 360°); however, the rebroadcast field fails to focus in any direction except that towards, or nearly towards, the original source ($\phi \approx 0$). The misdirected acoustic energy leads to the side lobe structure in Figs. 5 and 7.

The azimuthal retrofocus size can be quantified in terms of an angular full-width at half-maximum (FWHM), ϕ_{FWHM}, defined as the angular extent over which the TRA-produced pressure amplitudes are more than half of the peak pressure found at $(R, 0, z_s)$. Figure 8 displays the range dependence of ϕ_{FWHM} for source depths of 25 and 50 m at four acoustic frequencies for $H_{RMS} = 3.0$ m based on 10 different realizations of the bottom roughness. The range values on the horizontal axes in Fig. 8 are both scaled by the acoustic wavenumber $k = 2\pi f/c$ where $c = 1500$ m/s. The slope triangle provided on Fig. 8 suggests $\phi_{FWHM} \propto (kR)^{-3/2}$. These scaled plots show that the shallow source case [Fig. 8(a)] produces a frequency-independent rate of decrease in ϕ_{FWHM} with increasing source-array range followed by an upturn that depends on frequency. The pattern is similar but less well defined for the deep source [Fig. 8(b)]. This difference is believed to arise from the comparative dominance of low order modes for deep-source retrofocusing when compared to shallow-source source retrofocusing in the same channel. The low order propagating modes are less susceptible to bottom absorption and perturbations from bottom roughness so the deep source ($z_s = 50$ m) produces larger azimuthal retrofoci than the shallow source ($z_s = 25$ m).

11

Recall that vertical-TRA azimuthal retrofocusing is only possible when there is significant propagation perturbations caused by variations in the bottom (or water column).

The frequency dependent upturns in ϕ_{FWHM} shown on Fig. 8 occur because of bottom absorption that preferentially effects the higher order modes. To verify this claim, cases were run at 500 Hz and $H_{RMS} = 3.0$ m with varying attenuation values in the two bottom layers. The cases studied include one quarter (0.25 & 0.10 dB/λ), one half (0.50 & 0.20 dB/λ), one (1.00 & 0.40 dB/λ), and two (2.00 & 0.80 dB/λ) times the nominal attenuation values specified in Sec. I.A. Figure 9 shows these results for $z_s = 25$ m [Fig. 9(a)], and $z_s = 50$ m [Fig. 9(b)]. As in Figs. 8, the horizontal axis is kR. For the shallow source [Fig. 9(a)] as the attenuation values drop, there is an increase in the range at which the azimuthal sharpening trend reverses. For the deep source [Fig. 9(b)], the results also show sharper azimuthal retrofocusing for lower attenuation values. These results support the contention that the upturns in ϕ_{FWHM} with increasing R are caused by the absorption of the higher-order propagating modes.

To quantify the effect of bottom roughness height on azimuthal retrofocusing, ϕ_{FWHM}, was calculated at 500 Hz for $H_{RMS} = 0.75$, 1.5 and 3.0 meters. Figure 10 displays these results for $z_s = 25$ m [Fig. 10(a)] and $z_s = 50$ m [Fig. 10(b)], respectively. As in Figs. 8 and 9, the horizontal axis is kR. A smooth-bottom case produces a 360° retrofocus and therefore does not appear on either frame of Fig. 10. The remaining curves indicate an impressive sharpening of the retrofocus as the bottom roughness increases with the shallow ($z_s = 25$ m) source leading to consistently smaller retrofoci than the deep ($z_s = 50$ m) source for ranges greater than 5 km ($kR \approx 10^4$) and $H_{RMS} = 3.0$ m. Interestingly, the predicted azimuthal extent of the vertical TRA's retrofocus falls below 5° for both source depths when $H_{RMS} = 3.0$ m. In addition, the effects of absorption are delayed to longer ranges for smaller H_{RMS}. This is due to the higher amount of bottom absorption present when H_{RMS} is greater, since local grazing angles for bottom scattering and penetration are increased by increased bottom roughness.

The trends found in Figs. 8-10, suggest a simple power-law scaling is possible for the azimuthal size of the TRA retrofocus. Arguments leading to such a scaling law are presented in the next few paragraphs along with figures showing the scaling law's effectiveness for TRA retrofocusing on shallow and deep sources.

A TRA retrofocus field forms when the phase of the original forward-propagated field is precisely cancelled by the back-propagated field. Thus, the net phase at a TRA retrofocus is zero when the propagation is reciprocal and scattering from the bottom roughness along the source-

array path ($\phi = 0$) is compensated. If the phase of the back-propagated field is sufficiently altered compared to the forward propagated field, the constructive interference that forms the retrofocus will not occur and the retrofocus will be weakened or even lost. When the ocean bottom is rough, such uncompensated phase variations will occur in the TRA's back-propagated field along azimuthal directions ($\phi \neq 0$) other than that toward the source ($\phi = 0$) because of uncompensated scattering from the differing bottom roughness features lying along $\phi \neq 0$ paths.

The extent of such phase variations can be estimated by comparing the TRA's back-propagated field that travels at $\phi = 0$, $G_{c\omega}(r,0,z)$, and the TRA's back-propagated field that travels at a small nonzero azimuthal angle ϕ, $G_{c\omega}(r,\phi,z)$, Here, the phase difference at the source depth, z_s, between these two field values is denoted by η, i.e. $G_{c\omega}(r,0,z_s,0)G_{c\omega}^{*}(r,\phi,z_s,0) \propto e^{i\eta}$. Although the expected value of η will be zero, its variance, $\langle \eta^2 \rangle$, increases with increasing k, R, ϕ, and H_{RMS} because of uncompensated bottom scattering along the $\phi \neq 0$ path. When $\langle \eta^2 \rangle$ is of order unity or greater, the TRA retrofocus in ϕ-direction will have been weakened or even eliminated because of uncompensated bottom scattering. Therefore, ϕ_{FWHM} should be proportional to the value of ϕ that produces $\langle \eta^2 \rangle \approx 1$.

To determine how $\langle \eta^2 \rangle$ depends on ϕ, an estimate is needed for the phase fluctuations developed by the nth propagating mode traveling in the ϕ direction. Here, the approach of Clay (1964) is adopted; a ray with bottom grazing angle θ_n is associated with each of the N_p propagating modes of the sound channel and a simple statistical model is built from the I_n interactions of each ray with the rough ocean bottom. A more sophisticated approach based on the work of Kuperman (1975), and Kuperman and Ingentio (1977) may be possible but was not found necessary.

At the nth ray's i^{th} bottom interaction, the ray's phase will be modified by a random increment γ that depends on the acoustic wavenumber k, the local bottom roughness profile $H(r,\phi)$, and the ray's grazing angle θ_n, i.e. $\gamma = \gamma[k, H(r_{i,n},\phi), \theta_n]$. For i^{th} bottom interaction, the difference in the phase increment between the nth ray at ϕ and the nth ray at $\phi = 0$ will be:

$$\Delta\gamma_{i,n} = \gamma[k,H(r_{i,n},\phi),\theta_n] - \gamma[k,H(r_{i,n},0),\theta_n] \approx r_{i,n}\phi\frac{\partial\gamma}{\partial H}\frac{\partial H}{\partial y} \tag{10}$$

where $r_{i,n}$ is the distance from the array to n^{th} ray's i^{th} bottom interaction, the approximate equality follows from a Taylor series expansion of $\gamma[k, H(r_i,\phi), \theta_n]$ with $\phi \ll 1$, and the y-axis is horizontal and transverse to the $\phi = 0$ direction (see Fig. 1). The total phase difference, η, can be estimated

by summing (10) over bottom interactions and rays. Thus, if all the bottom interactions produce independent phase fluctuations, the variance of η is approximately:

$$\langle \eta^2 \rangle \approx N_p N_b \left\langle \left(r_{i,n} \phi \frac{\partial \gamma}{\partial H} \frac{\partial H}{\partial y} \right)^2 \right\rangle \tag{11}$$

where N_b is the average number of bottom interactions per ray and N_p is the number of rays.

To determine how $\langle \eta^2 \rangle$ depends on acoustic and sound channel parameters, proportionalities and scaling relationships can be inserted in (11). Here, $N_p \propto kD$, $N_b \propto R/D$, $r_{i,n} \sim R$, $\partial \gamma / \partial H \sim \gamma_{RMS} / H_{RMS}$, and $\partial H / \partial y \sim H_{RMS} / \Lambda$ are used to find

$$\langle \eta^2 \rangle \propto kD \frac{R}{D} R^2 \phi^2 \left(\frac{\gamma_{RMS}}{H_{RMS}} \right)^2 \left(\frac{H_{RMS}}{\Lambda} \right)^2 \propto \frac{kR^3 \gamma_{RMS}^2}{\Lambda^2} \phi^2 . \tag{12}$$

When $\langle \eta^2 \rangle$ is set equal to unity, (12) can be inverted to find the parametric dependence of ϕ_{FWHM}:

$$\phi_{FWHM} \propto \frac{\Lambda}{k^{1/2} R^{3/2} \gamma_{RMS}} . \tag{13}$$

In general, γ_{RMS} will be proportional to kH_{RMS} (see Ishimaru 1978) and a function g that depends on the statistics of the scattering geometry: $\gamma_{RMS} = kH_{RMS}g\left(H_{RMS}/\Lambda, \overline{\theta}\right)$ where H_{RMS}/Λ represents the surface slope, and $\overline{\theta}$ is an appropriate average modal-propagation grazing angle. Making this substitution for γ_{RMS} produces the final scaling law for ϕ_{FWHM}:

$$\phi_{FWHM} \propto \frac{\Lambda}{(kR)^{3/2} H_{RMS}g\left(H_{RMS}/\Lambda, \overline{\theta}\right)} . \tag{14}$$

This scaling law matches the kR power-law dependence shown on Fig. 8(a) and predicts ϕ_{FWHM} to be independent of D.

The accuracy of (14) and the remaining dependence of ϕ_{FWHM} on H_{RMS}/Λ was determined by plotting calculated results for ϕ_{FWHM} vs. the right side of (14) assuming a power-law behavior for the scattering function g. First, new simulations were carried out in sound channels that were vertically stretched and compressed by factors of two and one half, respectively, ($D = 150$ m and

37.5 m). For these simulations, the vertical TRA remained water-column-spanning with constant 3 m spacing and the acoustic frequency was 500 Hz. The source depth and speed of sound gradients were scaled, but the bottom roughness height was not changed. Additional simulations were also completed with the bottom roughness profiles stretched and compressed in the horizontal plane by factors of two and one half respectively, ($\Lambda = 560$ m and 140 m) compared to the nominal case ($\Lambda = 280$). Here too the roughness height was unchanged.

Figure 11 presents all of the computed results on a single plot for the shallower (a) and deeper (b) source. Figure 11 is similar in format to Figs. 8-10 except that the inset triangle shows a slope of -1 and the horizontal axis is $(kRH/\Lambda)^{3/2}$. This scaling factor was found by trial and error to produce the best collapse of the computed results for the shallower source. It implies $g(H_{RMS}/\Lambda, \bar{\theta}) \sim \sqrt{H_{RMS}/\Lambda}$.

Given the sophistication of the arguments leading to (14), the collapse of results in Fig. 11(a) is good with the exception of the attenuation upturns at longer ranges and the shorter-range results at lowest roughness level. In fact, a quantitative power-law relationship for the azimuthal retrofocus size of the shallower source can be proposed:

$$\phi_{FWHM}(degrees) \approx 2500 \left(\frac{\Lambda}{kRH_{RMS}} \right)^{3/2}, \tag{15}$$

where the empirical constant (2500) was chosen by eye to fit the bulk of the calculations for ϕ_{FWHM} that are not influenced by absorption. This scaling law accounts for ϕ_{FWHM} in terms of five length scales ($1/k$, D, R, H_{RMS}, and Λ) and should be applicable to a wide variety of shallow water sound channels when absorption effects are minimal.

The collapse of the ϕ_{FWHM} results for the deeper source ($z_s = 50$ m) shown on Fig. 11(b) are favorable but not as compelling as for the shallow source. Here the retrofocus is mostly formed by the lowest order modes that are least likely to be perturbed by bottom interactions and the azimuthal retrofocus sizes are larger than that found for the shallower source ($z_s = 25$ m). The influence of the mode-averaged grazing angle on ϕ_{FWHM}, which is not predicted in (14), is the most likely cause for the less successful collapse of results shown on Fig. 11(b). However, (15) does provide a consistent lower limit for ϕ_{FWHM} for the deeper source.

In summary, bottom roughness encourages environment-enhanced retrofocusing. Higher acoustic frequencies, greater bottom roughness, and longer ranges sharpen azimuthal retrofocusing except when absorption of the high-order propagating modes reverses these trends.

C. Azimuthal Retrofocusing with Static Internal Waves

Variations in the water column properties caused by internal waves may also lead to environment-enhanced retrofocusing. In a sound channel with vertical variation in the sound speed, internal waves raise and lower the contours of constant sound speed to produce a fully three-dimensional (3D) sound-speed field. This subsection describes the effects of a random superposition of linear internal waves on vertical TRA azimuthal retrofocusing in the baseline sound channel without bottom roughness. The parameters varied here include the source depth (z_s), the source-array range (R), and the acoustic frequency (f). These internal-wave retrofocusing results are provided for comparison with the bottom roughness results presented in the previous subsections, and for comparison with the simplified theory in Kholsa & Dowling (1998).

Figure 12 shows the azimuthal retrofocus width, ϕ_{FWHM}, versus scaled source-array range, kR, for source depths of $z_s = 25$ m [Fig. 12(a)] and $z_s = 50$ m [Fig. 12(b)]. The logarithmic range on both axes and the scaling of this figure allow it to be directly compared to Figs. 8, 9, and 10. The shallow source data plainly show that as the range increases, ϕ_{FWHM} decreases for a random linear super-position of internal waves whose strength is matched to measurements made during the SWARM experiment. This trend is not as strong and then appears to slightly reverse at long ranges for the deep source. Comparison of Figs. 10 and 12 shows that an RMS depth fluctuation of 1.5 m leads to nearly the same azimuthal retrofocus extent as the SWARM-strength internal waves for both the shallow and deep sources.

These internal-wave retrofocusing results can also be compared to the simple single-path straight-ray theory developed in Khosla and Dowling (1998). Their equation (5a) predicts that horizontal retrofocusing will be produced by a linear vertical TRA operating in a randomly refracting free-space environment. For small retrofocus angles, their prediction for ϕ_{FWHM} (in radians) becomes:

$$\phi_{FWHM}(radians) \approx \frac{2.35 w_y}{R} = 8.14 \left(\frac{k}{-A_{yy}} \right)^{1/2} (kR)^{-3/2} \tag{16}$$

16

where w_y is the horizontal standard-deviation width of the retrofocus, and A_{yy} is the second spatial derivative of the projected autocorrelation function of index of refraction fluctuations with respect to the horizontal coordinate (see Ishimaru 1978, A_{yy} is negative). Figure 13 shows a comparison of (16) (solid straight line) with the current computed results (curves with symbols) for the shallow source ($z_s = 25$ m). The value of A_{yy} used to construct this figure (-1.4×10^{-8} m^{-1}) was obtained from a water-column average of the simulated internal wave fluctuations. The scaling suggested by (11) produces a remarkable collapse of the computational results for ϕ_{FWHM} at the various acoustic frequencies and source-array ranges even though the predicted power law exponent and retrofocus sizes do not perfectly match the computational results. The simulation results for ϕ_{FWHM} are approximately a factor of two larger than the predictions of (16).

Like the bottom roughness cases, the scaled internal-wave-field results for ϕ_{FWHM} with the deeper ($z_s = 50$ m) source shown on Fig. 13(b) do not collapse as well as the scaled shallower ($z_s = 25$ m) source results. Here, the low-order modes forming the deeper retrofocus predominantly pass underneath the sound speed variations shown in Fig. 2(b). Thus, the scaling law (16), which is based on a water-column average of sound-speed fluctuations, over predicts the azimuthal scattering effects of the internal waves when the source is deep in the sound channel. However, when taken together, the deep and shallow source results suggest that random refraction has similar effects on azimuthal TRA retrofocusing in both free-space (single-path) and sound channel (multi-path) environments when the propagating sound fields interact with the random media.

III. Summary and Conclusions

This paper reports the findings of a computational study of the azimuthal (or horizontal) extent of the retrofocus formed by a vertical narrowband water-column-spanning time-reversing array operating in a static random shallow ocean. The influences of source depth, source-array range, acoustic frequency, bottom absorption, random bottom roughness, and internal-wave-induced fluctuations have all been addressed. Moreover, two power law scalings for the azimuthal size of the TRA retrofocus have been found.

The results presented here lead to several conclusions. First of all, random depth variations in a sound channel environment sharpen the retrofocusing in the azimuthal direction while leaving the vertical retrofocus size essentially unchanged. This occurs because modal propagation dominates the vertical character of shallow-water sound fields so that the more delicate effects of weak horizontal environmental variations can only be ascertained in the azimuthal (or horizontal)

17

retrofocus size. Second, the environment's ability to enhance (i.e. decrease) a vertical TRA's azimuthal retrofocus size increases with increasing acoustic frequency, environmental fluctuation levels, and source-array range. While this conclusion is strongly supported by the rough bottom results shown in Figs. 8-11, it also applies to retrofocusing with random internal waves. Third, the extent to which vertical-TRA azimuthal retrofocusing is influenced by random environmental fluctuations in a shallow ocean sound channel is determined by the depth of the source and the character of the channel's propagating modes. Deep (shallow) source retrofocusing relies more heavily on the lower (higher) order propagating modes that are less (more) susceptible to scattering from bottom roughness and internal waves. Thus, deep (shallow) sources produce larger (smaller) azimuthal retrofocus sizes. And, the shallow-source azimuthal sizes are amenable by simple power law scalings which form lower bounds for deeper source retrofocus sizes. Fourth, bottom absorption eventually reverses the trend toward better azimuthal retrofocusing with increasing bottom roughness and range.

And finally, the good (perhaps even fortuitous) agreement found between the simple theory of (16) and the calculated azimuthal retrofocus sizes for the shallower source suggests that retrofocusing through random media in single-path and multipath environments shares some common features. In this circumstance, the connection between single-path and multipath environments may lie in the fact that the calculated sound channel results only incorporate vertical multipath propagation. When viewed in the usual vertical r-z plane, multipath propagation is apparent in the sound channels of this study. However, when sound propagation in the same environments is viewed from above (i.e. looking down on the r-ϕ plane) there is only one propagation path; all of the various bottom and surface bounce paths seen in the r-z plane follow the same r-ϕ path. Moreover, this lone path is a straight line in the horizontal r-ϕ plane. Weak horizontal propagation variations lead to azimuthal retrofocusing, and (16) is based on there being a single straight average propagation path through the random medium between any two points. Interestingly, both of these phenomena (weak horizontal propagation variations, and straight r-ϕ plane rays) are captured in the current N×2D calculations. Thus, the main reason that (16) was found successful in the internal-wave perturbed sound channels simulated here is because the dominant multipath propagation occurs in vertical planes while the phenomena necessary for vertical-array azimuthal retrofocusing are reasonably well simulated by single-path propagation in the horizontal r-ϕ plane. Therefore, although (16) is surprisingly effective, it will likely fail in

more complicated three-dimensional environments that support both horizontal (i.e. azimuthal) and vertical multipath propagation.

Acknowledgements

References

Apel, J.R., Badiey, M., Chiu, C.-S., Finette, S., Headrick, R., Kemp, J., Lynch, J.F., Newhall, A., Orr, M.H., Pasewark, B.H., Tielbürger, D., Turgut, A., von der Heydt, K., and Wolf, S. (1997). "An overview of the 1995 SWARM Shallow-water internal wave acoustic scattering experiment," IEEE J. Oceanic Eng. 22, 465-500.

Bell, T.H. (1975). "Statistical features of sea floor topography," Deep Sea Res., 22, 883-892.

Berkson, J.M. and Matthews, J.E. (1984). "Statistical Characterization of Seafloor Roughness," IEEE J. Oceanic Eng. 9, 48-52.

Buckingham, M.J. (1984). "Acoustic propagation in a wedge-shaped ocean with perfectly reflecting boundaries," in *Hybrid Formulation of Wave Propagation*, edited by L.B. Felsen, Nijhoff, Dordrecht.

Chakroun, N., Fink, M., and Wu, F. (1995). "Time reversal processing in ultrasonic nondestructive testing," IEEE Trans. Ultrason. Ferroelectr. Freq. Control 42, 1087-1098.

Clay, C.S. (1964). "Effect of a slightly irregular boundary on the coherence of waveguide propagation," J. Acoust. Soc. Am. 36, 833-837.

Collins, M.D. (1993). "A split-step Padé solution for parabolic equation method," J. Acoust. Soc. Am. 93, 1736-1742.

Collins, M.D. (1994). "Generalization of the split-step Padé solution," J. Acoust. Soc. Am. 96, 382-385.

Collins, M.D. (1998). "New and improved parabolic equation models," J. Acoust. Soc. Am. 104, No. 3, Pt. 2, 1808.

Dashen, R., Munk, W.H., Watson, K.M., and Zachariasen, F. (1979). In *Sound Transmission Through a Fluctuating Ocean*, edited by S.M. Flatté (Cambridge U.P., Cambridge).

Dowling, D.R., and Jackson, D.R. (1992). "Narrow-band performance of acoustic phase-conjugate arrays in dynamic random media," J. Acoust. Soc. Am. 91, 3257-3277.

Draeger, C., Cassereau, D., and Fink, M. (1998). "Theory of the time-reversal process in solids," J. Acoust. Soc. Am. 102, 1289-1295.

Draeger, C. and Fink, M. (1999a). "One channel time-reversal in chaotic cavities: Theoretical limits," J. Acoust. Soc. Am. 105, 611-617.

Draeger, C., Aime, J.-C., and Fink, M. (1999b). "One channel time-reversal in chaotic cavities: Experimental results," J. Acoust. Soc. Am. 105, 618-625.

Dungan, M.R., and Dowling, D.R. (2000). " Computed narrowband time-reversing array retrofocusing in a dynamic shallow ocean," J. Acoust. Soc. Am 107, 3101-3112.

Finette, S. (1998). Private Communication.

Fink, M. (1997). "Time-Reversed Acoustics," Physics Today 50, No. 3, 34-40.

Fink, M. (1999). "Time-Reversed Acoustics," Scientific American 281, No. 5, 91-97.

Fox, C.G. and Hayes, D.E., (1985), "Quantitative Methods for Analyzing the Roughness of the Seafloor, " Reviews of Geophysics 23(1), 1-48.

Hodgkiss, W.S., Song, H.C., Kuperman, W.A., Akal, T., Ferla, C., and Jackson,, D.R. (1999). "A long-range and variable focus phase-conjugation experiment in shallow water" J. Acoust. Soc. Am. 105, 1597-1604.

Ishimaru, A. (1978). *Wave Propagation and Scattering in Random Media* (Academic Press, San Diego), Vol. 2.

Jackson, D.R., Winebrenner, D.P., and Ishimaru, A. (1986). "Application of the composite roughness model to high-frequency bottom backscattering," J. Acoust. Soc. Am. 79, 1410-1422.

Jackson, D.R. and Dowling, D.R. (1991). "Phase-conjugation in underwater acoustics," J. Acoust. Soc. Am. 89, 171-181.

Jensen, F.B., Kuperman, W.A., Porter, M.B., and Schmidt, H. (1994). *Computational Ocean Acoustics*, AIP Press, New York, p. 41.

Khosla, S.R., and Dowling, D.R. (1998). "Time-reversing array retrofocusing in simple dynamic underwater environments," J. Acoust. Soc. Am. 104, 3339-3350.

Khosla, S.R., and Dowling, D.R. (2000). "Time-reversing array retrofocusing in noisy environments," revised for the J. Acoust. Soc. Am., August 2000.

Kuperman, W.A. (1975). "Coherent component of specular reflection and transmission at a randomly rough two-fluid interface," J. Acoust. Soc. Am. 58, 365-370.

Kuperman, W.A., Hodgkiss, W.S., Song, H.C., Akal, T., Ferla, C., and Jackson, D.R. (1998). "Phase-conjugation in the ocean: experimental demonstration of an acoustic time reversal mirror," J. Acoust. Soc. Am. 103, 25-40.

Kuperman, W.A., and Ingenito, F. (1977). "Attenuation of the coherent component of sound propagating in shallow water with rough boundaries," J. Acoust. Soc. Am. 61, 1178-1187.

Kuperman, W.A., Porter, M.B., Perkins, J.S., and Evans, R.B. **(1991)**. "Rapid computation of acoustic fields in three-dimensional ocean environments," J. Acoust. Soc. Am. **89**, 125-133.

Medwin, H. and Clay, C.S. **(1998)**. Fundamentals of Acoustical Oceanography, Wiley-Academic Press, Boston, Ch. 13.

Ohno, M., Yamamoto, K., Kokubo, A., Sakai, K., and Takagi, K. **(1999)** "Acoustic phase conjugation by nonlinear piezoelectricity. I. Principle and basic experiments," J. Acoust. Soc. Am. **106**, 1330-1338.

Orris, G.J. and Perkins, J.S. **(1998)**. "Three-dimensioanal propagation modeling in shallow water," 135th ASA Meeting Proceedings, Seattle, WA, 2429-2430.

Perkins, J.S. and Kuperman, W.A. **(1990)**. "Environmental signal processing: Three dimensional matched field processing with a vertical array," J. Acoust. Soc. Am. **87**, 1553-1556.

Press, W.H., Flannery, B.P., Teukolsky, S.A., and Vetterling, W.T. **(1986)** *Numerical Recipes* (Cambridge University Press, Cambridge) Chapter 16.

Rose, J.H., Bilgen, M., Roux, Ph., and Fink, M. **(1999)**. "Time-reversal mirrors and rough surfaces: Theory" J. Acoust. Soc. Am. **106**, 716-723.

Roux, Ph., De Rosny, J., Fink, M., and Rose, J.R. **(1999a)**. "Time-reversal mirrors and rough surfaces: Experiment" J. Acoust. Soc. Am. **106**, 724-732.

Roux, Ph., Derode, A., Peyre, A., Tourin, A., and Fink, M. **(1999b)**. "Acoustic imaging through a multiple scattering medium using a time-reversal mirror" J. Acoust. Soc. Am. **107**, L7-L12.

Smith, K.B. **(1996)**. "Modeling the effects of azimuthal coupling on acoustic propagation in the presence of 3-dimensional, rough ocean interfaces using the parabolic approximation," Special Issue of Theoretical and Computational Acoustics, eds. Lee et al., World Scientific Publishing Co., 115-131.

Smith, K.B. **(1998)**. "Three-dimensional propagation modeling in shallow water," 135th ASA Meeting Proceedings, Seattle, WA, 2087-2088.

Song, H.C., Kuperman, W.A., and Hodgkiss, W.S. **(1998a)**. "A time-reversal mirror with variable range focusing," J. Acoust. Soc. Am. **103**, 3234-3240.

Song, H.C., Kuperman, W.A., Hodgkiss, W.S., and Gerstoft, P. **(1998b)**. "Out-of-plane defocusing in a time reversal mirror," J. Acoust. Soc. Am. **104**, 1748 (A).

Song, H.C., Kuperman, W.A., Hodgkiss, W.S., Akal, T., and Ferla, C. **(1999)**. "Iterative time reversal in the ocean," J. Acoust. Soc. Am. **105**, 3176-3184.

Steinberg, B. D., **(1976)**, *Principles of Aperture and Array System Design*, Wiley, New York, Ch. 1,12.

Sturm, F.B., Fawcett, J.A., Jensen, F.B., Pélissier, M.-C. **(1998)**. "Benchmarking Two Three-Dimensional Parabolic Equation Methods," 135th ASA Meeting Proceedings, Seattle, WA, 2093-2094.

Tanter, M., Thomas, J.-L., and Fink, M., (1998). "Focusing and steering through absorbing and aberrating layers: Application to ultrasonic propagation through the skull," J. Acoust. Soc. Am. **103**, 2403-2410.

Tielbürger, D., Finette, S. and Wolf, S. (1997). "Acoustic propagation through an internal wave field in a shallow water waveguide," J. Acoust. Soc. Am. **101**, 789-808.

Yamamoto, K., Ohno, M., Kokubo, A., Sakai, K., and Takagi, K. (1999) "Acoustic phase conjugation by nonlinear piezoelectricity. II. Visualization and application to imaging systems," J. Acoust. Soc. Am. **106**, 1339-1345.

Yang, T.C. and Yoo, K. (1998). "Frequency spectrum of linear internal waves in shallow water and a modified Garrett-Munk model," J. Acoust. Soc. Am. **104**, No. 3, Pt. 2, 1765.

Yönak, S.H. and Dowling, D.R. (1999) "Photoacoustic detection and localization of small gas leaks," J. Acoust. Soc. Am. **105**, 2685-2694.

Yoo, K. and Yang, T.C. (1998). "Measurements of modal spectrum of linear internal waves in shallow water and comparison with the Garrett-Munk model," J. Acoust. Soc. Am. **104**, No. 3, Pt. 2, 1765.

Ziomek, L. J., (1985), *Underwater Acoustics*, Academic Press, Orlando, FL., Chaps. 3 and 4.

Table Caption

Table I. Bottom roughness effect on vertical full-width-at-half-maximum size of retrofocus, z_{FWHM}, at a source-array range of $R = 10$ km for various frequencies and two source depths $z_s = 25$ m (a) and $z_s = 50$ m (b). Notice that only small changes in mean vertical retrofocus sizes occur at each frequency, but large variations can occur in 50%-confidence levels for the vertical retrofocus sizes (in parentheses) as the RMS depth fluctuation increases.

Figure Captions

Figure 1. Schematic of the sound channel and time-reversing array (TRA) geometry. The radial coordinate is r. The vertical coordinate, z, increases downward. The azimuthal angle is denoted by ϕ. A harmonic omni-directional source is located at ($r=R$, $\phi=0$, $z=z_s$). The TRA receives the signal at ($r=0$, $\phi=0$, $z=z_n$) and retransmits it to form a retrofocus back near the source. The $z=0$ plane represents a pressure release surface. The ocean bottom has two layers.

Figure 2. Speed of sound versus depth for the baseline sound channel. (a) This profile is based on measurements made during the 1995 SWARM experiment that were provided to the authors by Dr. Steven Finette of the Naval Research Laboratory. (b) Average and fluctuating speed of sound in the synthetic internal wave field. The horizontal bars lie at ± 1 standard deviation.

Figure 3. Synthetic bottom variation spectrum for a power law of exponent $b = 2$. The inset triangle indicates slope of a curve with a power of two.

Figure 4. Sample synthetic bottom variation floor map over a 10 km by 20 km area for $H_{RMS} = 3.0$ m. The TRA is located on the left, with several azimuthal return paths superimposed. Several source locations are indicated by white dots. The gray-scale changes from black (more than +10 m upward deflection) to white (less than –10 m downward deflection).

Figure 5. Retrofocus field amplitude through the channel depth on a vertical screen as shown in Fig. 6 at a source-array range of $R = 10$ km for various bottom RMS height variations: $H_{RMS} = 0.0$ m (a), 0.75 m (b), 1.5 m (c), and 3.0 m (d). The acoustic frequency is $f = 500$ Hz and the source depth is $z_s = 25$ m. Each field is self normalized and black corresponds to the highest 10% of field amplitudes.

Figure 6. Sketch of a vertical screen illustrating the viewing orientation of the field plots on Figs. 5 and 7. The TRA is at the left with propagation paths compiled at small ϕ intervals to produce the field values displayed on the curved vertical screen (at $r = R$) shown at the right. The images on Figures 5 and 7 represent the field on the curved screen from the vantage point of the TRA ($r = 0$).

Figure 7. Retrofocus field amplitude through the channel depth on a vertical screen as shown in Fig. 6 for various source-array ranges: $R = 2.5$ km (a), 5 km (b), 10 km (c), and 20 km (d). The acoustic frequency is $f = 500$ Hz, the source depth is $z_s = 25$ m, and the RMS bottom roughness is $H_{RMS} = 3.0$ m. Each field is self normalized and black corresponds to the highest 10% of field amplitudes.

Figure 8. TRA retrofocus azimuthal full-width at half-maximum angles, ϕ_{FWHM}, versus acoustic-wavenumber-scaled source array-range (kR) for varying frequencies at source depths of $z_s = 25$ m (a) and 50 m (b). The RMS bottom roughness is $H_{RMS} = 3.0$ m. The inset triangle illustrates a -3/2 slope. The results suggest $\phi_{FWHM} \propto (kR)^{-3/2}$.

Figure 9. TRA retrofocus azimuthal full-width at half-maximum angles, ϕ_{FWHM}, versus acoustic-wavenumber-scaled source array-range (R) for varying bottom attenuation values at source depths of $z_s = 25$ m (a) and 50 m (b). The RMS bottom roughness is $H_{RMS} = 3.0$ m, and the acoustic frequency is $f = 500$ Hz.

Figure 10. TRA retrofocus azimuthal full-width at half-maximum angles, ϕ_{FWHM}, versus acoustic-wavenumber-scaled source array-range (R) for varying RMS bottom roughness at source depths of $z_s = 25$ m (a) and 50 m (b). The acoustic frequency is $f = 500$ Hz.

Figure 11. TRA retrofocus azimuthal full-width at half-maximum angles, ϕ_{FWHM}, versus the dimensionless parameter $\left(kRH_{RMS}/\Lambda\right)^{+3/2}$ for a variety of acoustic frequencies f, source-array ranges R, and root-mean-square bottom roughnesses heights H_{RMS} for bottom correlation lengths $\Lambda = 140$, 280, and 560 m and sound channel depths $D = 37.5$, 75, and 150 m with a source depth of $z_s = D/3$ (a) and $2D/3$ (b). Where not specified, the nominal parameters of $f = 500$ Hz, $H_{RMS} = 3.0$ m, $D = 75$ m, and $\Lambda = 280$ m were used in the simulations. The inset slope triangle shows a -1 slope. The collapse is better for the shallower source where ϕ_{FWHM} is typically smaller than for the deeper source.

Figure 12. TRA retrofocus azimuthal full-width at half-maximum angles, ϕ_{FWHM}, versus acoustic-wavenumber-scaled source array-range (R) for SWARM strength internal waves at various frequencies for source depths of $z_s = 25$ m (a) and 50 m (b) without bottom roughness.

Figure 13. Comparison of (16) to the computed retrofocus azimuthal full-width at half-maximum angles, ϕ_{FWHM}, versus acoustic-wavenumber-scaled source array-range (R) for SWARM strength internal waves at various frequencies for source depths of $z_s = 25$ m (a) and 50 m (b). The collapse is unsuccessful for the deeper source because the back-propagating field interacts little with the sound speed fluctuations.

Table Ia. Source Depth = 25 m

Frequency:	250 Hz	500 Hz	1000 Hz	2000 Hz
H_{RMS}(m)	z_{FWHM}/λ	z_{FWHM}/λ	z_{FWHM}/λ	z_{FWHM}/λ
0.0	2.8 (0.0)	2.7 (0.0)	2.7 (0.0)	2.4 (0.0)
1.0	2.9 (0.2)	2.7 (0.1)	2.7 (0.1)	2.6 (0.1)
2.0	3.1 (0.9)	2.6 (0.1)	2.6 (0.1)	2.7 (0.3)
3.0	3.3 (1.1)	2.6 (0.2)	2.7 (0.2)	2.6 (0.3)

Table Ib. Source Depth = 50 m

Frequency:	250 Hz	500 Hz	1000 Hz	2000 Hz
H_{RMS}(m)	z_{FWHM}/λ	z_{FWHM}/λ	z_{FWHM}/λ	z_{FWHM}/λ
0.0	3.7 (0.0)	4.0 (0.0)	4.8 (0.0)	3.4 (0.0)
1.0	3.7 (0.1)	4.0 (0.1)	4.1 (0.2)	4.5 (0.4)
2.0	3.8 (0.3)	4.1 (0.3)	3.9 (0.4)	4.0 (0.3)
3.0	3.9 (0.5)	4.1 (0.4)	3.6 (0.4)	3.2 (0.2)

Time Reversing Array
24 elements
spaced 3 m apart

Source Location
$(r=R, z=z_s, \phi=0)$

Mean Depth = 75 m

speed of sound=1650 m/s
top layer thickness=23 m

density=1700 kg/m³
attenuation=1.0 dB/λ

speed of sound=1950 m/s
bottom layer=half space

density=2200 kg/m³
attenuation=0.4 dB/λ

Fig. 2

a)

b)

Fig. 3

Fig. 4

Fig. 5

Fig. 6

Fig. 7
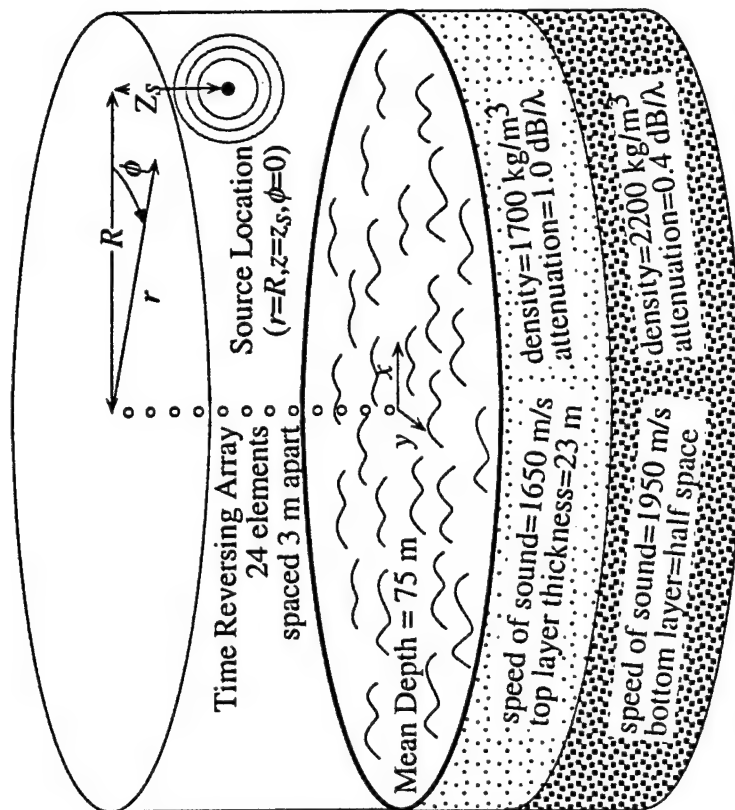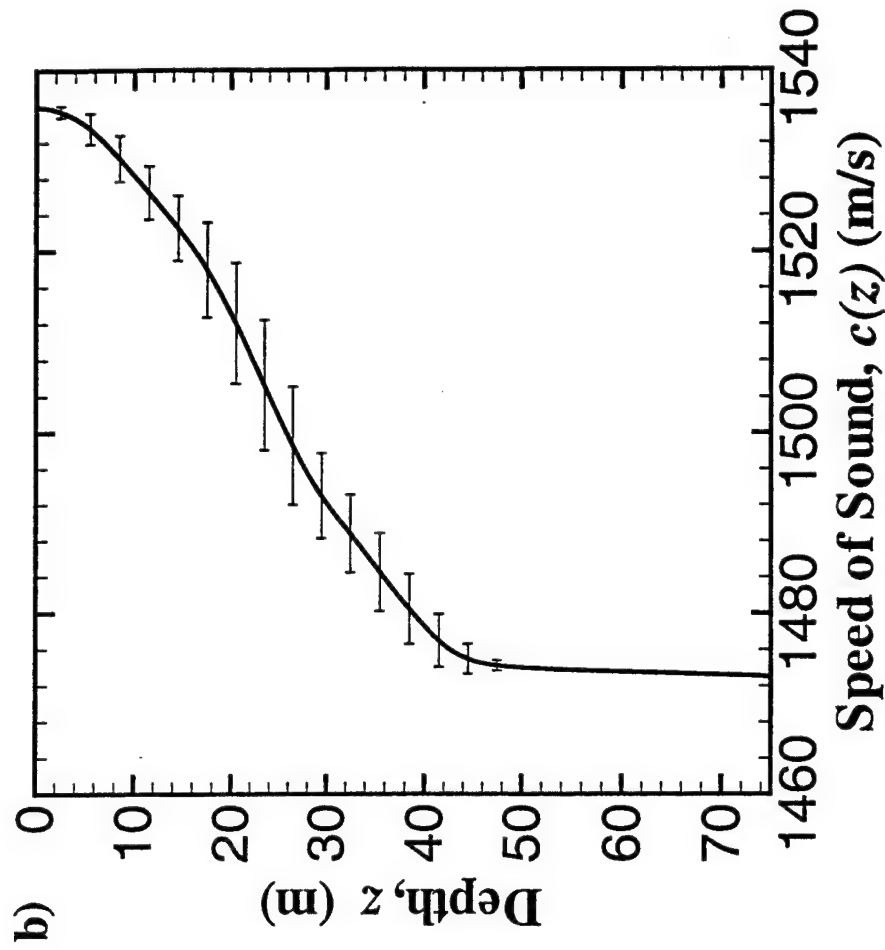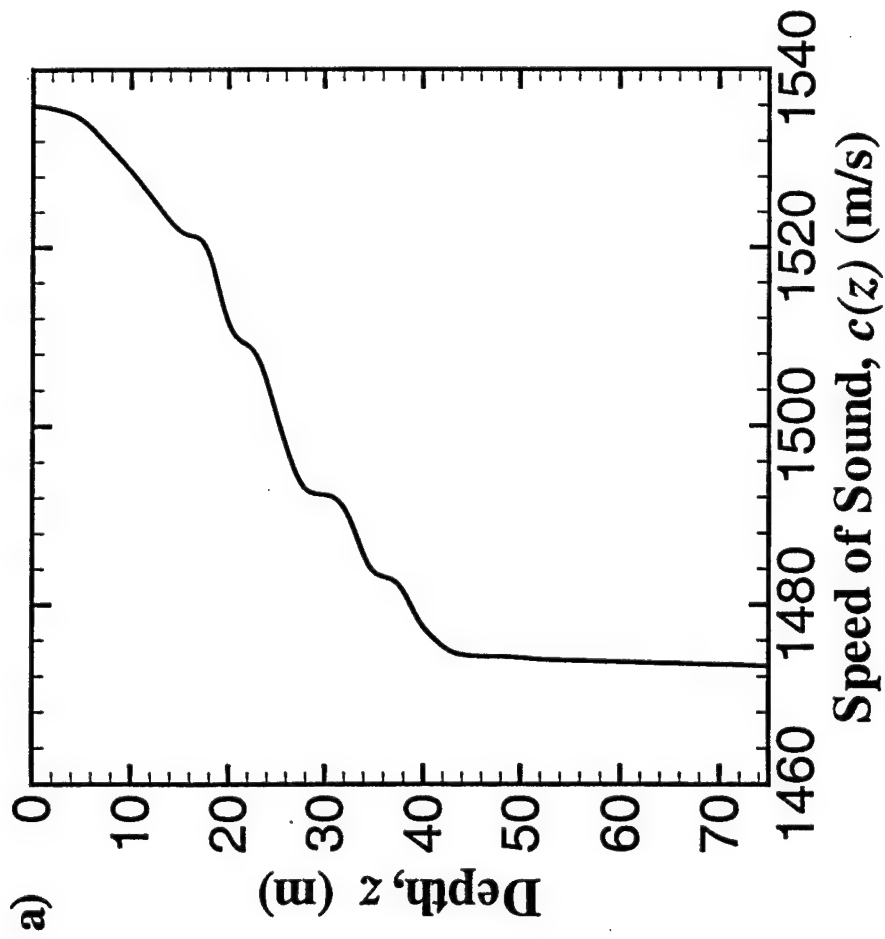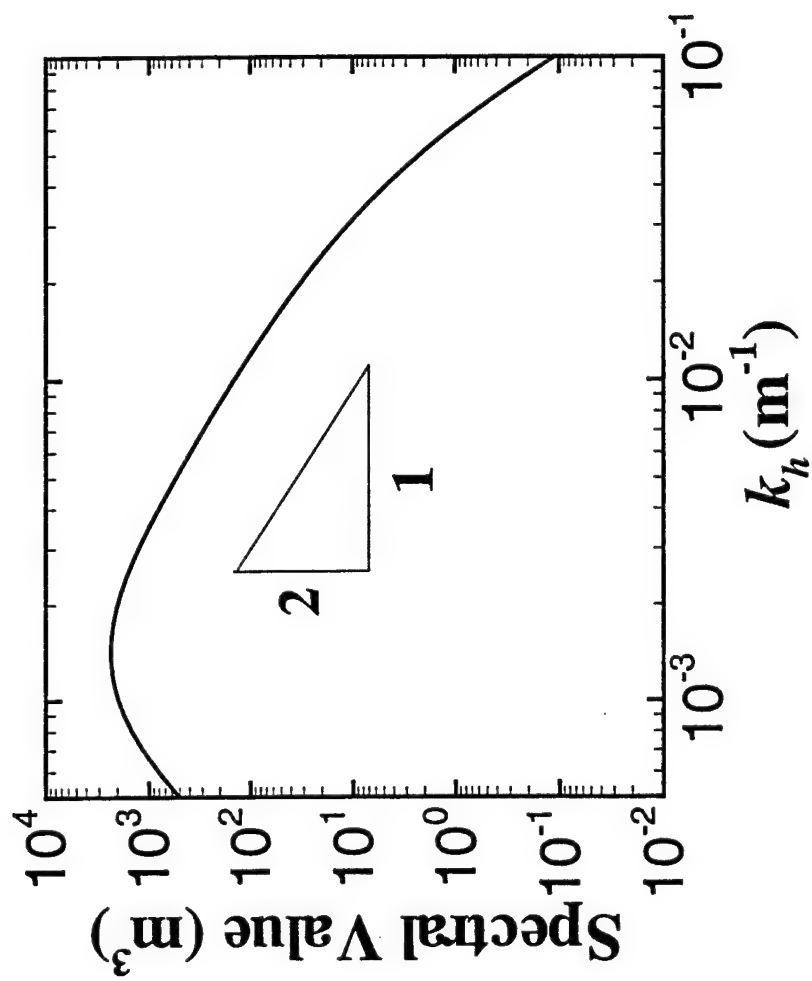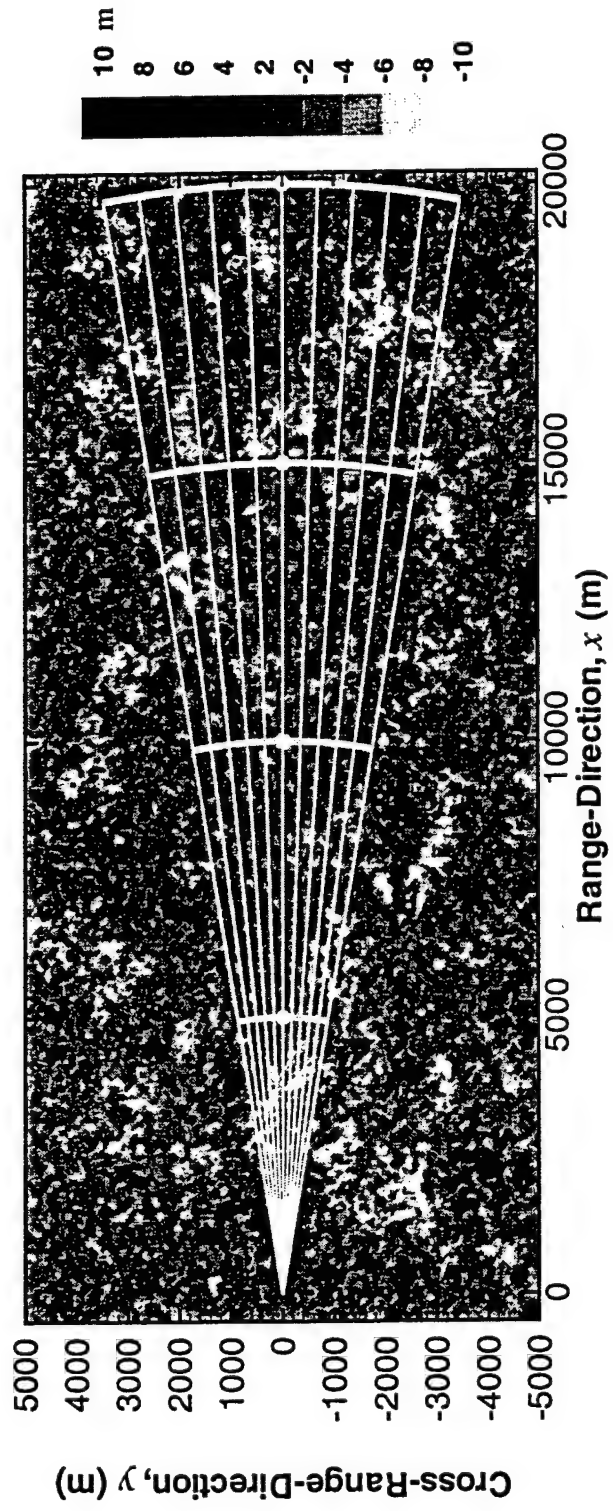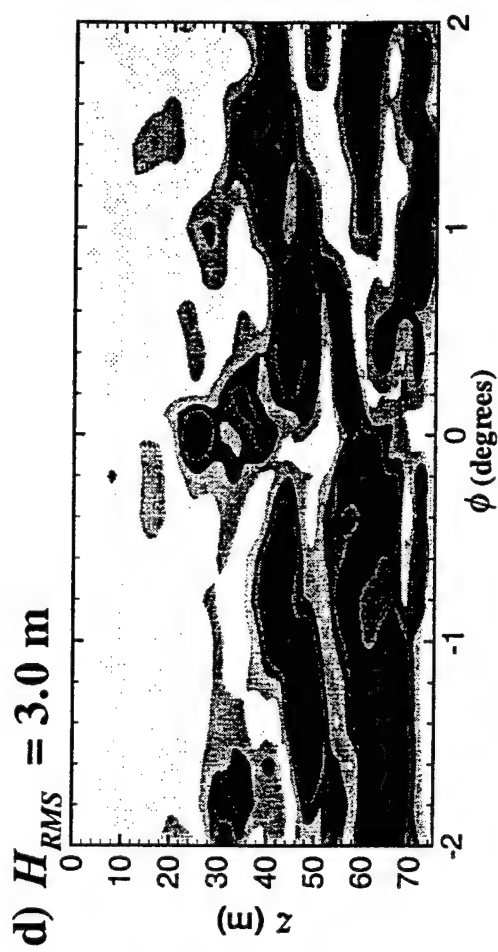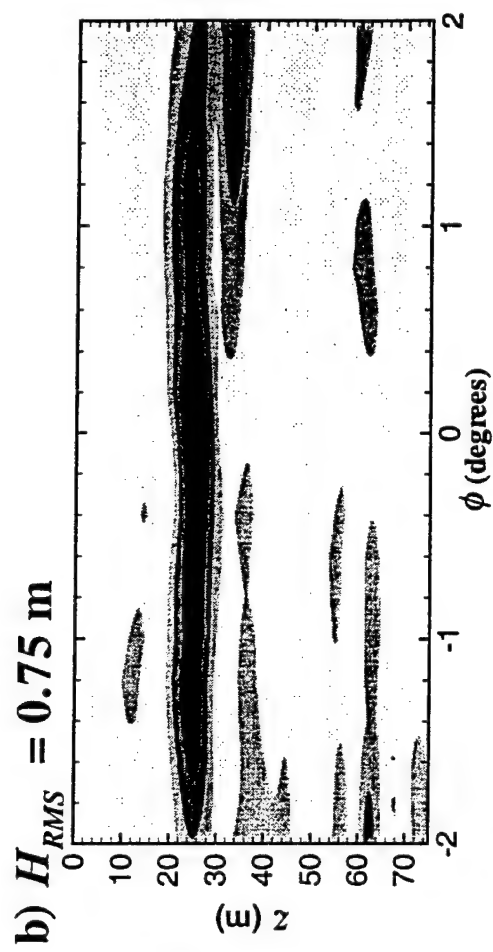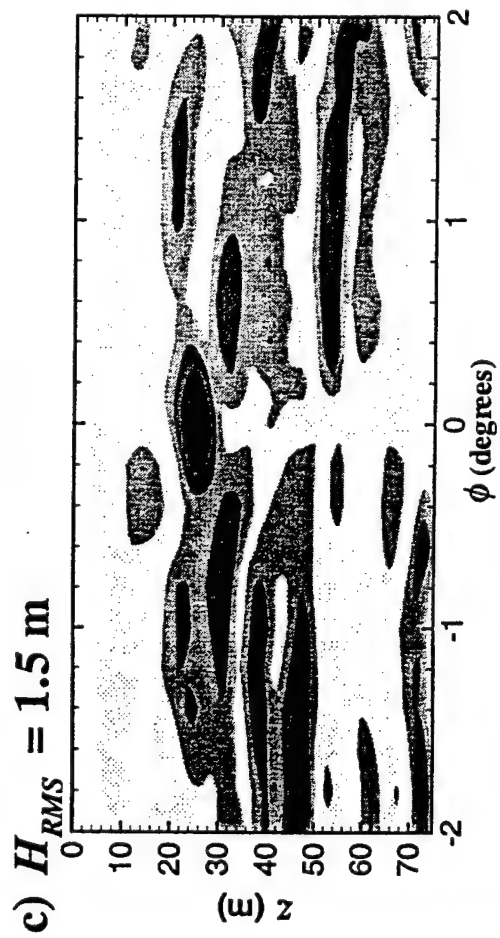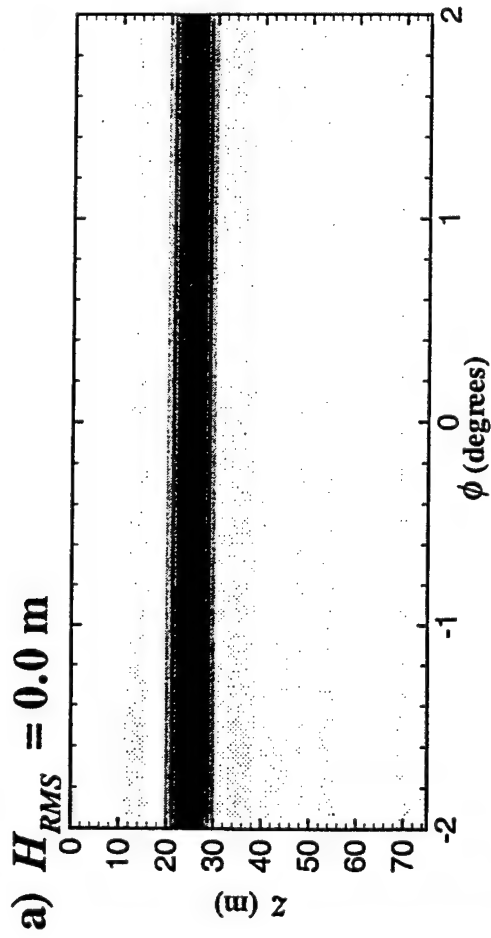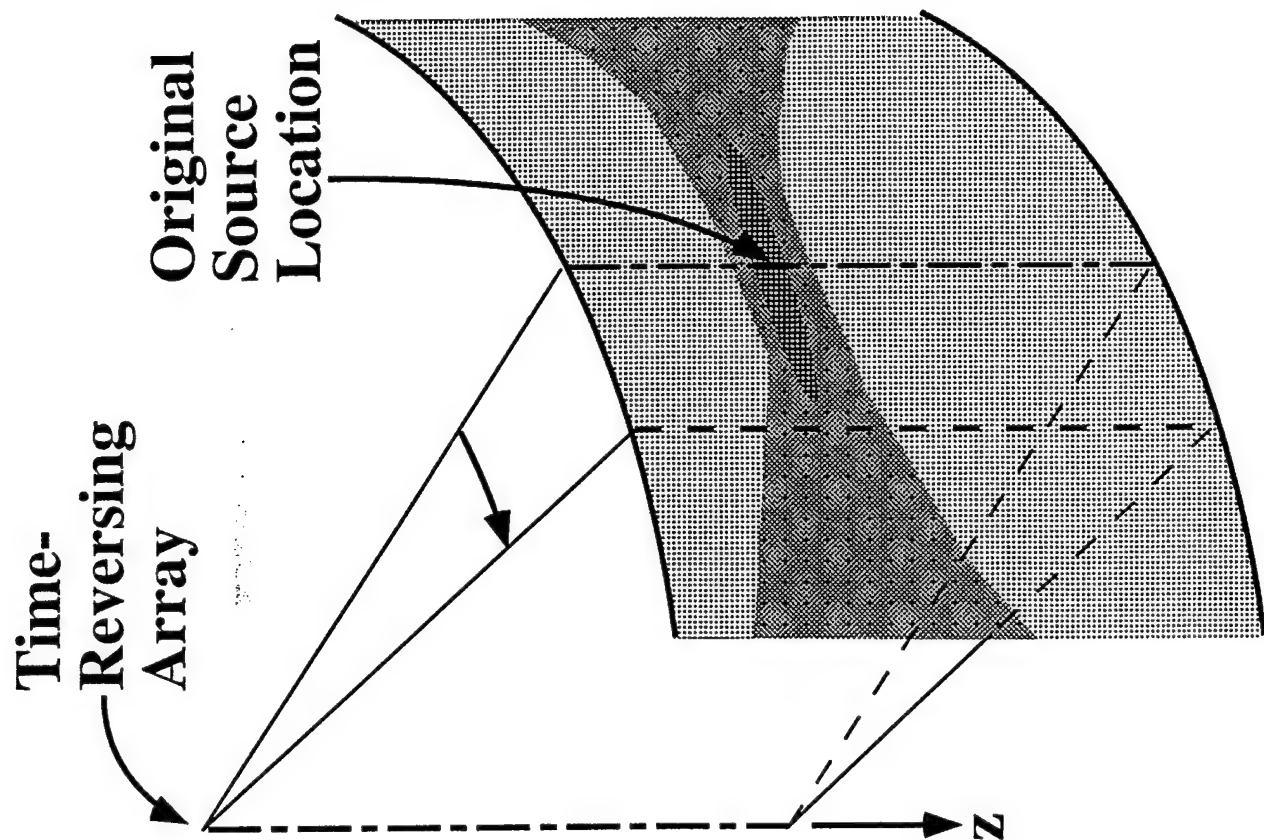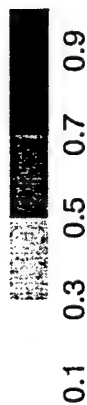
a) R = 2.5 km

b) R = 5 km

c) R = 10 km

d) R = 20 km
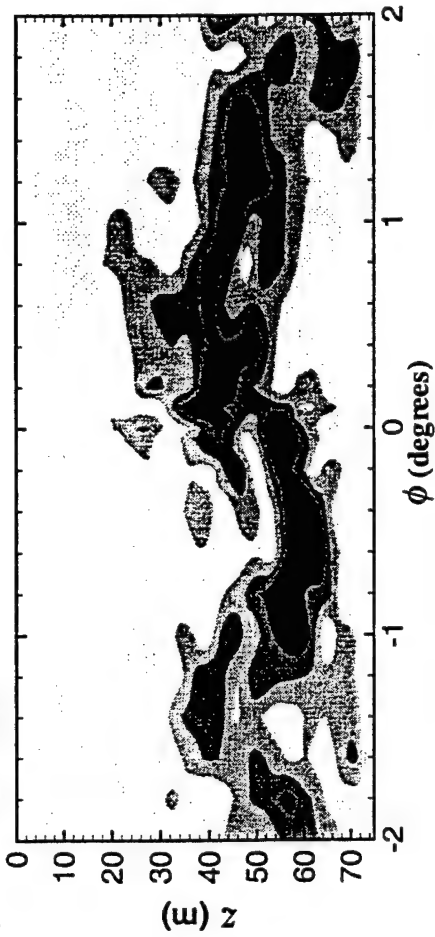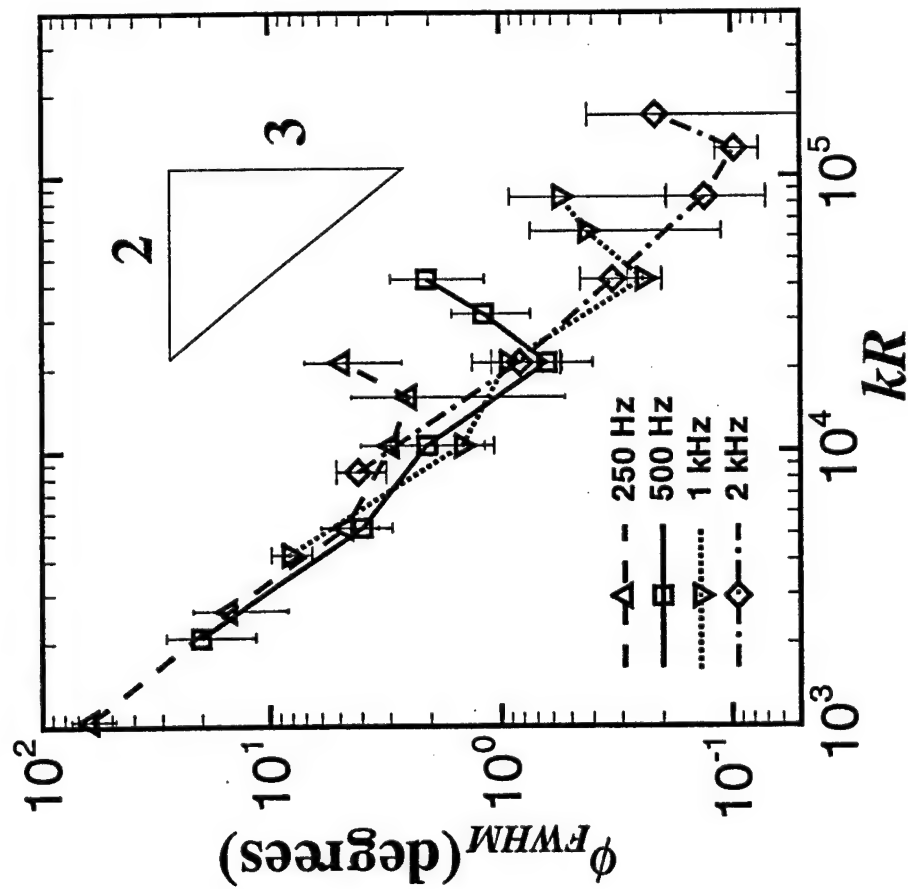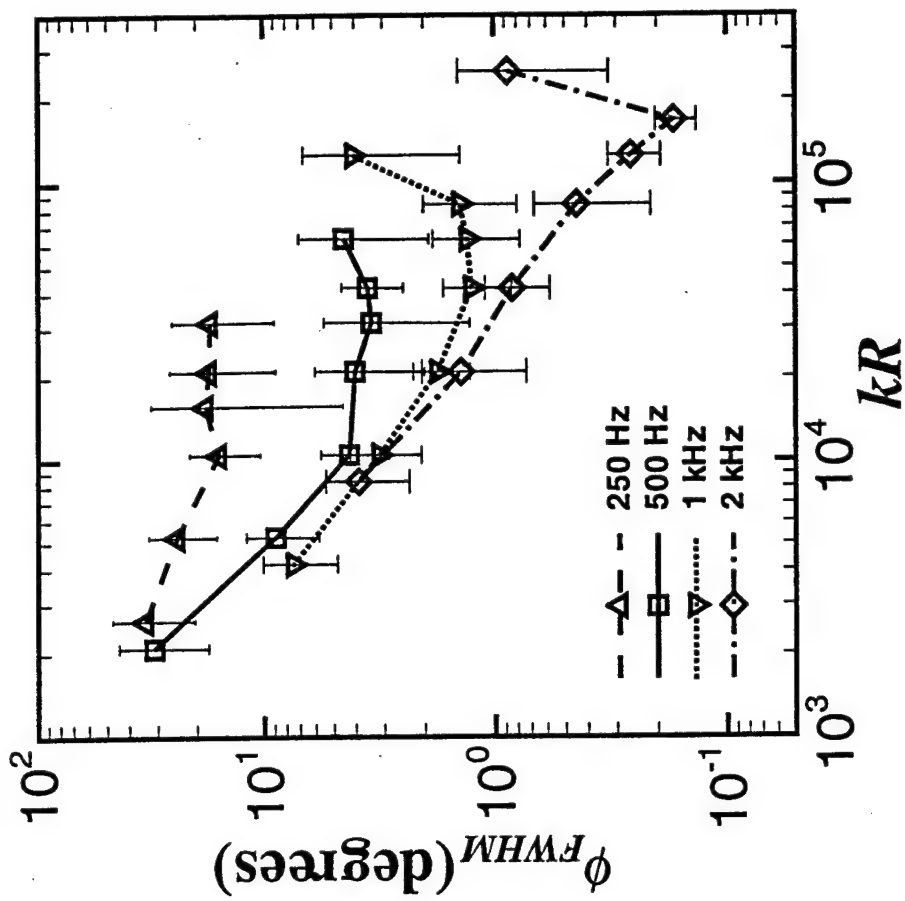
Fig 8

a) $z_s = 25$ m

ϕ_{FWHM}(degrees)

kR

250 Hz
500 Hz
1 kHz
2 kHz

b) $z_s = 50$ m

ϕ_{FWHM}(degrees)

kR

250 Hz
500 Hz
1 kHz
2 kHz

fig 9

a) $z_s = 25$ m

b) $z_s = 50$ m

Fig. 10

a) $z_s = 25$ m

b) $z_s = 50$ m

Fig.11

a) $z_s = D/3$

b) $z_s = 2D/3$

ϕ_{FWHM} (degrees)

$(kRH_{RMS}/\Lambda)^{3/2}$

Legend:
$f = 250\ Hz$
$f = 500\ Hz$
$f = 1\ kHz$
$f = 2\ kHz$
$D = 37.5\ m$
$D = 150\ m$
$H_{RMS} = 0.75\ m$
$H_{RMS} = 1.5\ m$
$\Lambda = 140\ m$
$\Lambda = 560\ m$

Fig. 12

a) $z_s = 25$ m

ϕ_{FWHM}(degrees)

kR

250 Hz
500 Hz
1 kHz
2 kHz

b) $z_s = 50$ m

ϕ_{FWHM}(degrees)

kR

250 Hz
500 Hz
1 kHz
2 kHz

Fig. 13

a) $z_s = 25$ m

b) $z_s = 50$ m

$(-A_{yy}/k)^{1/2} \phi_{FWHM}$

kR

250 Hz
500 Hz
1 kHz
2 kHz
Eq. (16)
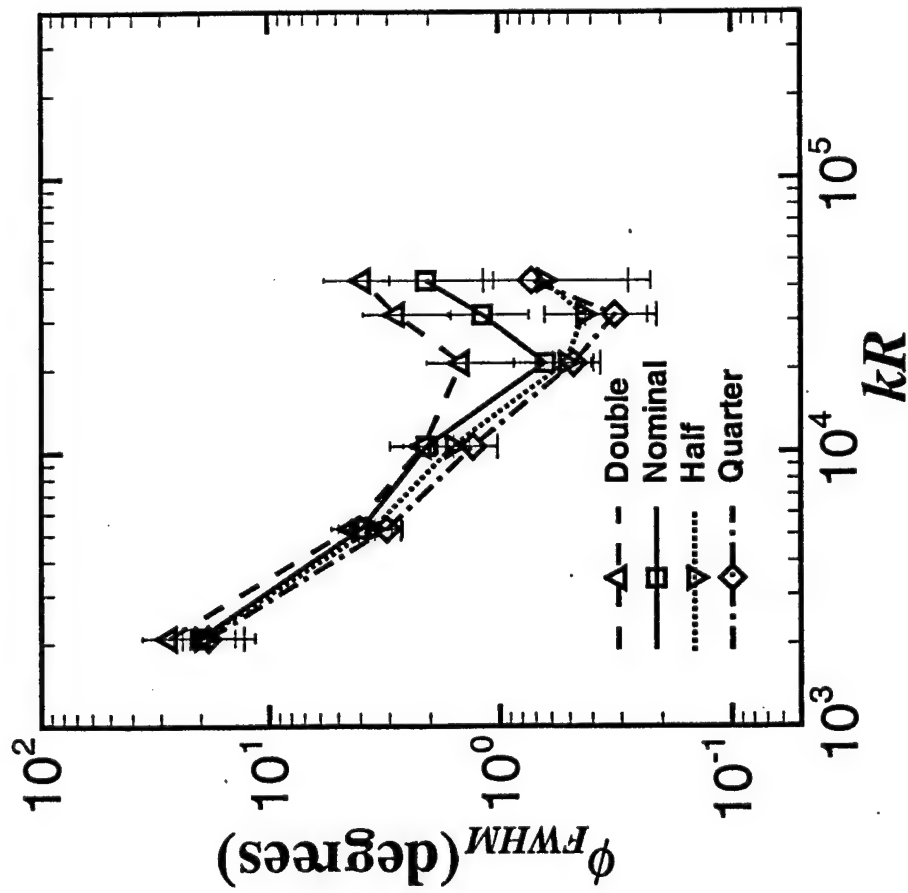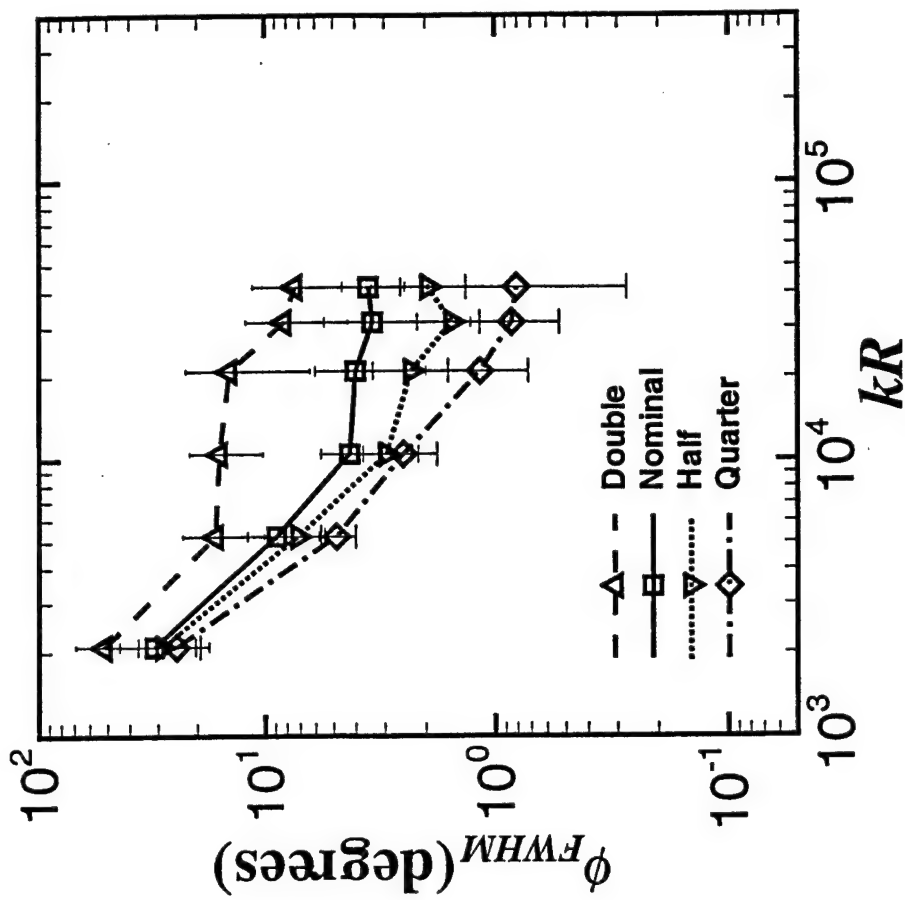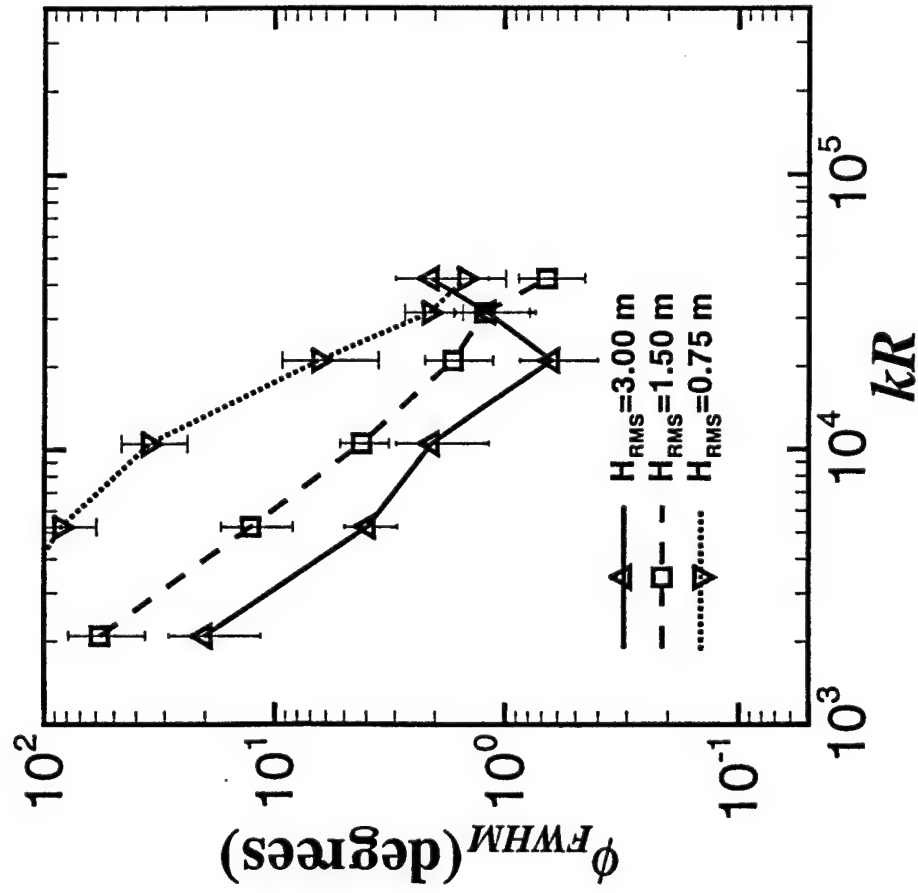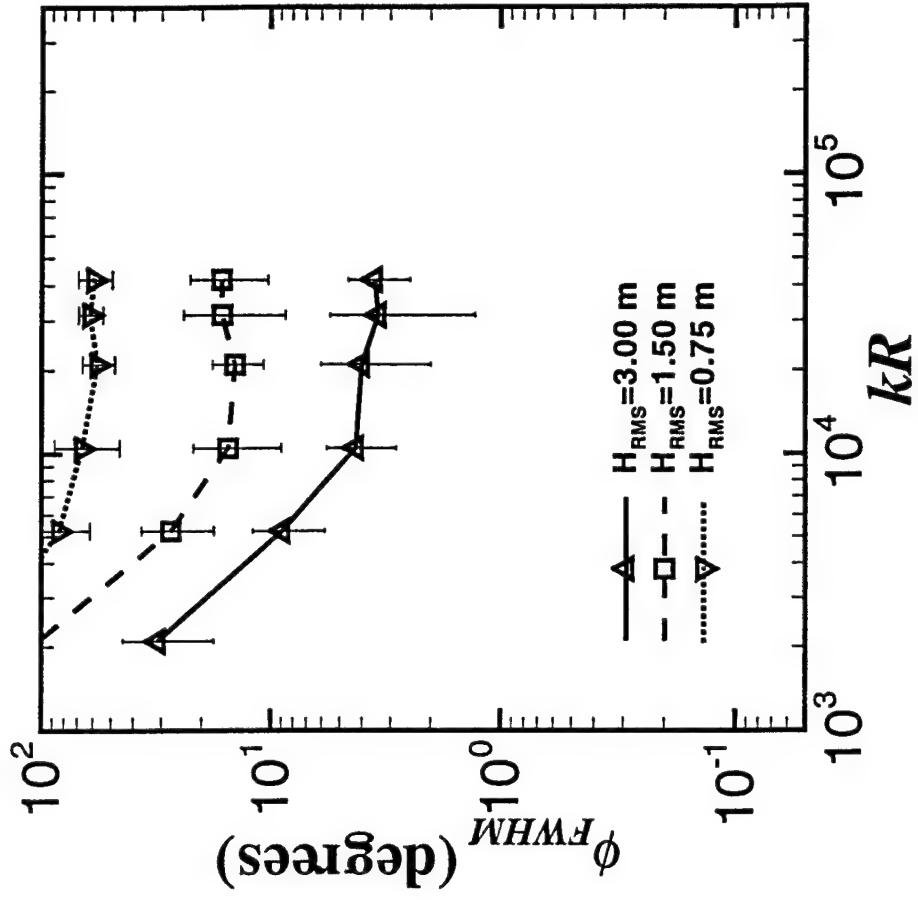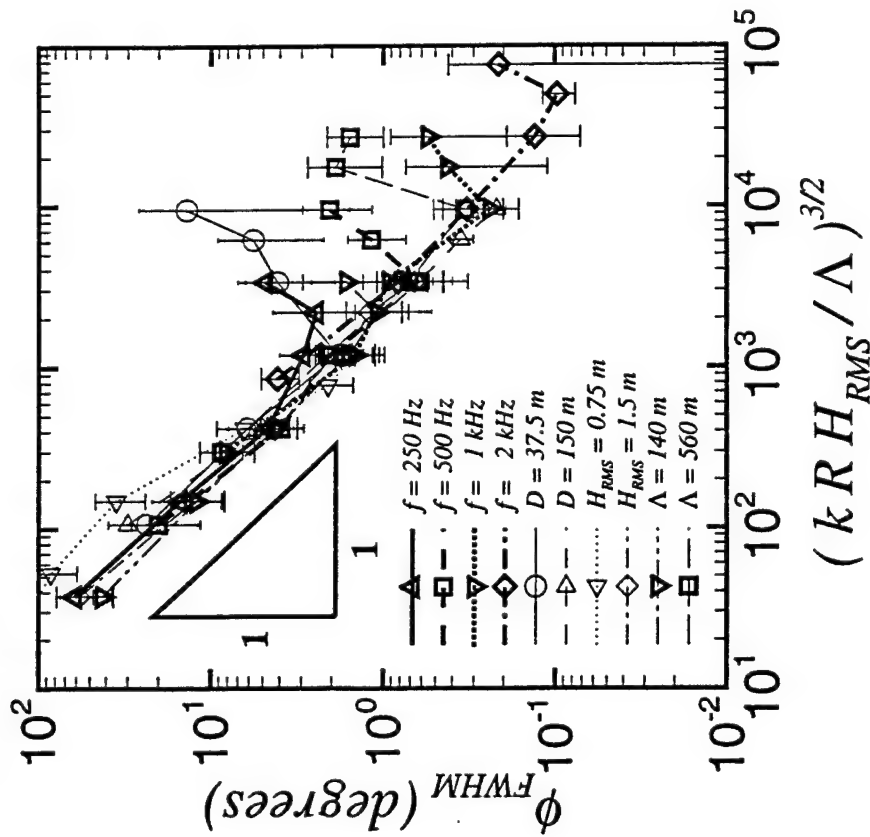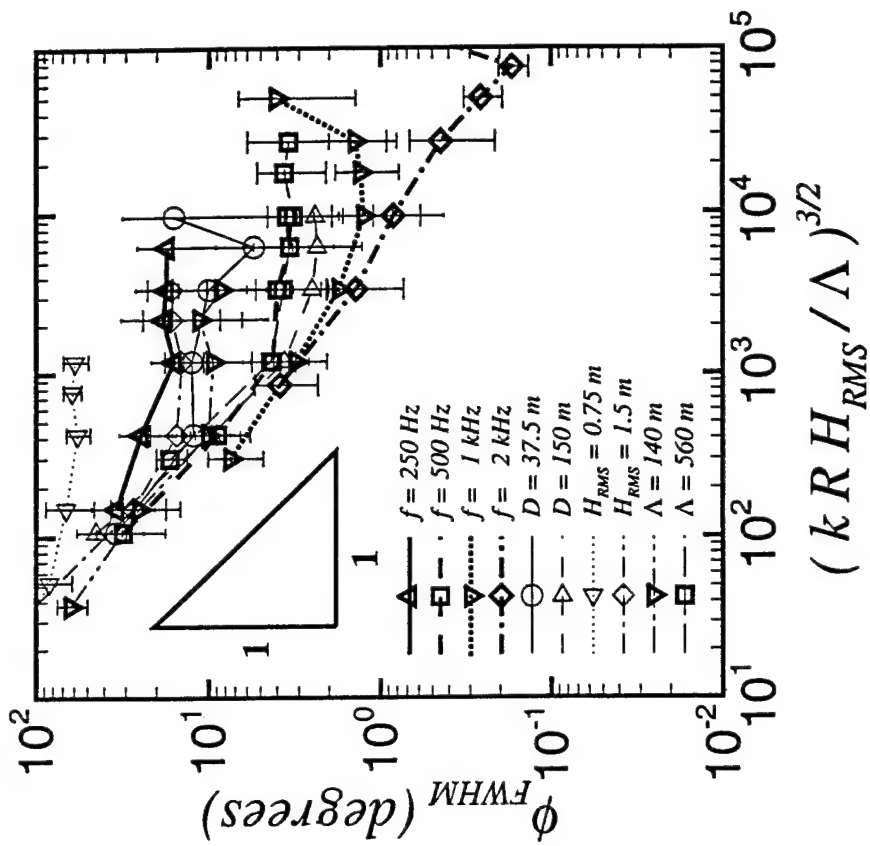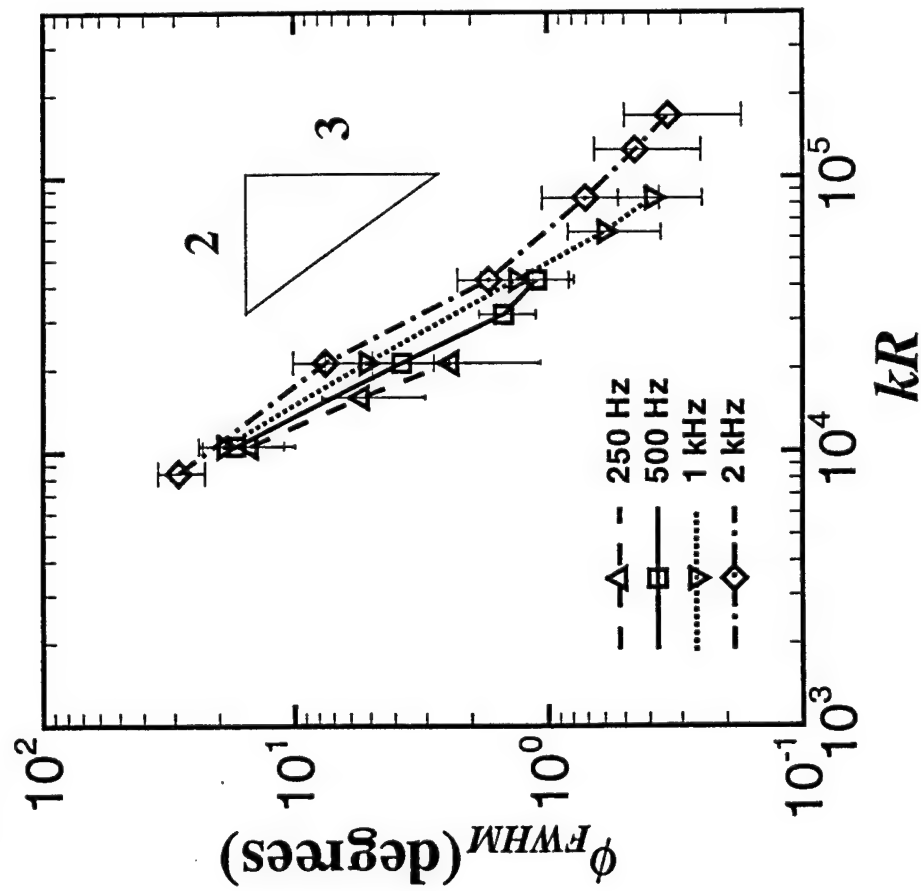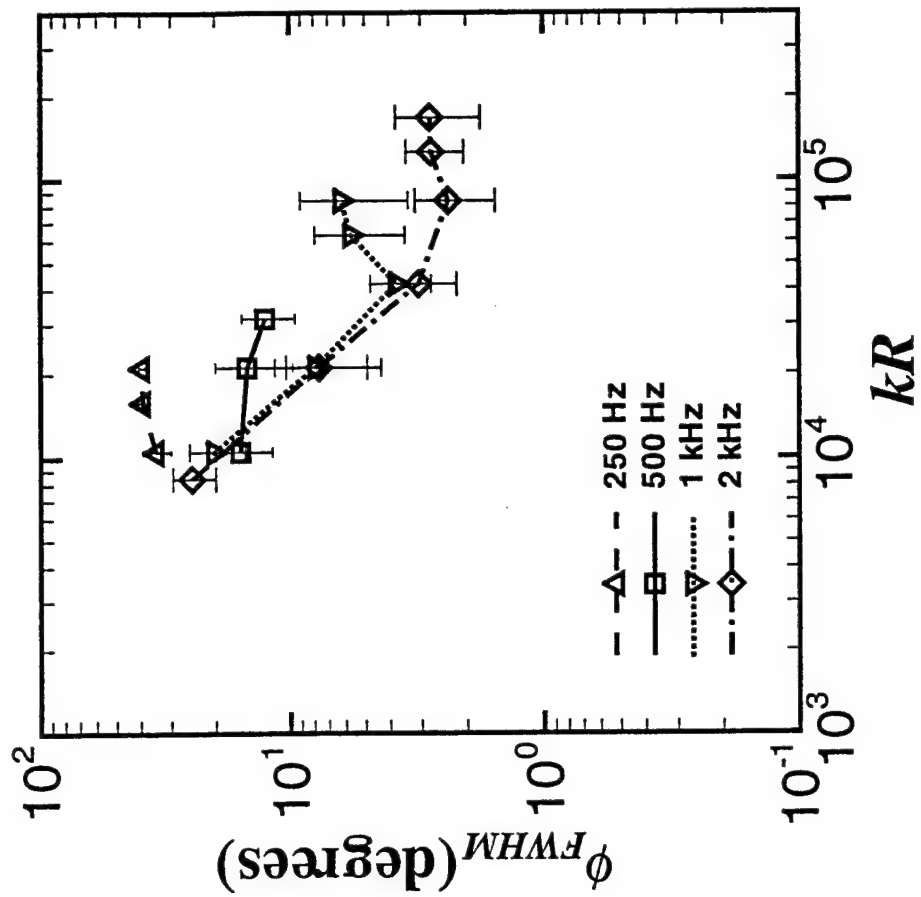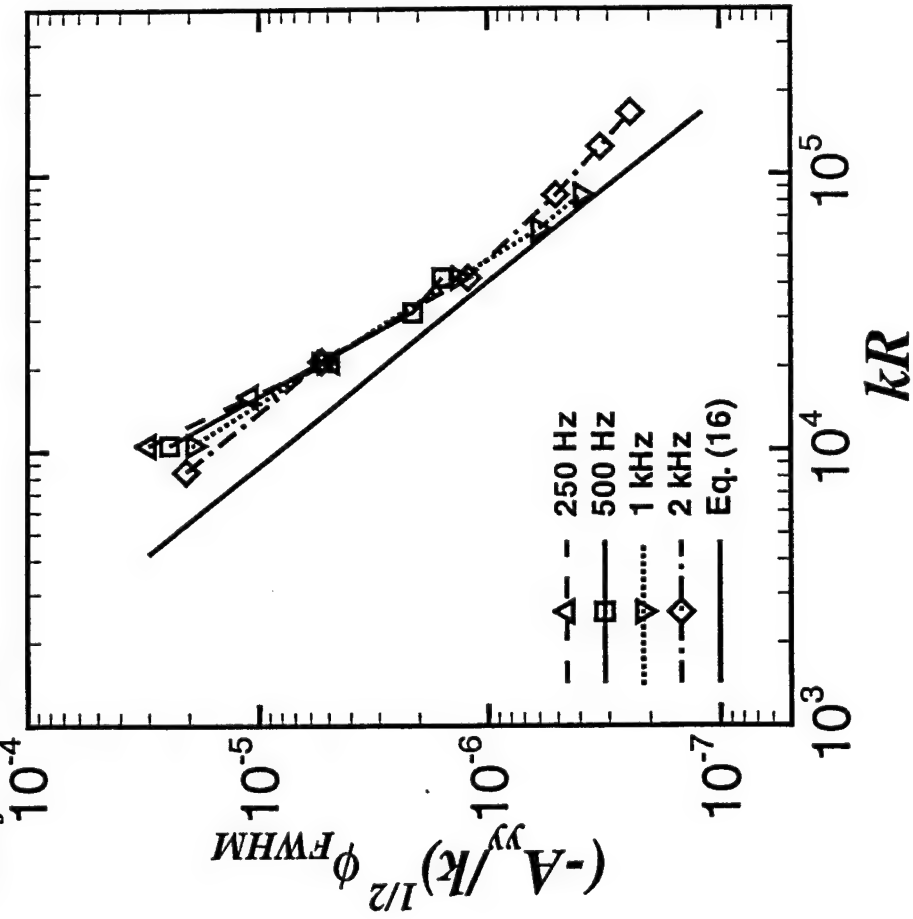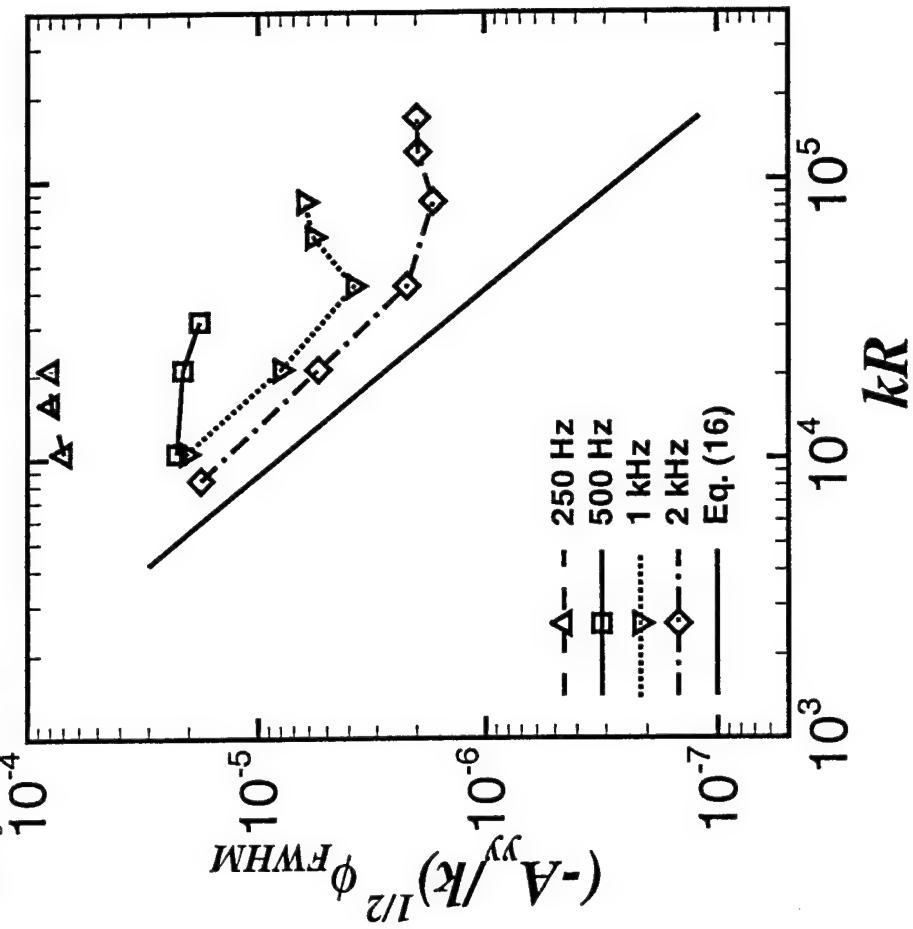
Orientation effects on linear time-reversing array retrofocusing in shallow water
(Submitted to *The Journal of the Acoustical Society of America*, 2/01)

Michael R. Dungan and David R. Dowling
Dept. of Mechanical Engineering, University of Michigan, Ann Arbor, MI 48109-2121

Abstract

A time-reversing array (TRA) can retrofocus acoustic energy, in both time and space, to the original sound-source location without any environmental information. This short paper presents results from an analytical investigation into the effects that array orientation has on linear TRA retrofocusing in shallow water. A linear TRA has three limiting orthogonal orientations with respect to a distant sound source in a shallow water waveguide: vertical, endfire, and broadside. Here, TRA retrofocus size, amplitude, location, and peak-to-sidelobe ratio are predicted from a monochromatic modal-sum formulation for sound propagation in a Pekeris waveguide and compared for the three orthogonal array orientations. Differences between retrofocusing in these three configurations are determined by the strength and propagation directions of sound waves unintentionally rebroadcast by the TRA.

PACS: 43.30Vh, 43.30Yj, 43.30Ft

Introduction

Hydrophone arrays commonly used in underwater acoustic experiments are linear and vertical and are typically moored from the ocean floor and suspended by a float, or dipped from an anchored vessel and vertically aligned by a weight. However, many important sonar applications involve towed arrays that are more nearly horizontal. This short paper presents and compares time-reversing array retrofocusing performance for different array orientations in a simple waveguide and provides illustrations of predicted horizontal TRA performance.

The performance of TRAs in waveguides have been the subject of much recent theoretical, computational, and experimental attention (Kuperman *et al.* 1998, Song *et al.* 1998, 1999, Hodgkiss *et al.* 1999, Dungan and Dowling 2000, Roux and Fink 2000, Khosla and Dowling 2001). In particular, the oceanic experiments (the first four references above) show that acoustic time reversal is a very promising technology for retrofocusing sound in the shallow ocean. However, these previous studies have only considered linear vertical arrays even though practical implementation of TRA concepts in the ocean may require more nearly horizontal or towed array deployment. The purpose of this paper is to illustrate the inherent limitations of the three limiting cases of linear TRA orientation (vertical, endfire, and broadside) for TRAs responding to a single remote time-harmonic source in a shallow ocean waveguide. Here, specific results are drawn from a Pekeris waveguide and a modal sum Green's function. These results illustrate important generic features of a linear TRA's back-propagated field that will be present in any waveguide environment.

A variety of transducer array geometries and orientations have been used in several other applications with the most notable being matched field processing, a powerful technique for determining of the location of an underwater contact (for example see Tolstoy 1993 or Jensen *et al.* 1994). Recently, Tantumand and Nolte (2000) discussed ways of improving the matched field processing (MFP) results by properly shaping the array.

MFP and TRA retrofocusing are conceptually similar but differ in their intent and requisite environmental information. MFP can be used to efficiently locate sound sources in known environments. A TRA can be used to acoustically illuminate an unknown sound source in an unknown but reciprocal environment. Although MFP with horizontal arrays has been previously studied (Bogart and Yang 1994, Yang and Yates 1998), consideration of horizontal TRA retrofocusing performance has not. In particular, the orientation of the TRA will determine whether unintended back-propagating waves appear near the retrofocus location thereby leading to increased sidelobes (spurious retrofoci). While the findings presented here are similar to those in the previous horizontal-linear-array MFP studies, the current explanation of the results in terms of unintended back-propagating waves is new.

The remainder of this short paper is broken into the three sections; the first of which briefly introduces the foundations of acoustic time reversal. The next section presents results for three basic orientations of a TRA in an ideal shallow water waveguide. The final section summarizes the findings and states the conclusions of this research.

I. Narrowband Acoustic Time Reversal

Active acoustic time reversing arrays operate by listening to a remote sound source and then broadcasting what was heard back into in the environment in a time reversed fashion. When the array has sufficient aperture and the environment is reciprocal, the array-broadcast sound will retrace its path(s) back to its point of origin where it will retrofocus at the location of the original sound source even when the environment, the array element locations, and the sound source location are all unknown. The quality and lifetime of this retrofocus field is determined by the characteristics of the environment, the sound signal, and the array. Here, the emphasis is on the influence of the final factor. The formal basis for acoustic time reversal is provided in Jackson and Dowling (1991). This subsection describes the computation of the narrow-band acoustic time reversal Green's function.

The response of a time-reversing array (TRA) is entirely described by the conjugate Green's function, $G_{c\omega}$, shown in (1) [see Jackson and Dowling (1991) Eq. (10), or Kuperman *et al.* (1998) Eq. (7)]. This can be extended to an array of discrete point sources as

$$G_{c\omega}(r,z,x,t_2 - t_1) = \sum_{n=1}^{N} G_{2\omega}(r,z,x;r_n,z_n,x_n)G_{1\omega}^*(r_n,z_n,x_n;0,z_s,0) \tag{1}$$

where r, z, and x are the range, depth and cross-range coordinates, respectively, N is the number of array elements, $G_{m\omega}(r,z,x;r',z',x')$ is the Green's function at radian frequency ω for acoustic propagation from (r',z',x') to (r,z,x) at time t_m, and the asterisk denotes complex conjugation. The time delay, $t_2 - t_1$, is taken to be zero for this study.

To get a quick overview of the performance for the different TRA orientations, narrow-band acoustic time reversal was studied using a modal sum for the Green's function (see Jensen *et al.* 1994) in the idealized Pekeris waveguide environment shown in Fig. 1. The half-space bottom layer has a density of 1700 kg/m^3 and a speed of sound of 1650 m/s. For simplicity there is no attenuation in the bottom, the water sound speed profile is isovelocity at 1500 m/s, and the ocean surface is treated as a flat pressure-release surface. The effects of absorption, refraction, and internal wave dynamics are simulated in Dungan and Dowling (2000). The complications posed by bubble scattering, bubble absorption, and dynamic rough ocean-surface scattering typical at acoustic frequencies in the kHz range and above are beyond the scope of this study. Assessments of rough surface scattering and TRA performance are provided in Kuperman *et al.* (1998) and Khosla and Dowling (1998).

As illustrated in Fig. 1, a linear TRA has three limiting orientations possible within the shallow ocean: vertical, endfire, and broadside. The vertical TRA has elements located at $(R,z_n,0)$. The endfire TRA has elements at $(R-r_n,z_a,0)$. The broadside TRA has elements at (R,z_a,x_n). Other straight-array orientations fall at some rotation angle between these three limiting orthogonal cases. All the arrays studied herein have regular element spacing. The spacing variables for broadside, endfire, and vertical TRAs are Δx, Δr, and Δz. The horizontal TRAs in this study are all deployed at mid-water column, $z_a = 37.5$ m.

II. Results For Different Array Orientations

In the simple sound channel, the three TRA orientations produce different results for retrofocus size in the azimuthal, depth, and range directions, and for the prevalence of sidelobes in the vicinity of the source. The two parameters considered here beyond orientation are the depth of array and array element spacing. Two array orientations lead to unintended back-propagating waves that interfere with the intended ones and degrade the TRA's retrofocus. This finding is illustrated and discussed below.

A simple comparison of the retrofocus fields produced by 24-element TRAs having the three orthogonal orientations is shown on Figure 2 which shows range-depth slices through the

retrofocus fields computed from (1) in the Pekeris waveguide environment of Fig. 1 at a frequency of 500 Hz, a source-array range of 10 km, and a source depth of 25 m. The array element spacing is varied between the three frames of Fig. 2 to produce the best possible retrofocus results. The water-column-spanning vertical TRA ($\Delta z = 3$ m) produces the cleanest retrofocus with the fewest sidelobes (Fig. 2a). A somewhat longer endfire array ($\Delta r = 50$ m) produces a comparable retrofocus with only a few sidelobes visible in its range-depth field slice (Fig. 2b). The one strong sidelobe shown at a 50 m depth in Fig. 2b is the result of the unintended back-progating waves. Although it does produce the retrofocus with the smallest range extent, the very large aperture broadside TRA ($\Delta x = 400$) struggles to provide even minimal sidelobe suppression (Fig. 2c) because of the strong influence of unintended back-propagating waves.

The relationship between the retrofocus field structure along a linear vertical intersection at the original source location and the array element spacing is illustrated in Fig. 3 for the three orthogonal orientations at a frequency of 500 Hz, a source-array range of 10 km, a source depth of 25 m, and $N = 24$. Note that the horizontal axes of the three frames in this figure are different. The field values in each vertical intersection were normalized by their maximum value in that intersection, and black corresponds to peak field amplitude. The vertical TRA (Fig. 3a) produces the tightest vertical retofocus for the shortest overall length and performs well once it spans slightly more than half the water column. Except for a persistent sidelobe at 50 m depth, the endfire TRA (Fig. 3b) also performs well once the element spacing is 25 m or so. However, to achieve comparable vertical retrofocusing performance with a broadside TRA (Fig. 3d), its overall length reaches several kilometers. This is actually a result of the simplified sound channel geometry used here.

For the two horizontal arrays, one potential impediment to good retrofocusing is the array aperture's ability to resolve the different propagating modes, especially low-order modes with low horiztontal wavenumbers, $k_{H,n}$, where n is the mode number. A longer TRA, with end-elements having a greater difference in range to the source, should be able to better resolve these modes. Figure 3b) and c) are constructed from the same endfire array and together display this effect. Fig. 3c) shows the fraction of modes that are properly resolved versus the array spacing. Here, there are 21 propagating modes and the nth propagating mode is considered to be properly resolved by the array if the product $(k_{H,n} - k_{H,n-1})L \geq 1$ with $L =$ the total length of the array. Comparison of Fig. 3b) and c) shows that once the array resolves 90 to 95% of the modes, the sidelobe structure from the endfire array is nearly independent of array length.

However, even when the array is long enough to resolve all of the propagating modes, Fig. 3b) shows that the endfire array produces a persistent sidelobe located at a depth of 50 m. This

persistent sidelobe results from unintended back-propagating waves produced by the endfire TRA. Fig. 4 illustrates how these unintended back-propagating waves are created. Suppose for a moment that one of the paths between the source and the endire TRA leads to a quasi-plane wave arrival at the array with an arrival angle of θ with respect to the array (Fig. 4a). Because of its symmetry and because it is composed of onmi-directional sources, when the linear TRA rebroadcasts the sound arriving on this path, its response is symmetric and it launches waves at both $+\theta$ and $-\theta$ during its broadcast step. In the special case when the waveguide is isovelocity and range independent, the ensemble of unintended back-propagating waves actually coalesce near the same range as the source and form a ghost or unintended retrofocus. In range-dependent waveguides or with a depth-dependent speed of sound profile, such a ghost retrofocus will likely not form but the unintended back propagating waves will still exist and will interfere with the intended waves near the retrofocus.

Figure 5 presents further confirmation of this contention about unintended waves from the endfire TRA. It shows the same assembly of vertical field slices as Fig. 3b) except in Fig. 5a) a zero-mean random vertical displacement with root-mean-square deviation of 3 m was given to the elements of the endfire array. A comparison of Fig. 3b) and Fig. 5a) shows that the ghost retrofocus at 50 m is broken up by the random element displacements. Adding the random vertical displacements to the element locations helps to add directionality of the TRA broadcast, and this decreases production of back-propagating unintended waves. Hence, careful attention to keeping a horizontal array straight may actually be detrimental to the production of the best retrofocus.

A second test of these ideas is provided in Fig. 5b) where some vertical directionality of the TRA broadcast is added by tilting the endfire array. In this case, the array elements are linearly distributed from +3 m to –3 m from the mean depth (z_a=37.5m) between the two ends of the array. A comparison of Fig. 3b) and Fig. 5b) shows that a slightly-tilted endfire TRA suffers less from the ghost retrofocus problem than a perfectly horizontal array. Hence, a towed TRA should be deployed with some tilt to operate most effectively.

Although the unintended back-propagating waves partially spoil the retrofocusing performance of the endfire array, the situation is even worse for the broadside array because its effective length is smaller than its geometric length. In the simplified and specialized sound channel considered here where there is no azimuthal dependence, a broadside TRA with length L operating at source-array center range of R is equivalent a geometrically compressed endfire array with an effective length $\sqrt{R^2 + L^2} - R$ ($< L$) at the retrofocus location (see Fig. 6). This effective length may be much smaller than L when $R > L$. Although the outcome of this geometrical effect will be different in range- and azimuthally-dependent sound channels, the basic problem with the broadside geometry will persist. Thus, broadside-array vertical-retrofocusing performance suffers

twice because of source-array sound-channel geometry. A broadside TRA is effectively shorter than is true length so it struggles to distinguish the propagating modes of the sound channel, and—like the horizontal endfire array—it generates unintended waves that back-propagate toward the source and interfere with the intended waves at the retrofocus.

The existence of unintended back-propagating waves near the intended retrofocus location is the critical difference between vertical and horizontal TRAs. The unintended waves from the vertical TRA propagate away from it at different azimuthal angles with respect to the source-array azimuthal path, and thus do not interfere with the intended waves that converge at the TRA's retrofocus. However, for both horizontal arrays, the linear array geometry ensures that unintended waves will be launched toward the TRA's retrofocus and this geometric effect will persist independent of length or the number of elements composing the TRA.

Size of retrofocus is one indicator of TRA performance. The amplitude at the expected retrofocus location relative to that of the sidelobes is another. When the pressure amplitude at the expected retrofocus location is comparable to that at one or more sidelobes, this may be considered a poor retrofocus. Figure 7 is a summary plot of this relative amplitude for the three orthogonal TRA types at a source-array range of 10 km, a source depth of 25 m and a frequency of 500 Hz. For TRA-length efficiency, the clear order of orientation preference is vertical, endfire, and broadside for vertical sidelobe suppression. This performance ordering of is unlikely to change even at different ranges in actual ocean sound channels having greater geometric complexity.

Although broadside TRAs may become prohibitively long to achieve acceptable amplitude and vertical retrofocus size resolution, they do have an advantage in azimuthal retrofocus size resolution. Figure 8 compares different azimuthal intersections through the TRA retrofocus fields from broadside (Fig. 8a) and endfire (Fig. 8b) TRAs. Each plot consists of the field at different azimuthal angles at a constant range of $R = 10$ km from the TRA center at the depth of the original source, 25 m, for an acoustic frequency of 500 Hz. The vertical axes on both frames of Fig. 8 cover the same range of element spacing while the horizontal axes display azimuthal angle ϕ on different scales. As in Fig. 3, each intersection is normalized by the maximum field value found on that intersection and black corresponds to peak field amplitude. Thus, the dark central regions at $\phi = 0$ (the retrofocus direction) on Fig. 8 are the intended retrofoci.

As expected, the azimuthal retrofocusing performance of the broadside TRA in Fig. 8a) is far superior to that of an equivalent length endfire TRA. This result is merely an illustration of the well-known azimuthal-resolution advantage of broadside arrays and fully contrasts with the 360° ring-focus produced by a vertical TRA in a horizontally uniform environment.

III. Conclusions

This short paper reports the findings of a study of how array orientation effects linear time-reversing array retrofocusing in a simple shallow ocean environment. Performance changes produced by variations in array orientation and element spacing have been presented. Although the simulations described here are for a very simplified sound channel, the two conclusions presented here should also be applicable to actual ocean sound channels because they are fundamentally based on the geometric limitations of a linear transducer array in a sound channel environment. First, a vertical water-column-spanning TRA consistently provides the best performance for minimizing retrofocus size and sidelobes on vertical slices with the smallest overall length. However, a vertical TRA does not provide any azimuthal retrofocusing in horizontally-uniform environments. Although this is a limitation, it may not be a severe problem in actual ocean applications since vertical TRAs can produce azimuthally confined retrofoci in inhomogeneous environments (Dowling & Jackson 1992, Dungan & Dowling 2001). Second, horizontal TRAs, which naturally provide azimuthal retrofocusing, suffer from increased sidelobes through the vertical compared to a water-column spanning vertical array even when the horizontal TRAs are much longer than the water column. The increased sidelobes are caused by unintended back-propagating waves that interfere with the intended waves near the retrofocus location. Furthermore, these unintended waves are produced by the linear array geometry and cannot be eliminated by lengthening the TRA or increasing the number of TRA elements. Yet, the unintended waves can be brought under control by giving the TRA some vertical aperture. Thus, a horizontal towed TRA might be best utilized by when it is slightly tilted or when a small random vertical offset is made to its element locations.
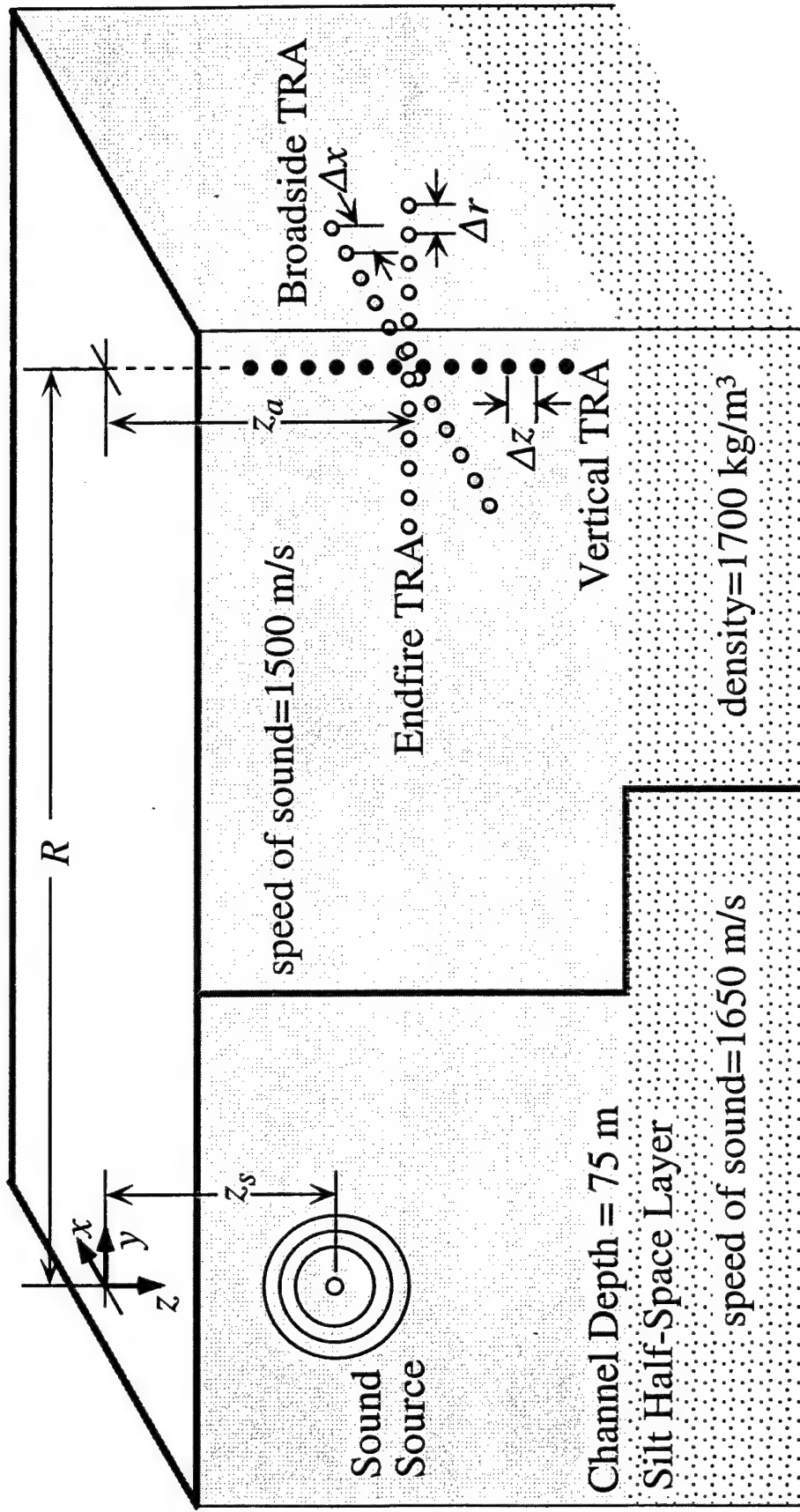
Acknowledgements

References

Bogart, C.W., and Yang, T.C. (**1994**). "Source localization with horizontal arrays in shallow water: Spatial sampling and effective aperture," J. Acoust. Soc. Am. **96**, 1677-1686.

Dowling, D.R. and Jackson, D.R. (**1992**). "Narrow-band performance of acoustic phase-conjugate arrays in dynamic random media," J. Acoust. Soc. Am. **91**, 3257-3277.

Dungan, M.R., and Dowling, D.R. (**2000**). "Computed narrowband time-reversing array retrofocusing in a dynamic shallow ocean," J. Acoust. Soc. Am. **107**, 3101-3112.

Dungan, M.R. and Dowling, D.R. (**2001**). "Computed narrowband azimuthal time-reversing array retrofocusing in shallow water," submitted to J. Acoust. Soc. Am.

Hodgkiss, W.S., Song, H.C., Kuperman, W.A., Akal, T., Ferla, C., and Jackson, D.R. (1999). "A long-range and variable focus phase-conjugation experiment in shallow water" J. Acoust. Soc. Am. 105, 1597-1604.

Jackson, D.R. and Dowling, D.R. (1991). "Phase-conjugation in underwater acoustics," J. Acoust. Soc. Am. 89, 171-181.

Jensen, F.B., Kuperman, W.A., Porter, M.B., and Schmidt, H. (1994). *Computational Ocean Acoustics* (AIP Press, New York).

Khosla, S.R. and Dowling, D.R. (1998). "Time-reversing array retrofocusing in simple dynamic underwater environments," J. Acoust. Soc. Am. 104, 3339-3350.

Khosla, S.R., and Dowling, D.R. (2001). "Time-reversing array retrofocusing in noisy environments," in press, J. Acoust. Soc. Am.

Kuperman, W.A., Hodgkiss, W.S., Song, H.C., Akal, T., Ferla, C., and Jackson, D.R. (1998). "Phase-conjugation in the ocean: experimental demonstration of an acoustic time reversal mirror," J. Acoust. Soc. Am. 103, 25-40.

Roux, P. and Fink, M. (2000). "Time reversal in a waveguide: Study of the temporal and spatial focusing," J. Acoust. Soc. Am. 107, 2418-2429.

Song, H.C., Kuperman, W.A., and Hodgkiss, W.S. (1998a). "A time-reversal mirror with variable range focusing," J. Acoust. Soc. Am. 103, 3234-3240.

Song, H.C., Kuperman, W.A., Hodgkiss, W.S., Akal, T., and Ferla, C. (1999). "Iterative time reversal in the ocean," J. Acoust. Soc. Am. 105, 3176-3184.

Tantum, S.L. and Nolte, L.W. (2000). "On array design for matched-field processing," J. Acoust. Soc. Am. 107, 2101-2111.

Tolstoy, A. (1993). *Matched Field Processing for Underwater Acoustics,* World Scientific, Singapore.

Yang, T.C., and Yates, T. (1998) "Matched-beam processing: Application to a horizontal line array in shallow water," J. Acoust. Soc. Am. 104, 1316-1330.
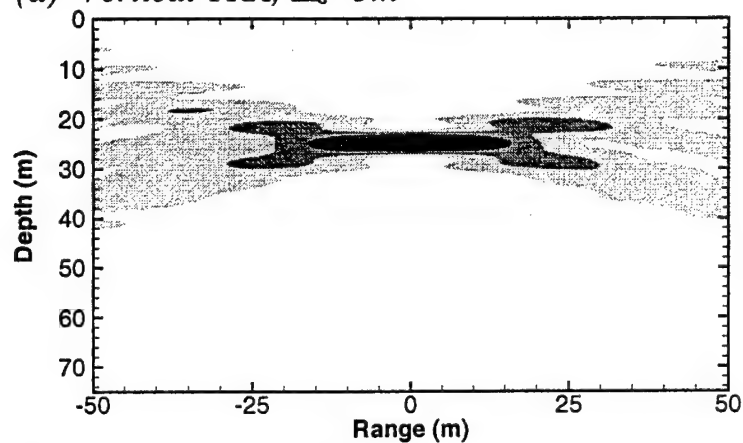
Figure Captions

Fig. 1 Geometry of TRA orientations in a simple sound channel: vertical, horizontal endfire and horizontal broadside. The simple sound channel is a Pekeris waveguide having a modal-sum Green's function. There is no attenuation present in the bottom. Parameter values are listed in the figure.

Fig. 2 Retrofocus plots through range and depth for various TRA orientations and element spacing for a source depth of $z_s = 25$ m, a source-array range of $R = 10$ km, and an acoustic frequency of $f = 500$ Hz. The computed results from: a vertical TRA with 3 m element spacing is shown in (a), an endfire TRA with a 50 m element spacing in (b), and a broadside TRA with a 400 m spacing in (c).

Fig. 3 Compilation of vertical intersections through the intended retrofocus location for various element spacings for a vertical TRA (a), an endfire TRA (b), and a broadside TRA (d). Frame (c) should be compared to (b) and displays the fraction of propagating modes that the endire array properly resolves. The sidelobe pattern becomes essentially constant once the array is long enough to resolve ~90 to 95% of the modes. Each array is composed of 24 elements and is centered at a depth of $z_a = 37.5$ m and a source-range of $R = 10$ km. The acoustic frequency is $f = 500$ Hz with a source depth $z_s = 25$ m. Each profile in (a), (b), and (d) is normalized to the maximum pressure value.

Fig. 4 Production of unintended back-propagating waves with an endfire TRA. In (a) the array receives a wave from above at an angle $+\theta$. In (b), the TRA creates back propagating waves with angles of $+\theta$ and $-\theta$. The wave launched at $-\theta$ is unintended and may cause sidelobes or a ghost retrofocus near the intended retrofocus location.

Fig. 5 Compilation of vertical intersections through the intended retrofocus location for slightly modified endfire arrays. In (a), the TRA elements have been randomly shifted with 3 m rms vertical displacement. In (b) the array has been tilted so that it lies on a mild diagonal and spans 6 m vertically at the center of the water column. Comparison of both frames to Fig. 3b) shows that even a modest amount of vertical aperture helps control the unintended wave problem illustrated in Fig. 4.

Fig. 6 Geometrical collapse of a broadside TRA into an endfire TRA.

Fig. 7 Normalized retrofocus peak amplitude for vertical, endfire and broadside TRAs at an acoustic frequency of $f = 500$ Hz and a source at depth $z_s = 25$ m. Each 24 element array is centered at a range of $R = 10$ km and a depth of $z_a = 37.5$ m. The vertical axis is the ratio between the amplitude at the expected retrofocus location divided by the maximum amplitude in a vertical slice at the source range. The endfire and horiztonal arrays have to be long to work well. Array sparseness causes the fluctuations at element spacing of greater than 100 m.

Fig. 8 Compilation of azimuthal profiles of retrofocus peaks for various array spacing values for a broadside (a) and an endfire (b) TRA. Note the larger range of azimuthal angles required to capture the retrofoci from the endfire configuration in (b). Each array is composed of 24 elements and is centered at a depth of $z_a = 37.5$ m at a source-array range $R = 10$ km. The acoustic frequency is $f = 500$ Hz with a source depth of $z_s = 25$ m. Each profile is normalized by its maximum pressure value. A vertical TRA retrofocuses into a 360° ring in the horizontally-uniform Pekeris waveguide.
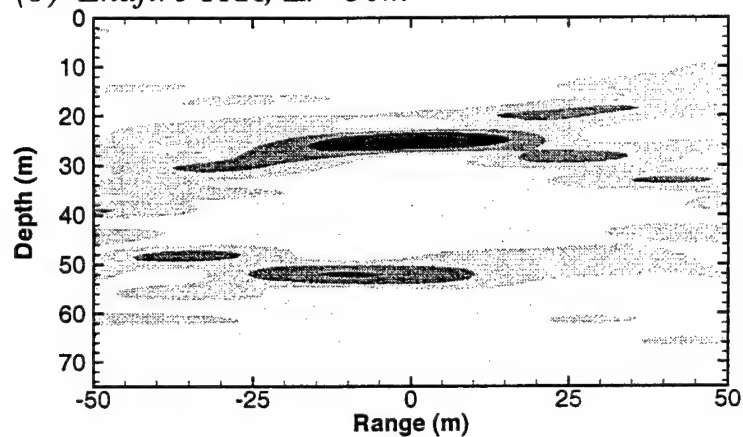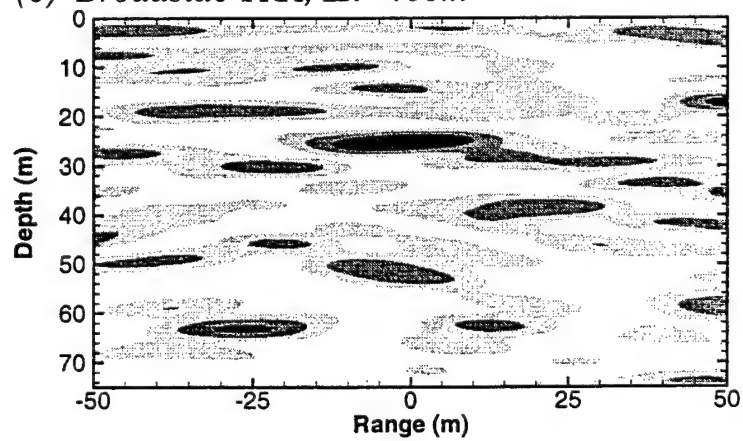
Sound
Source

z
x
y

z_s

R

speed of sound=1500 m/s

z_a

Broadside TRA

Δx

Δr

Endfire TRA

Δz

Vertical TRA

Channel Depth = 75 m
Silt Half-Space Layer

speed of sound=1650 m/s

density=1700 kg/m³

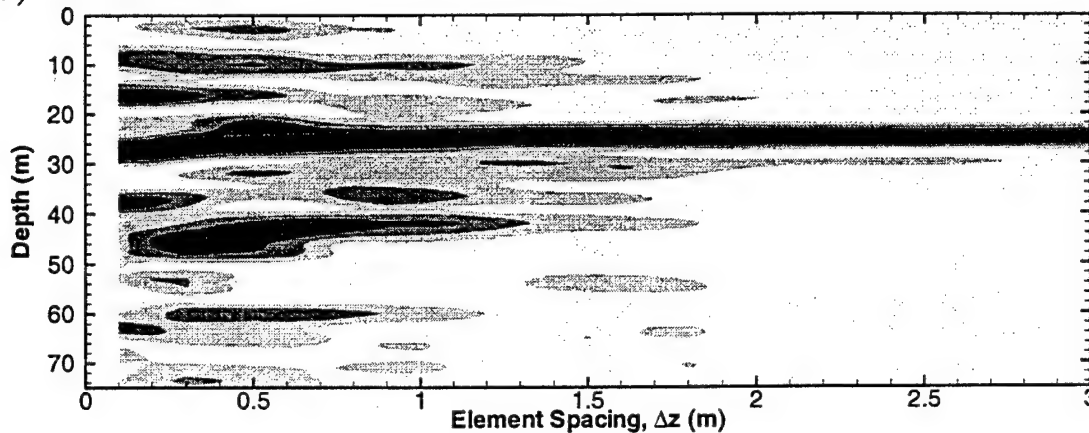0.1   0.3   0.5   0.7   0.9
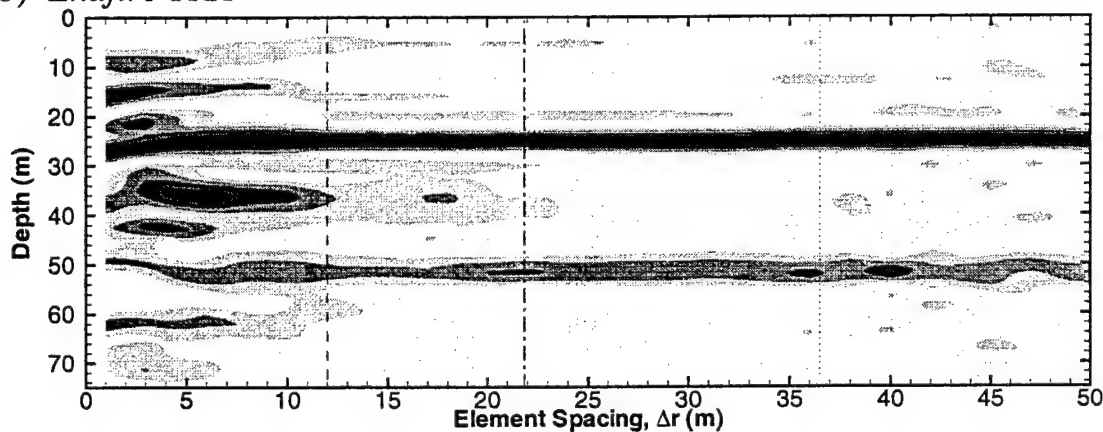
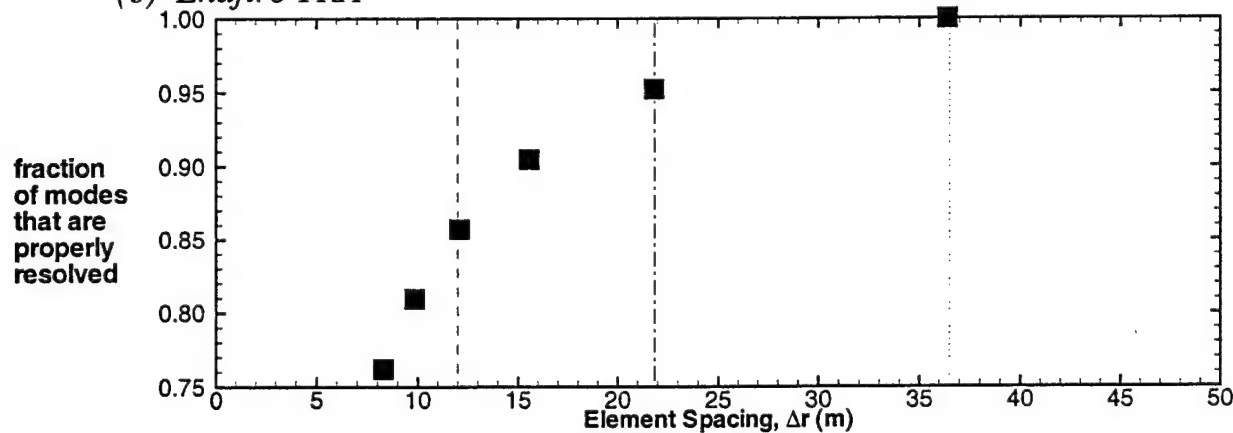(a) Vertical TRA, Δz=3m

(b) Endfire TRA, Δr=50m
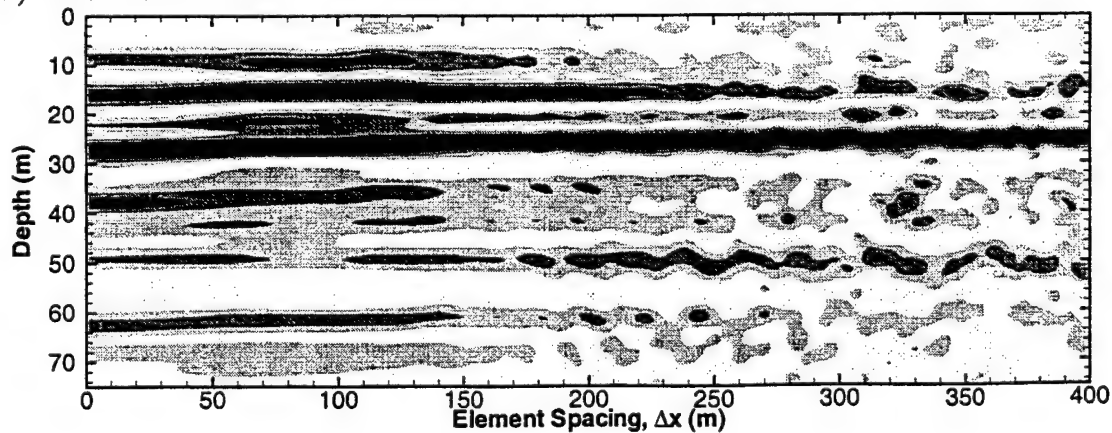
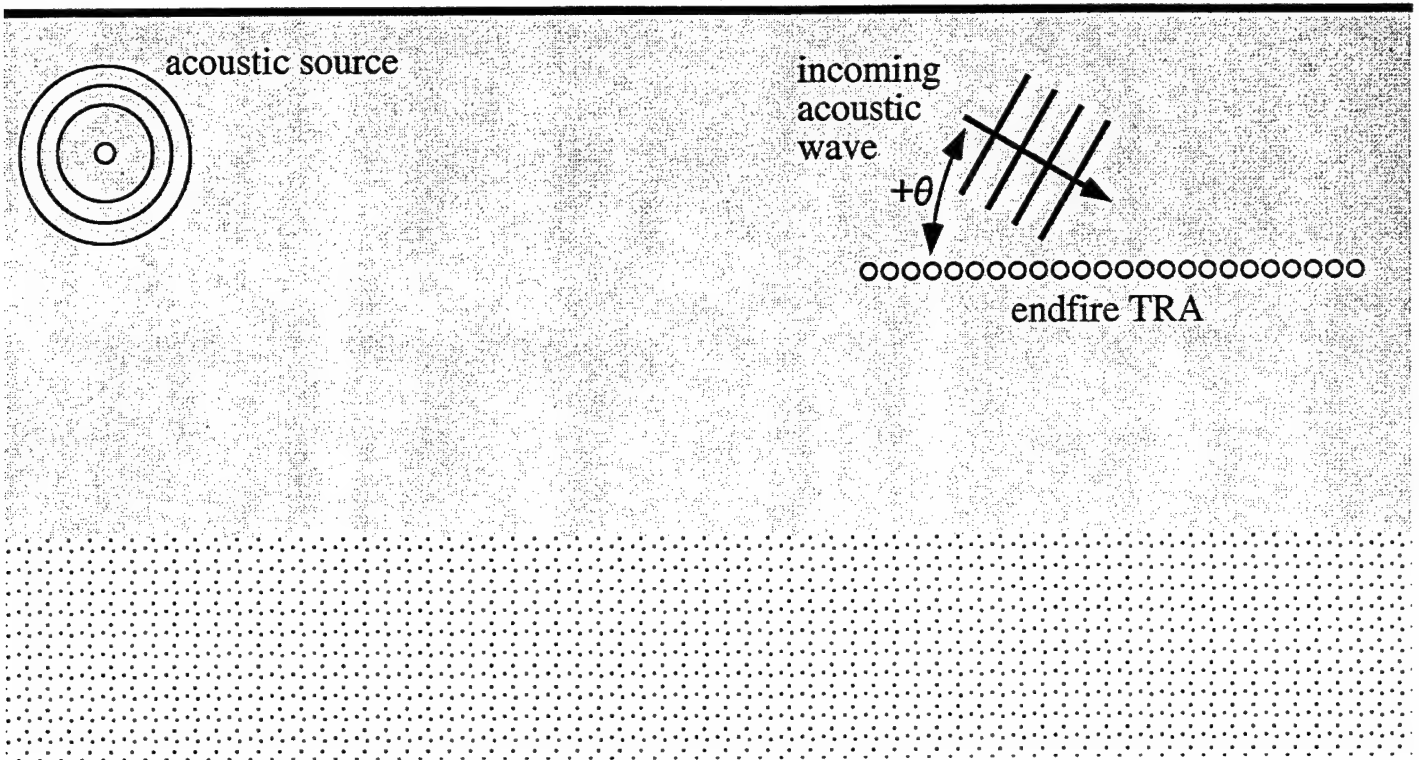(c) Broadside TRA, Δx=400m

(a) *Vertical TRA*

(b) *Endfire TRA*

(c) *Endfire TRA*

fraction of modes that are properly resolved

(d) *Broadside TRA*

(a) Endfire TRA receives acoustic signal

acoustic source

incoming acoustic wave

$+\theta$

endfire TRA

(b) Endfire TRA rebroadcasts time-reversed acoustic signal

true retrofocus

outgoing time-reversed acoustic wave

$+\theta$

ghost focus

$-\theta$

Due to symmetry of endfire horizontal TRA, an unintended acoustic wave is also broadcast
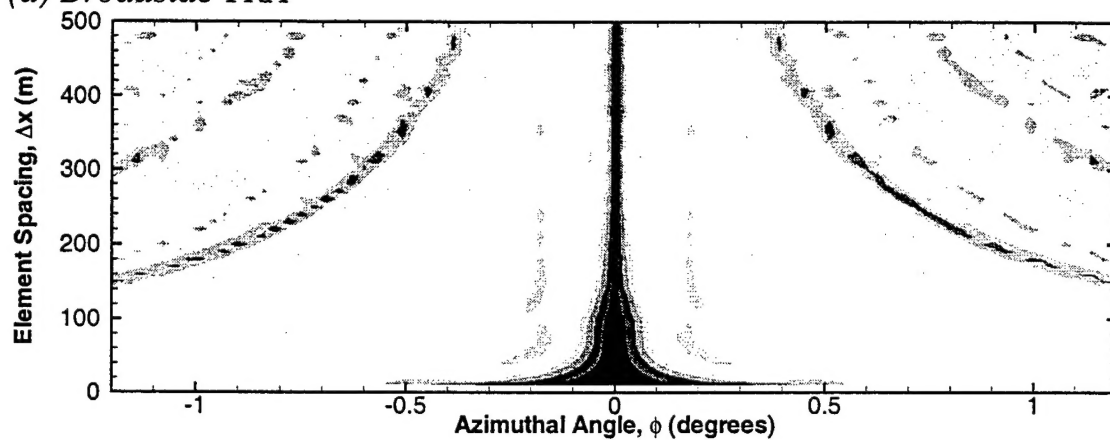
(a)

(b)

range-equivalent
endfire TRA

broadside TRA

R_n

R_n
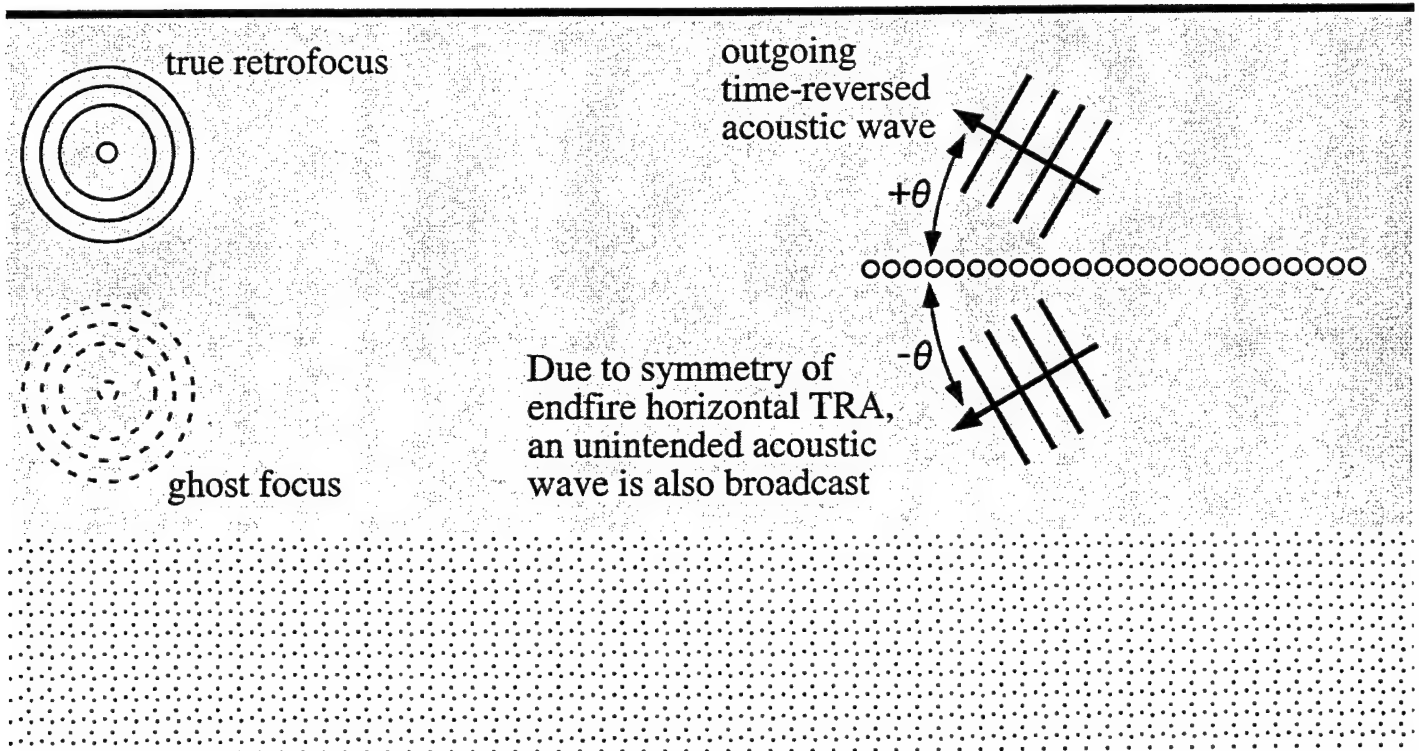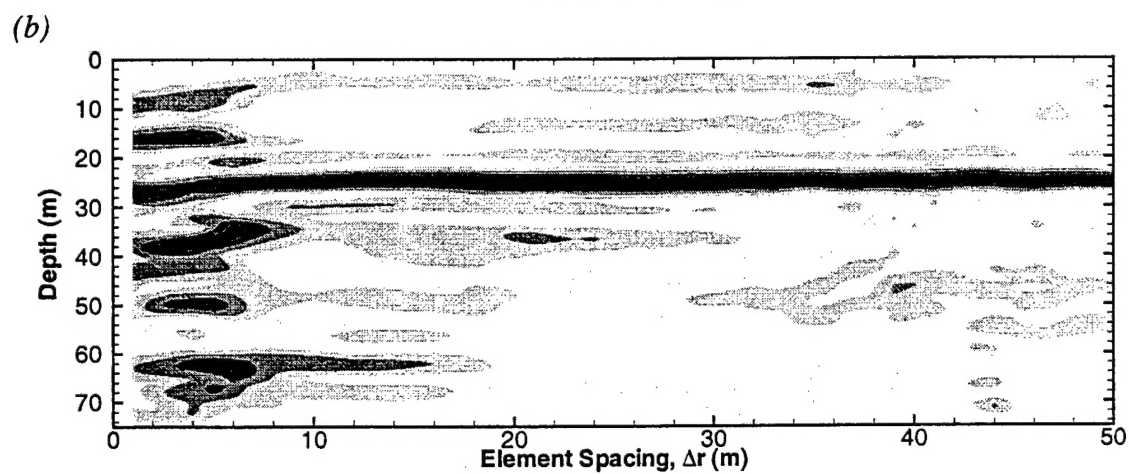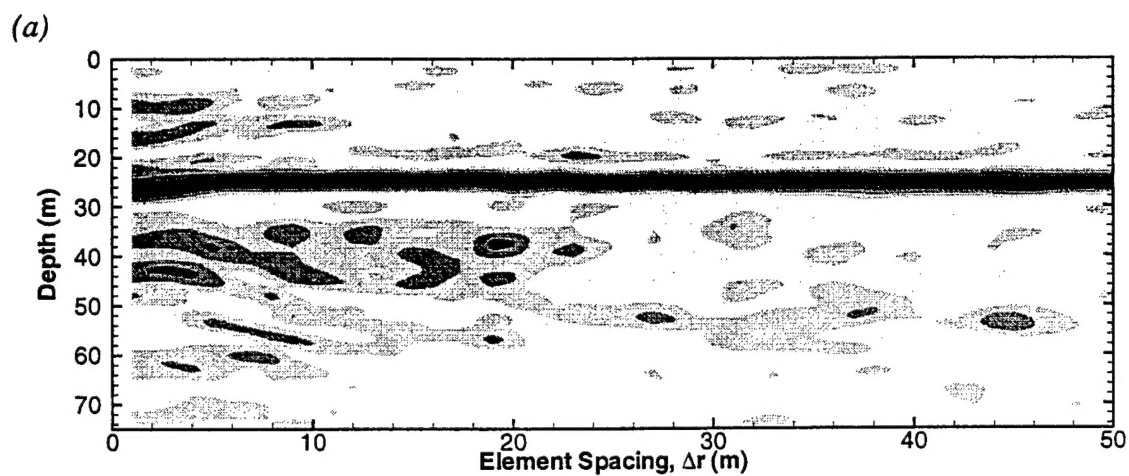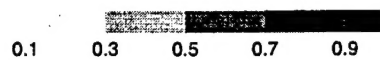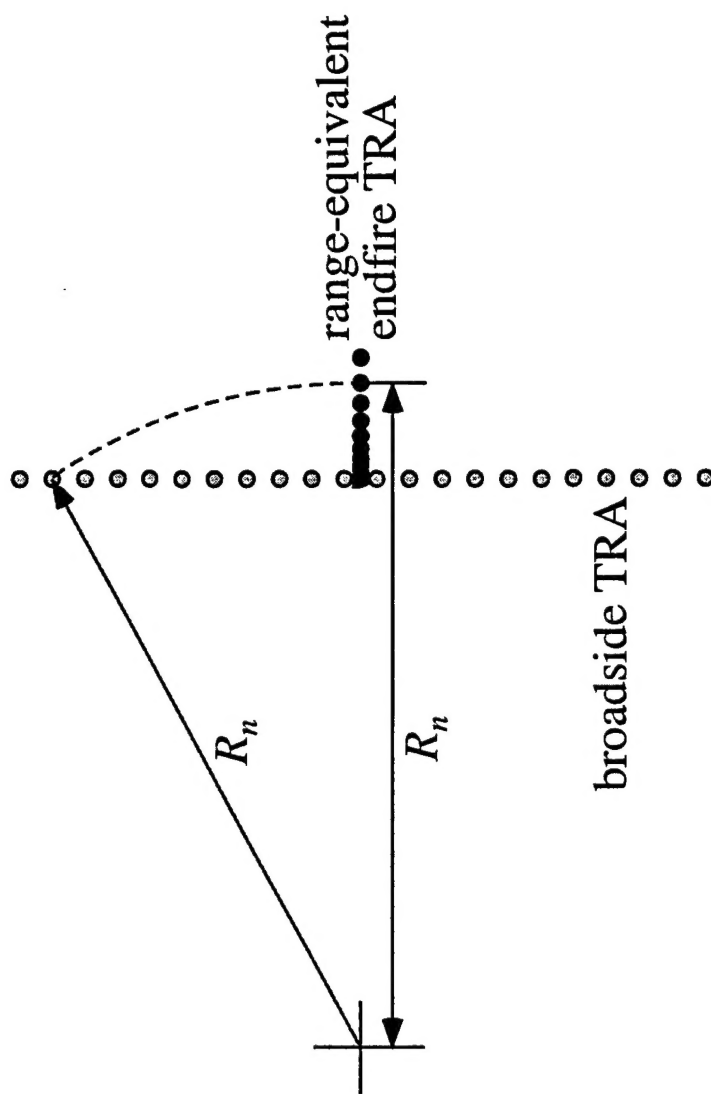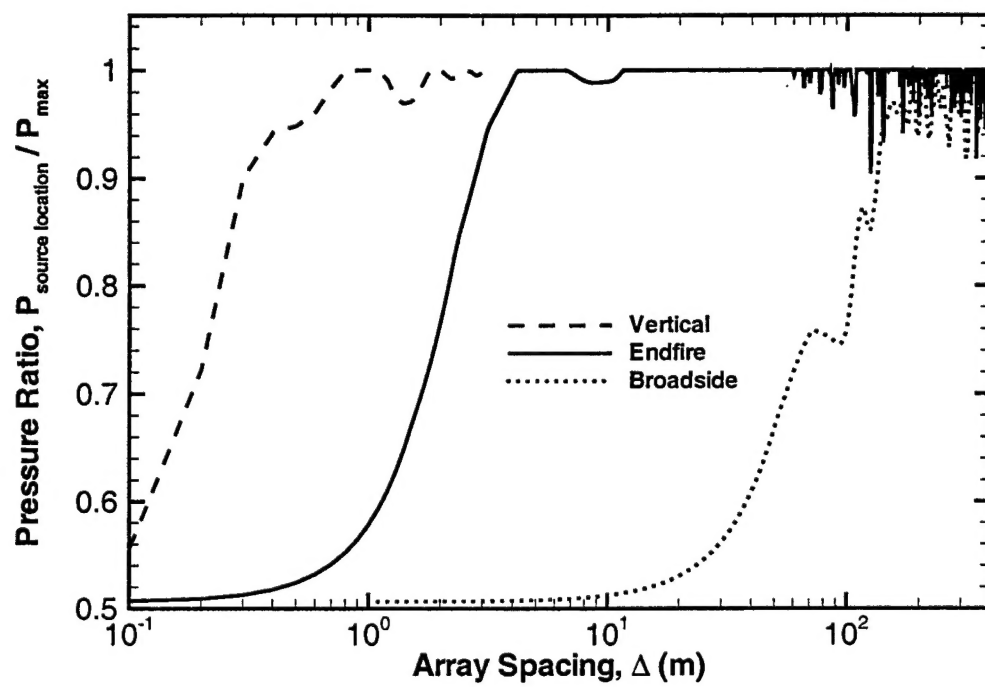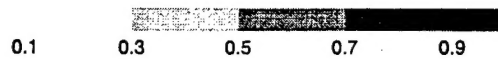
(a) Broadside TRA

(b) Endfire TRA